

MODULATION OF WIND GENERATED WAVES  
BY LONG GRAVITY WAVES

By

ALLAN M. REECE, JR.

A DISSERTATION PRESENTED TO THE GRADUATE COUNCIL  
OF THE UNIVERSITY OF FLORIDA  
IN PARTIAL FULFILLMENT OF THE REQUIREMENTS FOR THE  
DEGREE OF DOCTOR OF PHILOSOPHY

UNIVERSITY OF FLORIDA

1976

## ACKNOWLEDGMENTS

I wish to express my appreciation to Professor Omar H. Shemdin for providing the motivation from which this study grew and the means to carry it on to a conclusion.

I owe many thanks also to other members of the Coastal and Oceanographic Engineering Laboratory staff. In particular I want to thank Mrs. Melody Gaudy for painstakingly transforming the handwritten copy of this paper into a typed rough draft, and Mrs. Lillean Pieter for producing reproducible drawings.

In addition the highly professional approach of Mrs. Elaine Mabry has made the final manuscript of superior quality.

My sincerest appreciation is due my wife, Margo, for her remarkable ability to encourage and motivate me over the period during which this dissertation was written.

This work was sponsored by NOAA - Space Oceanography Program under Grant NG-29-72 and by the Jet Propulsion Laboratory under Contract 954030.

10-77

## TABLE OF CONTENTS

	Page
Acknowledgments . . . . .	ii
List of Figures . . . . .	v
Abstract . . . . .	ix
Chapter I. Introduction . . . . .	1
A. The Need for the Study of High Frequency Waves . . . . .	1
B. Description and Scope of the Present Work . . . . .	4
Chapter II. Investigations of Waves and Associated Energy Transfers . . . . .	5
A. Transfer of Mechanical Energy to Waves Through the Miles-Phillips Mechanism . . . . .	5
B. Interactions Among Components of a Wave System . . . . .	15
1. Tick Second Order Perturbation of the Wave Spectrum . . . . .	16
2. Benjamin and Feir Side Band Interactions . . . . .	18
3. Phillips Resonant Interaction Among Gravity Waves . . . . .	22
4. McGoldrick Resonant Interaction Among Capillary-Gravity Waves . . . . .	26
5. Hasselmann Fifth Order Nonlinear Interchange . . . . .	28
6. Valenzuela Capillary-Gravity Wave Resonant Interaction . . . . .	30
C. Experimental Studies of High Frequency Waves . . . . .	32
Chapter III. Measurement of Wave Slope . . . . .	39
A. Measurement of Slope Versus Height . . . . .	39
B. The Wind-Wave Facility . . . . .	44
C. Laser-Optical System for Measuring Slope . . . . .	47
D. Supporting Measurements . . . . .	66
E. Experimental Conditions . . . . .	70
F. Digital Data Acquisition and Reduction . . . . .	74
Chapter IV. Experimental Results . . . . .	83
A. Time Series Data . . . . .	83
B. First Order Spectra . . . . .	99
C. Spectral Modulations . . . . .	104
D. Amplitude Modulation of the Spectrum . . . . .	111

TABLE OF CONTENTS (continued)

	Page
Chapter V. Theories of Interaction Between Short Waves and Long Waves . . . . .	117
A. The Two-Scale Model of Longuet-Higgins and Stewart . . . . .	118
B. The Solution of the Two-Scale Wave Model by Direct Integration of the Wave Energy Equation . . . . .	122
C. The Solution of the Two-Scale Wave Model by Perturbation of the Wave Energy Equation . . . . .	125
D. The Modulation of Short Wave Spectra by Long Waves . . . . .	128
Chapter VI. Comparison Between Experimental and Theoretical Results . . . . .	137
A. Determination of Spectral Modulation by the Modeling Methods . . . . .	137
B. Model Based on the Wave Energy Equation . . . . .	141
C. Model Based on the Hamiltonian Formulation . . . . .	144
Chapter VII. Conclusions . . . . .	180
Appendix I. The Boltzmann Transport Equation . . . . .	183
Appendix II. The Wave-Wave Interaction Integral . . . . .	188
List of References . . . . .	192
Biographical Sketch . . . . .	196

## LIST OF FIGURES

Figure	Page
1 Plan and side views of the wind-wave tank model . . . . .	45
2 Wave generator section and test section of the wind-wave model . . . . .	46
3 Orientation diagram for laser beam refraction at the air water interface . . . . .	48
4 The conversion of deflection angle to wave slope . . . . .	51
5 Schematic view of the receiver of the optical wave slope measurement system . . . . .	52
6 Maximum deflection and slope angles measurable as a function of distance from the objective lens to the local water level . . . . .	54
7 Analog conversion of the photodiode output signals to orthogonal axes of deflection . . . . .	56
8 Error introduced into the slope measurement due to the finite size of the laser beam . . . . .	58
9 Static response of the instrument receiver to deflection and azimuth changes . . . . .	60
10 X channel instrument calibration curve . . . . .	61
11 Schematic cross section of the wave tank at the instrument installation site . . . . .	62
12 The slope measurement receiver in operating position in the wave tank . . . . .	64
13 Side view of the installed relationship between the system light source and receiver . . . . .	65
14 The wave gauge calibration for experiment 3 . . . . .	67
15 Three local wind velocity profiles . . . . .	69
16 Wave record segmenting scheme used to produce short wave slope epics for phase averaging . . . . .	76

LIST OF FIGURES (continued)

Figure	Page
17 Visualization of a typical trend removal sequence . . . . .	79
18 Phase averaged slope energy spectral estimate at the front face of the long wave crest . . . . .	81
19 Wave slope and height time records for experiment E3 and tests T13 and T14 . . . . .	85
20 Wave slope and height time records for experiment E3 and tests T15 and T16 . . . . .	87
21 Wave slope and height time records for experiment E3 and test T17 . . . . .	89
22 Wave slope and height time records for experiment E3 and test T18 . . . . .	91
23 Wave slope and height time records for experiment E3 and test T19 . . . . .	93
24 Wave slope and height time records for experiment E3 and test T20 . . . . .	95
25 Wave slope and height time records for experiment E3 and test T21 . . . . .	97
26 Average total wave slope spectra . . . . .	100
27 Average total wave slope spectra . . . . .	101
28 Average total wave slope spectra . . . . .	102
29 Phase averaged short wave slope spectra from the crest and trough regions of the long wave profile for experiment E3 and test T15 . . . . .	106
30 Phase averaged short wave slope spectra from the crest and trough regions of the long wave profile for experiment E3 and test T16 . . . . .	108
31 Example of the short wave energy modulation for selected free wave frequencies from experiment E3 and test T15. Advection is not considered . . . . .	112
32 Example of the short wave energy modulation for selected free wave frequencies from experiment E3 and test T16. Advection is not considered . . . . .	113

LIST OF FIGURES (continued)

Figure	Page
33 Example of the short wave energy modulation for selected free wave frequencies from experiment E3 and test T15. The advection correction is applied . . . . .	114
34 Example of the short wave energy modulation for selected free wave frequencies from experiment E3 and test T16. The advection correction is applied . . . . .	115
35 Comparison for experiment E3 and test T16 between the experimental modulation results and the theoretical prediction based on the hydrodynamic energy equation with the cyclic perturbation . . . . .	142
36 Comparison for experiment E3 and test T19 between the experimental modulation results and the theoretical prediction based on the hydrodynamic energy equation with the cyclic perturbation . . . . .	143
37 Eight point amplitude modulation comparison . . . . .	148
38 Magnitudes and phases of the short wave slope energy amplitude modulation for the conditions of experiment E3 and test T14 . . . . .	150
39 Magnitudes and phases of the short wave slope energy amplitude modulation for the conditions of experiment E3 and test T15 . . . . .	152
40 Magnitudes and phases of the short wave slope energy amplitude modulation for the conditions of experiment E3 and test T16 . . . . .	154
41 Magnitudes and phases of the short wave slope energy amplitude modulation for the conditions of experiment E3 and test T17 . . . . .	156
42 Magnitudes and phases of the short wave slope energy amplitude modulation for the conditions of experiment E3 and test T18 . . . . .	158
43 Magnitudes and phases of the short wave slope energy amplitude modulation for the conditions of experiment E3 and test T19 . . . . .	160
44 Magnitudes and phases of the short wave slope energy amplitude modulation for the conditions of experiment E3 and test T20 . . . . .	162

LIST OF FIGURES (continued)

Figure	Page
45 Magnitudes and phases of the short wave slope energy amplitude modulation for the conditions of experiment E3 and test T21 . . . . .	164
46 Magnitudes and phases of the short wave slope energy amplitude modulation for the free wave frequency of 5.00 Hz . . . . .	166
47 Magnitudes and phases of the short wave slope energy amplitude modulation for the free wave frequency of 6.25 Hz . . . . .	168
48 Magnitudes and phases of the short wave slope energy amplitude modulation for the free wave frequency of 9.38 Hz . . . . .	170
49 Magnitudes and phases of the short wave slope energy amplitude modulation for the free wave frequency of 10.00 Hz . . . . .	172
50 Magnitudes and phases of the short wave slope energy amplitude modulation for the free wave frequency of 12.50 Hz . . . . .	174
51 Magnitudes and phases of the short wave slope energy amplitude modulation for the free wave frequency of 15.63 Hz . . . . .	176
52 Magnitudes and phases of the short wave slope energy amplitude modulation for the free wave frequency of 20.00 Hz . . . . .	178

Abstract of Dissertation Presented to the Graduate Council  
of the University of Florida in Partial Fulfillment of the  
Requirements for the Degree of Doctor of Philosophy

MODULATION OF WIND GENERATED WAVES  
BY LONG GRAVITY WAVES

By

Allan M. Reece, Jr.

December, 1976

Chairman: Omar H. Shemdin  
Major Department: Civil Engineering

The cyclic short wave variations, phase related to the long wave profile, that occur during active generation of the short wave field by wind are investigated. Measurements consisting of wave slope time series are made in a laboratory environment allowing the independent generation of two scales of motion. The large scale, long wave motion is developed mechanically with a 2.0 s period and 0.06 radian maximum slope. The small scale, short wave motion occupies a broader spectral region and is generated primarily by the action of the overlying air flow. The wind speeds used are referenced as 4.4 m/s to 10.0 m/s. The short waves of particular interest are chosen to be those of 5.00 to 20.00 Hz due to the rapid responses expected as a result of strong air sea and hydrodynamic coupling in that range.

Wave slope is measured locally, and continuously in time with a device utilizing the phenomenon of optical refraction at the air sea interface as the basis for the detection of slope angle. It is found that within the experimental bounds short wave slope energy exhibits a cyclic variation along the long wave profile that is related to that profile and characterized as a modulation. The observed variation is

separable conceptually and practically into effects having two origins. The first effect is the shift in short wave frequency brought about by bodily advection of the short wave profile by flow underlying it associated with the long wave. The shifted frequency is found to be adequately predicted by the linear combination of the small scale free wave frequency and the advection effect given by the product of short wave wavenumber and underlying velocity. The modulation of frequency is found to be an increasing function of free short wave frequency. Frequency shifts vary from 40% to 126% of the free wave frequency, increasing with free wave frequency and reference wind speed. For the long wave investigated the peak to peak variation about the mean advected frequency is 58% of that frequency for all wind speeds.

The second effect is that of small scale slope amplitude modulation brought about by straining against the long wave orbital flow and subsequent relaxation through wave-wave interaction toward the mean value of the energy. The peak to peak energy excursion of a variance element in the wave slope spectrum is considered after removal of the frequency modulation and is commonly found to be 100% of the mean value of the energy. The magnitude of the excursion becomes smaller as short wave frequency increases, and larger as wind speed increases. The experimentally determined phase of the energy excursions, relative to the long wave profile, place maximum values  $45^{\circ}$  to  $180^{\circ}$  ahead of the long wave crest.

The behavior of the energy content of a variance element in the short wave portion of the spectrum is characterized as a relaxation. The relaxation behavior, due to wave-wave coupling, is introduced into the Boltzmann transport equation to describe the evolution in space of the short wave slope energy along the long wave profile. The following

assumptions are employed in the analysis: (1) The wave system is two dimensional. (2) The short wave energy exists in a steady state over the large scale of motion. (3) The local variations in short wave energy are cyclic and related to the long wave horizontal orbital velocity. (4) The long wave is sinusoidal. (5) The local short wave frequency is given by the correct free wave frequency plus the linear modification due to the underlying flow. (6) Atmospheric input produces exponential wave growth. (7) Damping by nonconservative forces is negligible. (8) Wave-wave coupling among the short waves produces a relaxation type of energy drain from the disturbed energy values of a variance element. The analysis yields results that fit the experimental values well when the relaxation factor is taken to be a constant value of 6.3. If the relaxation factor is allowed to vary from 1.57 to 15.7, for any particular test and frequency the agreement between experiment and theory for the amplitude modulation can generally be made exact.

## CHAPTER I

### INTRODUCTION

#### I.A. The Need for the Study of High Frequency Waves

An understanding of how short waves evolve during their life span in time is essential to the advancement of two principle areas of oceanographic research. The field of remote sensing of oceanic parameters is presently undergoing a period of intense development. In many instances remote sensing is a function of short wave activity. From a more theoretical standpoint short waves are critically related to the study of the development of an ocean wave spectrum.

The large extent of the ocean, combined with its rather inhospitable nature, has made it difficult to obtain a great density of data concerning its dynamic state. As a result, the predictions of temporal and spatial distributions of surface waves have always contained considerable uncertainty. Recently the tools developed for remote sensing operations have been applied to problems of a geophysical nature. Photographic, nonvisual optical, and microwave instruments are being used for water wave detection. Groups associated with the technology of space flight are searching for new applications for space vehicles. Combining the advanced sensing capabilities of remote sensors with the ubiquitous platform provided by a space vehicle, could provide a remarkably efficient technique for monitoring the motion and local environment of the ocean surface. Of special interest currently is the role airborne and spaceborne radar will fulfill in the remote sensing of

atmospheric and oceanic parameters. Radiation of radar frequencies interacts with water waves of short wavelength through the mechanism of Bragg scattering (Crombie, 1955). If the response of the short waves to the wind and wave conditions were known, the wind and sea state could be inferred from the radar return. This information has obvious scientific, military, and commercial importance.

Short wave activity undoubtedly plays a major role in the development of an ocean wave spectrum. Stewart (1961) indicated that wave motion is probably the first line in the path of energy flux from the air flow to the total water motion. Using data compiled from ocean wave growth measurements, he demonstrated that the minimum contribution to the total drag on the air flow due to the direct flux of energy to the wave motion is at least 20%. This figure is probably quite low because it did not consider the whole spectrum that existed, nor the dissipation and flow of energy from the waves to the mean motion that occurred. Stewart argued that since the flow of air over the interface is aerodynamically rough, or nearly so, the energy of the air flow that passes to the water must go by way of the correlation product of the local pressure and vertical surface velocity. The work done by normal stresses produces only irrotational motions. A wave motion must result, which will, however, augment the surface drift current.

Short waves are suspected of being responsible for a conduction of energy to longer waves by several mechanisms. Wave interaction theories predict energy flows among groups of short waves, some of which are longer than others. These theories will be mentioned in Chapter II. Short waves can also create an energy flux to much longer waves by their support of a variable wind stress. Lonquet-Higgins (1969a) demonstrated that a fluctuating tangential stress at the free surface is dynamically

equivalent to a normal stress fluctuation lagging the tangential stress by  $90^\circ$ . This results from a change in boundary layer thickness brought about by the fluctuation in the tangential stress. In particular the stress he worked with had a sinusoidal variation along the surface of a sinusoidal long wave. Wu (1968) found experimentally that, at low wind speeds at least, surface roughness is related to short wave size and distribution. If the short waves were to vary cyclicly along a sinusoidal long wave profile in such a manner that the wind shear reached a maximum near the long wave crest, a normal stress maximum would appear on the rear face of the long wave crest. The correlation product of this pressure with the local vertical surface velocity would lead to an additional net inflow of energy to the long wave motion.

The response of short waves to the wind and sea is not entirely clear. Pierson (1975) expressed the idea that wind speed dependence in the overall mean spectra of short waves does exist. However, the idea is not heavily supported by experimental evidence (Phillips, 1969). On the other hand, evidence strongly indicates that the short wave motion is not steady in a local mean sense, but may vary cyclicly with a longer wave component and intermittently with coupling to the airflow. Fluctuations in the short wave energy related to the long wave motion were noticed early in the study of waves, and were pointed out for the first time by Russell (1844). He noticed steepening of the short waves in the neighborhood of the long wave crests. Dorman and Moilo-Christensen (1972) made measurements of wave response to wind gusts, indicating that there were bursts of momentum exchange between air and water motions that exceeded the mean by a factor of  $10^3$  during generation.

## I.B. Description and Scope of the Present Work

The thrust of the present study is toward the investigation of cyclic short wave energy changes, phase related to the long wave, that occur during active generation of the short wave field by wind. To accomplish this objective, experimental measurements of short wave slope time series are made in a laboratory environment where the basic long wave parameters can be controlled as desired and the wind speeds are accurately reproducible. An instrument system, operating on the principle of optical refraction at the air water interface, detects the slope of the interface at a point without disrupting the flow. The slope time series obtained in this manner are digitally analyzed so that the energy present within a specified variance element of the slope spectrum can be observed as a function of reference wind speed and phase location along the long wave profile.

The short wave energy variations along the long wave, determined in this manner, are used to verify a reasonable scheme for prediction of the energy variations based on the Boltzmann transport equation of Hamiltonian mechanics. The short wave frequency range identified as being of particular interest is the band containing all frequencies from 5.00 to 20.00 Hz. Waves in this region tend to be very responsive. That is, they are strongly coupled to the air flow so they exhibit rapid growth rates, and they are strongly coupled to the water motion so they exhibit short interaction times. Variance elements within this range have energy densities that are observed to vary as a function of long wave phase.

## CHAPTER II

### INVESTIGATIONS OF WAVES AND ASSOCIATED ENERGY TRANSFERS

#### II.A. Transfer of Mechanical Energy to Waves Through the Miles-Phillips Mechanism

While casually observing the motion of the ocean surface, one can easily overlook the fact that what is occurring is actually the coupled motion of two media in the region of their common boundary - the air sea interface. The motions are exchanging energy in both directions across the interface. During a wave generation situation, the motion of the water is evolving in space and time because the net flux of energy across the interface is from the air flow to the water flow. Energy is passed from the air to the water through the action of normal and tangential stresses (Kinsman, 1965). Pressure fluctuations at the interface are capable of passing on energy in such a manner that irrotational motion results. Irrotational analyses have been shown to yield considerable simplifications of and good approximations to the water wave problem. For these reasons analytical approaches to the generation of water waves have concentrated on energy flow associated with pressure fluctuations.

Pressure fluctuations are available in the air flow under all conditions to create and to feed the water wave motion. Eddies, passing in the air flow, create local unsteadiness in the pressure regardless of the shape of the water surface. Once the water surface has attained a

wave shape it forces a modification of the air flow streamlines, generating pressure fluctuations. So there are two types of identifiable pressure fluctuations. Based on these different pressure fluctuations, two rather different mechanisms for wave generation have been proposed. These two mechanisms were proposed concurrently, finally combined into one model, and have formed, since the later 1950's, the primary theoretical basis for the prediction of wave generation (Phillips, 1962).

The first mechanism proposes a resonance action between the possible surface wave modes and the eddies convected along by the mean air flow (Phillips, 1957). The equations describing the water motion are linearized, and simplified by assuming inviscid, irrotational flow. The equation of motion for the system is the dynamic free surface boundary condition including surface pressure and surface tension, evaluated at the mean surface level

$$\frac{\partial \phi}{\partial t} + g\eta = \frac{-p}{\rho_w} + \frac{T}{\rho_w} \nabla^2 \eta, \quad (2-1)$$

where

$\phi$  = velocity potential of water motion,

$\eta$  = water surface displacement,

$p$  = surface pressure,

$T$  = surface tension,

and

$\rho_w$  = water density.

Fourier transformation nicely converts the equation, (2-1), to a differential equation in terms of the transformed variables. The variables are written in equations (2-2), (2-3), and (2-4) in terms of their generalized Fourier transforms in space. The equations are

$$n(\underline{x}, t) = \int_{-\infty}^{\infty} A(\underline{k}, t) e^{i(\underline{k} \cdot \underline{x})} d\underline{k} \quad , \quad (2-2)$$

$$p(\underline{x}, t) = \int_{-\infty}^{\infty} P(\underline{k}, t) e^{i(\underline{k} \cdot \underline{x})} d\underline{k} \quad , \quad (2-3)$$

and

$$\phi(x, z, t) = \int_{-\infty}^{\infty} \frac{A'(\underline{k}, t)}{k} e^{kz} e^{i(\underline{k} \cdot \underline{x})} d\underline{k} \quad , \quad (2-4)$$

where a prime indicates a time derivative. The resultant differential equation, is in a form describing a system in forced oscillation

$$A''(\underline{k}, t) + \sigma^2 A(\underline{k}, t) = \frac{-k}{\rho_w} P(\underline{k}, t) \quad , \quad (2-5)$$

where  $\sigma$  is given by the familiar dispersion relation for free surface waves with surface tension included,

$$\sigma^2 = gk + \frac{Tk^3}{\rho_w} \quad . \quad (2-6)$$

The solution of the equation yields, in the form of a convolution integral, the time history of the amplitude of a wave component of wave number,  $\underline{k}$ , as it responds to an atmospheric pressure forcing function that is quite independent of the water motion. The solution is

$$A(\underline{k}, t) = \frac{ik}{2\rho_w \sigma} \int_0^t P(\underline{k}, \tau) [e^{-i\sigma(t-\tau)} - e^{i\sigma(t-\tau)}] d\tau \quad , \quad (2-7)$$

where  $\tau$  is the lag variable. The asymptotic form of the solution for the energy spectrum of the wave displacement,  $\Phi(\underline{k}, t)$ , is developed from the mean product of  $A(\underline{k}, t)$  and  $A^*(\underline{k}', t)$ . Kinsman (1965) formed the mean product with the use of equation (2-7), which yields

$$\phi(\underline{k}, t) = \frac{k^2}{\rho_w^2 \sigma^2} \int_0^t \int_0^t \Pi(\underline{k}, \tau, \tau') \sin \sigma(t - \tau) \sin \sigma(t - \tau') d\tau d\tau' \quad ,$$

after integration over  $k'$  space, and where  $\Pi(\underline{k}, \tau, \tau') \delta(\underline{k} - \underline{k}')$  is defined as  $P(\underline{k}, \tau) P^*(\underline{k}', \tau)$ . If the pressure spectrum,  $\Pi(\underline{k}, \tau, \tau')$  is considered stationary it becomes a function of time separation,  $\tau - \tau'$ , rather than time. Then the integral above transforms the pressure spectrum into the frequency domain. In terms of the energy spectrum of the pressure fluctuations,  $F(\underline{k}, \sigma)$ , the wave energy spectrum is given as

$$\phi(\underline{k}; t) \approx \frac{k^2 t}{4\rho_w^2 \sigma^2} F(\underline{k}, \sigma) \quad , \quad (2-8)$$

which shows the wave energy developing linearly in time. The response of the water surface depends on the magnitude of the pressure fluctuation and the time over which interactions are allowed to occur. For any given angle of wave propagation,  $\alpha$ , relative to the direction of the mean wind, waves that have the phase velocity given by

$$c(k) = U \cos \alpha \quad , \quad (2-9)$$

where  $U$  is the mean wind velocity, have the longest interaction times and largest responses. Every wave of wavenumber,  $k$ , would have a preferred direction,  $\alpha$ . If the input,  $F(\underline{k}, \sigma)$ , were a narrow band function the water wave spectrum would show a local energy maximum at an angle,  $\alpha$ , satisfying equation (2-9) for the phase speed of the wave at the peak of the wavenumber spectrum.

The second mechanism of wave generation relies on the coupling of the air and wave motions to induce the atmospheric pressure fluctuations that force energy to flow to the water motion. Miles (1957) proposed a model that coupled the equations for the flow of both media. The air flow is assumed to be inviscid, incompressible, and to have a mean shear

flow specified by a logarithmic variation with height. The mean flow is perturbed by small two dimensional disturbances induced by the shape of the surface waves. The disturbances are assumed to be small enough to allow linearization of the equations of motion. Turbulent fluctuations, although necessary to maintain the specified velocity profile, are not taken into account in the original problem. The water motion is assumed to be inviscid, irrotational, incompressible, and to have no mean flow. The wave motion itself is considered small amplitude.

From the average of the energy equation one is able to deduce the rate of energy flow per unit area of the interface from the air to the water due to the wave induced Reynolds stress. The flux rate is

$$\frac{dE}{dt} = \rho_a \int_0^{\infty} \overline{uw} \frac{\partial U}{\partial z} dz \quad , \quad (2-10)$$

where

$\rho_a$  = air density,

$U$  = mean horizontal air flow velocity,

$u$  = wave induced contribution to the horizontal air flow velocity,

and

$w$  = wave induced contribution to the vertical air flow velocity.

The Reynolds stress is evaluated as in instability theory. For the inviscid parallel flow assumption, the value is approximated by the expression

$$\rho_a \overline{uw} = \frac{\rho_a \pi}{k} \frac{\overline{w^2}}{w^2} \left. \frac{\partial^2 U / \partial z^2}{\partial U / \partial z} \right|_{z = z_c}$$

for the region  $z < z_c$  and

$$\rho_a \overline{uw} \approx 0 \quad , \quad (2-11)$$

for the region  $z > z_c$ .

The expression above is evaluated at a height,  $z_c$ , the distance above the water surface where  $U(z_c)$  equals the wave phase speed,  $c$ . Substitution of (2-11) into (2-10) yields the value of the rate of energy flow per unit area from the air to the water. The approximate evaluation of the integral in (2-10) is

$$\frac{dE}{dt} \approx - \frac{\pi \rho_a c \overline{w^2}}{k} \left. \frac{\partial^2 U / \partial z^2}{\partial U / \partial z} \right|_{z_c} \quad , \quad (2-12)$$

which needs to be evaluated at  $z_c$  only, and where

$c$  = water wave phase speed,

$k$  = water wave wavenumber,

and

$\overline{w^2}$  = intensity of the vertical velocity fluctuations.

Using the definition of energy for a two dimensional wave field and the deep water gravity wave dispersion relation, one can formulate a normalized rate,  $\zeta$ , of increase in the wave energy from equation (2-12) and the definition

$$\zeta \equiv \frac{1}{\sigma} \frac{dE/dt}{E} \quad , \quad (2-13)$$

where  $\sigma$  = wave radian frequency. Since the energy ratio is multiplied by the time per radian,  $1/\sigma$ , we see that  $\zeta$  yields the fractional increase in energy per radian of change in the wave. For this analysis the energy of the wave system grows at an exponential rate with time. To evaluate the growth rate the inviscid Orr-Sommerfeld equation, which arrives by using a stream function to describe the perturbed flow in the air, must be solved.

Based on the two preceding mechanisms, Miles (1960) developed a model for the wave response when both types of pressure fluctuations are acting. In doing this he modified equation (2-5), which was formulated for the resonance model, to include the wave induced pressure forcing function. Equation (2-5) becomes of the form of equation (2-14),

$$A''(\underline{k}, t) + \sigma^2 A(\underline{k}, t) = - \frac{k}{\rho_w} [P_0(\underline{k}, t) + P_1(\underline{k}, t)] \quad , \quad (2-14)$$

where  $P_0(\underline{k}, t)$  and  $P_1(\underline{k}, t)$  are the turbulent and wave induced pressure fluctuations, respectively. The pressures have been represented in equation (2-14) through the use of the transforms

$$P_0(\underline{x}, t) = \int_{-\infty}^{\infty} P_0(\underline{k}; t) e^{i(\underline{k} \cdot \underline{x})} d\underline{k} \quad ,$$

and

$$P_1(\underline{x}, t) = \int_{-\infty}^{\infty} P_1(\underline{k}; t) e^{i(\underline{k} \cdot \underline{x})} d\underline{k} \quad ,$$

where time remains a parameter. Considering the wave induced pressure field, which is assumed to be

$$P_1(\underline{x}, t) = (a + ib) \rho_w c^2 k \eta(\underline{x}, t) \quad ,$$

it can be said that only the component in phase with the downward surface velocity will do work on the wave. The component of interest is then the one proportional to that velocity, since it is wave induced. This pressure may be represented as

$$P_1(\underline{k}, t) = -\alpha A'(\underline{k}, t) \quad . \quad (2-15)$$

The energy equation, when integrated over the water column, contains the term,  $-P_\eta(\partial\eta/\partial t)$ , which specifies the rate of energy input to the wave

motion due to the atmospheric pressure at the surface,  $P_\eta$ . In spectral terms the mean rate of energy input due to the wave induced pressure of equation (2-15) can be written as

$$-\overline{P_\eta \frac{\partial \eta}{\partial t}} = \alpha \overline{A'(\underline{k}, t) A'^*(\underline{k}, t)} = \alpha \overline{\eta^2}, \quad (2-16)$$

where the use of the complex conjugate of the surface height is allowed because the surface height is a real quantity.

The evaluation of  $\alpha$  comes from directly equating the mean rate of energy input of equation (2-16) to Miles' original result in equation (2-12), where only wave induced pressure was considered. Solving the relationship for  $\alpha$  yields

$$\alpha \approx \frac{\left[ \frac{\pi \rho_a c w^2}{k} \frac{\partial^2 U / \partial z^2}{\partial U / \partial z} \right]_{z_c}}{\overline{\eta^2}}, \quad (2-17)$$

which can then be used to represent the pressure in terms of the wind and wave parameters. In terms of the normalized energy growth rate,  $\zeta$ ,  $\alpha$  is given by

$$\alpha = -c \rho_w \zeta, \quad (2-18)$$

where  $\zeta$  is defined by equation (2-13). Then the equation of motion, (2-14), can be written as

$$A''(\underline{k}, t) + \zeta \sigma A'(\underline{k}, t) + \sigma^2 A(\underline{k}, t) = -\frac{k}{\rho_w} P_0(\underline{k}, t), \quad (2-19)$$

where  $P_0$  is the only external force. From the solution of this problem the energy spectrum of the water surface elevation can be developed. The asymptotic solution for  $t$  much greater than the turbulence time

scale yields

$$\Phi(\underline{k}; t) \approx \frac{k^2}{4\rho_w^2 \sigma^2} \frac{e^{\zeta\sigma t} - 1}{\zeta\sigma} F(\underline{k}, \sigma) \quad , \quad (2-20)$$

where  $\Phi(\underline{k}; t)$  is the wave height energy spectrum with time as a parameter. It is evident that the energy spectrum, depending on the duration, can grow linearly as with a purely resonant interaction, or exponentially as with the shear flow model. The power series expansion of the exponential term of equation (2-20) is

$$\frac{e^{\zeta\sigma t} - 1}{\zeta\sigma} = t + \frac{\zeta\sigma t^2}{2} + \dots \quad , \quad (2-21)$$

which yields the two following time dependencies of

$$\Phi(\underline{k}; t) \propto t \quad \text{for} \quad \frac{\zeta\sigma t}{2} \ll 1 \quad ,$$

and

$$\Phi(\underline{k}; t) \propto e^{\zeta\sigma t} \quad \text{for} \quad \frac{\zeta\sigma t}{2} \gg 1 \quad .$$

Neither of these two fundamental mechanisms are able to adequately explain the formation and growth of short gravity and capillary waves. Turbulent pressure fluctuations cannot be expected to excite disturbances of short wavelength because the turbulent fluctuations of correspondingly short wavelengths are not energetic enough, and are convected downstream too rapidly to account for the straight crested waves observed. The inviscid shear flow mechanism cannot supply enough energy to capillary waves to overcome the laminar dissipation associated with the waves (Miles, 1962). Miles (1962) investigated the importance of a mechanism formulated by Benjamin (1959) with regard to short waves. In this mechanism the energy transfer to the waves results from the presence of a stress term which Miles called the viscous Reynolds stress. This

stress enters the problem through Benjamin's formulation of the equation governing small perturbations in the aerodynamic viscous shear flow. The aerodynamic viscous flow is assumed to be parallel and incompressible. The velocity profile is assumed to be linear within the viscous sublayer and asymptotically logarithmic at larger elevations. The water motion is considered to be inviscid, incompressible, and irrotational. An eigenvalue problem is solved for the wave phase speed. The phase speed turns out to be a complex value,  $(c_r + ic_i)$ , which leads to a growth rate of  $kc_i$  due to consideration of the wave amplitude

$$\eta = ae^{[kc_i t + i k(x - c_r t)]}, \quad (2-22)$$

where the complex value has been substituted. The results of the analysis indicate growth rates increasing rapidly with increasing wind speed and decreasing wavelength. This mechanism predicts rapid growth of short waves having lengths 1 to 3 cm under the action of wind.

## II.B. Interactions Among Components of a Wave System

The complexity of the wave development process arises from the fact that the process is composed of several more or less equally important components which are not well enough defined to be separable from one another. The process of wave development contains generative and degenerative components corresponding to energy flow to and loss from the organized motion of the waves, respectively. Analyses that attempt to predict the growth rate of a wave component based on energy inflow from the air stream have been mentioned previously. Analysis of the decay rate of a wave component is based on the estimation of the nonconservative dissipative mechanism such as breaking, turbulent stress, and viscous stress.

The aforementioned mechanisms deal with energy fluxes to a single wave component of a discretized spectrum. Of course, waves rarely exist in a solitary situation. Rather, many wave motions of various characteristics combine to form a wave system. It is on the complete wave system that the net result of the process of wave development is observable. Because the wave system and growth process are each made up of so many parts and are imperfectly understood, we must resort to a spectral representation of the system for its study. When the system is broad banded, that is consisting of more than a single spectral component, the process of wave development contains interactive mechanisms in addition to generative and degenerative mechanisms. These interactions result in the conservative transfer of energy among two or more wave components contained within the wave spectrum.

The interactive mechanisms and their effects are discussed below. All of these mechanisms assume the motion of the wave system to be

essentially linear with only small corrections required in the mathematical formulations. This approach seems justified by the generally good results obtained through the application of the purely linear theory.

### II.B.1. Tick Second Order Perturbation of the Wave Spectrum

Tick (1959) attempted to remove a deficiency from the use of the analytical first order spectrum to represent a natural wave field. The deficiency is due to the representation of a nonlinear process with a linear statistic. Tick's solution to this problem resulted in a theoretical spectral calculation given by the linear combination of the first order spectrum and a second order correction term.

The wave motion is assumed to be the two dimensional, irrotational flow of an inviscid, incompressible, infinitely deep fluid. As such, he applied the potential flow formulation retaining all terms up through second order in wave height. The kinematic and dynamic free surface boundary conditions are expanded as Taylor series about the mean surface,  $z = 0$ . The equation defining the problem results from the combination and perturbation of these two equations. The equation of the free surface is  $z = \eta(x,t)$ . A velocity potential,  $\phi(x,z,t)$ , that satisfies the Laplace equation is assumed to exist for the flow. The Laplace equation is

$$\frac{\partial^2 \phi}{\partial x^2} + \frac{\partial^2 \phi}{\partial z^2} = 0 \quad , \quad (2-23)$$

where the  $z$  axis is the vertical, and originates at the mean surface level. The bottom boundary condition restricts the vertical velocity

$$w = \frac{\partial \phi}{\partial z} = 0 \quad \text{at} \quad z = -\infty \quad , \quad (2-24)$$

where  $w$  is the vertical velocity. Surface stresses are not considered, so pressure and surface tension are taken as zero. The dynamic free surface boundary condition to second order may be written as

$$gz + \frac{\partial \phi}{\partial t} + \frac{1}{2} \left[ \left( \frac{\partial \phi}{\partial x} \right)^2 + \left( \frac{\partial \phi}{\partial z} \right)^2 \right] = 0 \quad \text{at} \quad z = \eta(x,t) \quad , \quad (2-25)$$

where  $\eta(x,t)$  is the vertical surface position. The kinematic free surface boundary condition is

$$\frac{\partial \phi}{\partial z} = \frac{\partial \eta}{\partial t} + \frac{\partial \phi}{\partial x} \frac{\partial \eta}{\partial x} \quad \text{at} \quad z = \eta(x,t) \quad (2-26)$$

to second order. The surface boundary conditions are Taylor series expanded about the mean surface elevation,  $z = 0$ . The velocity potential and surface elevation are approximated as the sum of the first and second order components,

$$\phi = \phi^{(1)} + \phi^{(2)} \quad ,$$

and

$$\eta = \eta^{(1)} + \eta^{(2)} \quad . \quad (2-27)$$

Combining the expanded and perturbed surface conditions yields the second order equation governing the wave motion. The combined free surface boundary condition is

$$\begin{aligned} \phi_{tt}^{(2)} + g\phi_z^{(2)} &= \phi_t^{(1)}\phi_{zz}^{(1)} - 2\phi_x^{(1)}\phi_{xt}^{(1)} - \phi_z^{(1)}\phi_{zt}^{(1)} \\ &+ \frac{1}{g} [\phi_{zt}^{(1)}\phi_{tt}^{(1)} + \phi_t^{(1)}\phi_{ttz}^{(1)}] \quad \text{at} \quad z = 0 \quad . \end{aligned} \quad (2-28)$$

The two velocity potentials may be represented by their generalized Fourier transforms, since the surface elevation is assumed to be a homogeneous, stationary, random process. The first order problem is solved after the transformation. The nonlinear problem is solved by Fourier transformation. In the nonlinear product terms of the second

order problem Tick used two variables of integration,  $\sigma'$  and  $\sigma''$ , in the Fourier transformation. In this way he was able to solve the nonlinear problem by stepping through the integration required by the linear solution method. What arises from the problem is a second order correction to the spectrum produced by the first order spectrum interacting with itself. The correction to the frequency spectrum is given as

$$\phi^{(2)}(\sigma) = \frac{1}{g^2} \int_{-\infty}^{\infty} K(\sigma', \sigma) \phi^{(1)}(\sigma - \sigma') \phi^{(1)}(\sigma') d\sigma' \quad , \quad (2-29)$$

where

$$K(\sigma'; \sigma) = \begin{cases} \sigma'^2(\sigma^2 - 2\sigma\sigma' + 2\sigma') & 0 < \sigma' < \sigma, \sigma > 0 \\ (\sigma - 2\sigma')^2 \sigma\sigma' & \sigma' < 0, \sigma' > \sigma, \sigma > 0 \end{cases} \quad ,$$

for the given regions of the  $\sigma, \sigma'$  plane. Equation (2-29) indicates the nonlinear effect quite clearly. Since the expression for  $\phi^{(2)}(\sigma)$  is a convolution operation, we see that for a continuous function,  $\phi^{(1)}(\sigma)$ , every contribution to  $\phi^{(2)}$  in a band around  $\sigma$  contains an effect from the first order energy at every other frequency in the spectrum. The result on the spectral shape is the production of a small bump at a frequency about twice that of the wind wave peak.

### II.B.2. Benjamin and Feir Side Band Interactions

Benjamin and Feir (1967) discussed the existence of side band interactions. This idea can account for the change in shape of a sinusoid as it proceeds, unperturbed by external effects, from its point of origin. This is accomplished by passage of energy from the basic frequency to its side band frequencies, which are present in infinitesimal proportion from the point of origin of the basic wave. This interesting

result eliminates the possibility of the existence of a wave of permanent form.

The flow is considered to be two dimensional, irrotational motion in an inviscid, incompressible fluid of infinite depth. The mean surface level is at  $z = 0$ , and the equation of the free surface is  $z = \eta(x,t)$ . The potential flow problem is formulated in the usual way. A velocity potential,  $\phi(x,z,t)$ , satisfies the Laplace equation. There is assumed to be no motion at infinite depth. The dynamic free surface boundary condition yields the condition for constant interfacial pressure with surface tension not included. The boundary value problem is specified by the Laplace equation

$$\nabla^2 \phi(x,z,t) = 0 \quad , \quad (2-30)$$

the bottom boundary condition

$$\nabla \phi(x,z,t) = 0 \quad \text{at} \quad z \rightarrow -\infty \quad , \quad (2-31)$$

the kinematic free surface condition

$$\eta_t + \eta_x \phi_x - \phi_z = 0 \quad \text{at} \quad z = \eta \quad , \quad (2-32)$$

and the dynamic free surface condition

$$gz + \phi_t + \frac{1}{2} (\phi_x^2 + \phi_z^2) = 0 \quad \text{at} \quad z = \eta \quad . \quad (2-33)$$

The Stokes solution to the nonlinear boundary value problem is perturbed according to the form of small side band modes of oscillation and substituted back into the boundary value problem specified by equations (2-30) to (2-33). A new boundary value problem in the perturbation variables results, the solution of which indicates the direction and rate of energy flux to the side band components of the oscillating system. The Stokes solution to the original problem to the order required for this problem is given by

$$\eta = N = a \cos \chi + \frac{1}{2} ka^2 \cos 2\chi \quad , \quad (2-34)$$

and

$$\phi = \Phi = \frac{\sigma}{k} ae^{kz} \sin \chi \quad , \quad (2-35)$$

where  $\chi = kx - \sigma t$  is the phase function of the primary wave. The expressions for velocity potential and surface level perturbed around the Stokes solution in the ordering parameter,  $\epsilon$ , are given as

$$\phi = \Phi + \epsilon \tilde{\phi} \quad , \quad (2-36)$$

$$\eta = N + \epsilon \tilde{\eta} \quad . \quad (2-37)$$

Substitution of equations (2-36) and (2-37) into the boundary value problem equations, yields the new boundary value problem specified as the Laplace equation

$$\nabla^2 \tilde{\phi}(x, z, t) = 0 \quad , \quad (2-38)$$

the bottom boundary condition

$$\nabla \tilde{\phi} = 0 \quad \text{at} \quad z \rightarrow -\infty \quad , \quad (2-39)$$

the kinematic free surface condition

$$\tilde{\eta}_t + \tilde{\eta}_x \Phi_x + \tilde{\eta}(-\Phi_{zz} + N\Phi_{xz}) + (-\tilde{\phi}_z + N_x \tilde{\phi}_x) = 0 \quad \text{at} \quad z = N \quad , \quad (2-40)$$

the dynamic free surface condition

$$g\tilde{\eta} + \tilde{\eta}(\Phi_x \Phi_{xz} + \Phi_z \Phi_{zz} + \Phi_{tz}) + (\tilde{\phi}_t + \Phi_x \tilde{\phi}_x + \Phi_z \tilde{\phi}_z) = 0 \quad \text{at} \quad z = N \quad (2-41)$$

where terms of order higher than  $\epsilon$  are not included, and the factors represented in upper case letters are known.

The solution to the new perturbation problem is assumed to consist of the sum of a pair of side band modes symmetrically located on each

side of the primary wave in phase and the results of the side band interactions with the primary wave. The solution for wave height takes the form

$$\tilde{\eta} = \tilde{\eta}_1 + \tilde{\eta}_2 \quad , \quad (2-42)$$

where for each of the two side band modes we have

$$\begin{aligned} \tilde{\eta}_i &= b_i \cos X_i \\ &+ akb_i [A_i \cos (X + X_i) + B_i \cos (X - X_i)] \\ &+ O[a^2 k^2 b_i] \quad , \end{aligned} \quad (2-43)$$

where  $b_i$  are the side band amplitudes, and the phases are

$$X_1 = k(1 + \alpha) x - \sigma(1 + \delta) t - \gamma_1 \quad ,$$

and

$$X_2 = k(1 - \alpha) x - \sigma(1 - \delta) t - \gamma_2 \quad ,$$

where  $\alpha$  and  $\delta$  are much less than one. The results of the analysis indicate that under certain conditions the side band amplitudes,  $b_i$ , will grow in time in an unbounded manner. If the perturbation,  $\delta$ , about the primary wave frequency is within the limits given in equation (2-44) the Stokes wave will not maintain a permanent form, because its side band modes will draw energy from it. The frequency spread allowing interaction is

$$0 < \delta \leq \sqrt{2}ka \quad . \quad (2-44)$$

The value of  $\delta$  yielding maximum growth rate was found to be within these limits, at  $\delta = ka$ . If there were minor oscillations present at a frequency in the neighborhood of the primary wave frequency, then the waves satisfying the gravity wave dispersion relation and with frequencies,  $\sigma_i = \sigma(1 \pm ka)$  and therefore wave numbers,  $k_i = k(1 \pm 2ka)$ , would

project energy at the group velocity of the primary wave and be selectively amplified.

### II.B.3. Phillips Resonant Interaction Among Gravity Waves

Phillips (1960) found an interaction of the third order in wave amplitude among three wave components that results in an energy transfer from them to a fourth new wave producing a growth in it that is linear in time. Initially of third order in amplitude, the new wave could reach a magnitude of the same order as the original three waves. In this conception the spectrum is still discretized, has become somewhat broad banded, yet by assumption is limited to the wave motions controlled by gravity. Phillips investigated the interaction of pairs of infinite sinusoidal wave trains of small amplitude. These primary waves are solutions to the linear equations of potential flow theory. The nonlinear terms of the potential flow equations produce traveling sinusoidal pressure and velocity fields with wave number and frequency equal to the sum or difference of the wave numbers and frequencies of the primary waves and with amplitudes proportional to the product of the primary wave amplitudes. If the frequency of an infinitesimal free wave happens to be the same as that of the nonlinear fields of the same wavenumber, resonance will occur and the free wave will be forced.

Phillips assumed an irrotational motion in an inviscid, incompressible fluid of infinite depth. The wave numbers are allowed to be vector quantities, so the wave propagation directions in the x-y plane are not restricted. The z axis is vertically oriented with  $z = 0$  at the mean water level. A velocity potential,  $\phi(x,y,z,t)$ , does then exist that satisfies Laplace's equation. It defines a three dimensional

velocity vector,  $\underline{V} \equiv \underline{\nabla}\phi$ . The kinematic and dynamic free surface boundary conditions are combined. The combined equation is assumed continuously valid and extended to the local surface,  $z = \eta(x,y,t)$ , through Taylor expansion, from the mean water level. The resultant equation before Taylor expansion, when the surface pressure is assumed constant, is given as

$$\frac{\partial^2 \phi}{\partial t^2} + g \frac{\partial \phi}{\partial z} + \frac{\partial}{\partial t} \underline{V}^2 + \underline{V} \cdot \underline{\nabla} \frac{1}{2} \underline{V}^2 = 0 \quad \text{at} \quad z = \eta \quad , \quad (2-45)$$

which arises as the difference between the material derivative of the dynamic condition and  $g$  times the kinematic condition. Note that the cubic terms resulting from the material derivative are retained, due to the necessity of finding an effect at third order. Each variable is perturbed with the first order terms being the first order approximation to the effective wave system created by two intersecting wave motions.

In Kinsman's (1965) notation, the perturbations are

$$\phi = (\alpha\phi_{10} + \beta\phi_{01}) + (\alpha^2\phi_{20} + \alpha\beta\phi_{11} + \beta^2\phi_{02}) + \dots \quad , \quad (2-46)$$

$$\underline{V} = (\alpha\underline{V}_{10} + \beta\underline{V}_{01}) + (\alpha^2\underline{V}_{20} + \alpha\beta\underline{V}_{11} + \beta^2\underline{V}_{02}) + \dots \quad , \quad (2-47)$$

and

$$\eta = (\alpha\eta_{10} + \beta\eta_{01}) + (\alpha^2\eta_{20} + \alpha\beta\eta_{11} + \beta^2\eta_{02}) + \dots \quad . \quad (2-48)$$

The coefficients,  $\alpha$  and  $\beta$ , are small and proportional to the surface slope of the wave they refer to. The solutions to the first approximation in the perturbation problem are the familiar linear wave solutions given as

$$\eta_{10} = a_1 \cos \chi_1 \quad , \quad (2-49)$$

$$\phi_{10} = \frac{a_1 \sigma_1}{k_1} e^{k_1 z} \sin \chi_1 \quad , \quad (2-50)$$



The behavior of  $\phi_{21}$ , as the solution to equation (2-53), indicates the behavior of a wave of frequency,  $2\sigma_1 - \sigma_2$ , which can receive energy from the combination of waves identified by wavenumbers,  $\underline{k}_1$ ,  $\underline{k}_2$ , and  $\underline{k}_3$ , where in this case  $\underline{k}_3 = \underline{k}_1$ . It turns out that on the right hand side of equation (2-53) there are terms containing the phase function,  $2\chi_1 - \chi_2$ . So resonant excitation of  $\phi_{21}$  does occur. The corresponding surface elevation,  $\eta_{21}$ , grows linearly in time as

$$\eta_{21}(x,y,t) \approx \frac{Kt}{2g} \sin(2\chi_1 - \chi_2) \quad , \quad (2-54)$$

where  $K$  is a constant depending on the amplitudes, wavenumbers, and frequencies of the primary waves.

In general the resonant interaction excites a new wave at wave-number and frequency,  $\underline{k}_4$  and  $\sigma_4$ , respectively, that grows linearly in amplitude with time. For this to occur the wavenumbers and frequencies must bear the following relationships to one another

$$\underline{k}_1 + \underline{k}_2 + \underline{k}_3 + \underline{k}_4 = 0 \quad (2-55)$$

and

$$\sigma_1 + \sigma_2 + \sigma_3 + \sigma_4 = 0 \quad , \quad (2-56)$$

where each wave obeys its own dispersion relationship,

$$\sigma_i^2 = g|\underline{k}_i| \quad . \quad (2-57)$$

Analytically, this theory suffers difficulties because the wave that begins at third order and is assumed to be of third order, is able to grow as large as the primary components. Phillips did not consider the energy balance between the interacting components.

In separate experiments Longuet-Higgins and Smith (1966) and McGoldrick et al. (1966) tested out the possibility of a resonant interaction of the type suggested by Phillips. In both cases the environment

was reduced to that of two mutually perpendicular primary wave trains. Both experiments took place in rectangular wave tanks. McGoldrick's apparatus was built with special attention given to the elimination of external effects that would mask the measurement. For the interaction geometry the production of a tertiary wave of frequency  $2\sigma_1 - \sigma_2$  was expected when the primary wave frequency ratio was,  $\sigma_1/\sigma_2 = 1.7357$ . Both tests found tertiary wave generation to occur and to closely follow the theoretical growth rate when the resonance condition was met.

#### II.B.4. McGoldrick Resonant Interaction Among Capillary - Gravity Waves

McGoldrick (1965) modified the resonance problem to include waves from a broader band so that surface tension effects could be included. He found an interaction at the second order in this case that is more physically satisfying than Phillips' result because he considered the balance of energy among the interacting components. His analysis resulted in a group of three discrete waves exchanging energy among themselves. The amplitudes of all three waves are of the same order, and in its turn, each individual wave grows at the expense of the others. The process repeats itself cyclicly.

McGoldrick assumed a three dimensional, irrotational motion in an inviscid, incompressible fluid of infinite depth. The vertical axis,  $z$ , equals zero at the mean water level. The actual surface is considered to be composed of three waves. The equation of the surface is

$$z = \eta(x, y, t) = \sum_{i=1}^3 \eta_i(x, y, t) \quad .$$

The combined free surface boundary condition defines the problem, as usual. The equation below is the same as equation (2-45) used by

Phillips with additional terms considered to allow for the surface pressure variations due to surface tension. The combined condition is

$$\frac{\partial^2 \phi}{\partial t^2} + g \frac{\partial \phi}{\partial z} + \frac{\partial(\underline{v}^2)}{\partial t} + \underline{v} \cdot \underline{\nabla} \left( \frac{1}{2} \underline{v}^2 \right) - \frac{T}{\rho_w} \left[ \frac{\partial(\nabla^2 \eta)}{\partial t} + \underline{v} \cdot \underline{\nabla}(\nabla^2 \eta) \right] = 0 \quad \text{at} \quad z = \eta, \quad (2-58)$$

where the additional terms allow for the consideration of surface pressure variation due to surface tension. The equation is not perturbed in this analysis, but it is extended by Taylor series to the surface from  $z = 0$ , and terms through second order are retained. A first order potential function that satisfies Laplace's equation, equation (2-58), and the bottom boundary condition

$$\underline{v}(x, y, z, t) = 0 \quad \text{at} \quad z = -\infty, \quad (2-59)$$

is written

$$\phi(x, y, z, t) = \sum_{i=1}^3 \frac{\sigma_i}{k_i} a_i(t) e^{k_i z} \sin \chi_i, \quad (2-60)$$

where

$$\chi_i = k_i x - \sigma_i t + \epsilon_i$$

is the phase function.

The corresponding expression for the surface is

$$\eta(x, y, t) = \sum_{i=1}^3 a_i(t) \cos \chi_i. \quad (2-61)$$

Equations (2-60) and (2-61) are substituted into the combined and kinematic surface conditions. The wave amplitudes are considered to be slowly varying functions of time, so second order time derivative terms

are neglected. Three differential equations for the three amplitudes,  $a_i(t)$ , result. Each equation is integrated directly in terms of Jacobian elliptic functions with real parameters. The set of solved equations represent a coupled system of three waves in which energy flows periodically into and out of each component from the others. The solutions are bounded, satisfy conservation of energy, and have no analytical difficulties concerning wave size or time range of solution.

The conditions for the resonance interaction to occur require only three waves and are

$$\underline{k}_1 \pm \underline{k}_2 = \pm \underline{k}_3 \quad , \quad (2-62)$$

and

$$\sigma_1 \pm \sigma_2 = \pm \sigma_3 \quad , \quad (2-63)$$

where each wave satisfies

$$\sigma_i^2 = gk_i + \frac{T}{\rho_w} k_i^3 \quad . \quad (2-64)$$

It is seen that if the  $\underline{k}_3$  corresponding to  $\underline{k}_1 \pm \underline{k}_2$  produces a  $\sigma_3$ , calculated by equation (2-64), that equals  $\sigma_1 \pm \sigma_2$ , resonance will occur.

#### II.B.5. Hasselmann Fifth Order Nonlinear Interchange

Hasselmann (1962) extended the perturbation type of analysis to a truly continuous wave spectrum. For the first time the mathematics represented the nonlinear energy transfer in an ocean wave spectrum. The assumptions limit the wave motions in the theory to those of gravity waves. The transfer of energy in a gravity wave spectrum was found to be of third order in the wave energy. In the extension to a continuous spectrum Hasselmann had to resort to a fifth order analysis in wave

amplitude because it contains the nonstationary quantity that leads to the resonant interaction. Hasselmann (1963) calculated that energy flows from intermediate frequencies to lower and higher frequencies.

The problem is assumed to be one of irrotational motion of an inviscid, incompressible, infinitely deep fluid. As such, a potential function exists that satisfies the potential flow problem. The potential function and corresponding surface elevation are used in the form of the generalized Fourier transforms given by

$$\phi(x,y,z,t) = \int_{-\infty}^{\infty} A(\underline{k};x,y,z,t) e^{kz} e^{i(\underline{k} \cdot \underline{x})} d\underline{k} \quad , \quad (2-65)$$

and

$$\eta(x,y,t) = \int_{-\infty}^{\infty} B(\underline{k};x,y,t) e^{i(\underline{k} \cdot \underline{x})} d\underline{k} \quad . \quad (2-66)$$

The problem, which starts with the perturbation of the combined surface condition, is not restricted to two dimensions. The linear motions are assumed to be statistically independent, so that the first order spectrum completely describes the surface. This property allows all energy fluxes to be represented in terms of the first order spectrum.

The resonant energy transfer could occur among four wave components given the same set of conditions given by Phillips in equations (2-55) through (2-57). Hasselmann (1962) found that an interaction does occur when

$$\underline{k}_1 + \underline{k}_2 = \underline{k}_3 + \underline{k}_4 \quad , \quad (2-67)$$

and

$$\sigma_1 + \sigma_2 = \sigma_3 + \sigma_4 \quad . \quad (2-68)$$

The energy transfer is the cubic function of the two dimensional first order energy spectrum,  $\phi(\underline{k}; \underline{x}, t)$ , given by

$$S_{nl} = \iiint_{-\infty}^{\infty} T(\underline{k}_1, \underline{k}_2, \underline{k}_3, \underline{k}_4) (\sigma_4 \phi_1 \phi_2 \phi_3 + \sigma_3 \phi_1 \phi_2 \phi_4 - \sigma_2 \phi_1 \phi_3 \phi_4 - \sigma_1 \phi_2 \phi_3 \phi_4) \delta(\sigma_4 + \sigma_3 - \sigma_2 - \sigma_1) dk_{x_1} dk_{y_1} dk_{x_2} dk_{y_2} \quad (2-69)$$

The subscripts on the spectra are a shorthand notation indicating at which of the wavenumbers the spectral values are to be taken. The transfer coefficient,  $T$ , is a lengthy function of only the wavenumbers. The Dirac delta function only allows contributions to the integral from the appropriate resonant conditions.

The effect of the interaction is to redistribute the energy toward the formation of a more uniform spectrum. That is, peaks would tend to be removed in favor of a white noise spectrum.

#### II.B.6. Valenzuela Capillary - Gravity Wave Resonant Interaction

Valenzuela and Laing (1972) pursued a Hasselmann type of analysis where capillary waves were allowed. The formulation of the problem is exactly the same as Hasselmann's, except for the consideration of surface tension. The interaction was found to be more pronounced with only a third order analysis in wave amplitude needed to calculate the unsteady term in the second order energy, that creates the energy flux.

The interactions are known as sum or difference resonances depending upon which of the following conditions are met

$$\underline{k}_3 = \underline{k}_2 + \underline{k}_1 \quad \text{and} \quad \sigma_3 = \sigma_2 + \sigma_1 \quad , \quad (2-70)$$

or

$$\underline{k}_3 = \underline{k}_2 - \underline{k}_1 \quad \text{and} \quad \sigma_3 = \sigma_2 - \sigma_1 \quad , \quad (2-71)$$

where each wave satisfies the dispersion relation. The resultant interaction is expressed in terms of the products of two first order spectra as

$$\begin{aligned}
 S_{nl} = & \iint_{-\infty}^{\infty} T(\underline{k}_1, \underline{k}_2, \underline{k}_3) (\sigma_3 \phi_1 \phi_2 - \sigma_2 \phi_1 \phi_3 - \sigma_1 \phi_2 \phi_3) \delta(\sigma_3 - \sigma_2 - \sigma_1) dk_{x_1} dk_{y_1} \\
 & + 2 \iint_{-\infty}^{\infty} T(\underline{k}_1, \underline{k}_2, \underline{k}_3) (\sigma_3 \phi_1 \phi_2 - \sigma_2 \phi_1 \phi_3 + \sigma_1 \phi_2 \phi_3) \delta(\sigma_3 - \sigma_2 + \sigma_1) dk_{x_1} dk_{y_1} \\
 & \dots \dots \dots (2-72)
 \end{aligned}$$

As before, the subscripts on the energy spectra indicate the appropriate wavenumber of evaluation, and the transfer coefficients are lengthy relationships between  $\underline{k}_1, \underline{k}_2$ , and their associated frequencies.

The results of the analysis predict an energy flow from the region of waves of minimum phase speed to both gravity and capillary waves.

## II.C. Experimental Studies of High Frequency Waves

The experimental investigation of waves of short and intermediate length did not begin in earnest until the 1950's. Short waves were neglected prior to that time, not because they were not noticed or considered irrelevant, but because the measurement and statistical tools required to facilitate their study had not been developed. By the middle 1950's the scientific environment was becoming conducive to the many investigations which were to follow.

Using a photographic, optical reflection method, Cox and Munk (1954) and Schooley (1954) studied the statistical distribution of wave slopes in two dimensions as a function of wind velocity. When a portion of the water surface attains an appropriate slope angle it will reflect a glitter of light from some overhead light source into a receiver. Knowing the true angle between the source and the receiver, one is able to infer the slope angle creating the reflection. Cox and Munk photographed the glitter patterns from an airplane, using the sun as the source of illumination, principally to measure mean square surface slope. Schooley illuminated the surface with flashbulbs held 45 feet above the water surface at night. Taking the glitter statistics as representative of the slope distribution statistics, Cox and Munk (1954) found the slope distributions to be nearly Gaussian and the rms value in radians to be  $\tan 16^\circ$  at a 14 m/s wind speed (Munk, 1955). The crosswind distribution was slightly more peaked than Gaussian. The upwind - downwind distribution was slightly peaked and skewed 2.5 degrees upwind. The skewness is thought to be due to the effect of wind stress on the wave slope (Kinsman, 1965). The value of the distribution functions fall to near zero by the slope values of  $\pm 25^\circ$ . The mean square slope

value was found to increase linearly with wind speed from 9.5 m/s to 13.8 m/s. Wentz (1976) showed that Cox and Munk overextended their data to estimate the surface variance. He proposed that a more realistic estimate would be a lower bound variance given by 0.8 times the Cox and Munk value.

Subsequent to Munk's study, Schooley (1955) measured wave curvature photographically in a small wind-wave tank to develop size distribution information. He used the reflection method and considered glitter area as well as angle. Approximating the glitter facets of the surface as spherical reflectors, he found the average radius of curvature to be greater across the wind than in line with the wind. He also found a minimum mean wind required for wave generation in his tank to be 3.6 m/s. Up to this point time series of short waves had not been investigated.

Cox (1958) performed a series of experiments in a model wind-wave tank that were designed specifically to investigate short waves. Using an optical refraction measurement technique, he measured wave slope time series. The source of illumination was located beneath the water surface, and was of variable intensity along the axis of measurement. The light receiver was located above the water surface and focused at a point on the surface. The surface slope at the point of focus then controlled the position of origin of the light beam, and therefore, the intensity of the light beam received. Hence the light intensity was related to the surface slope.

Of particular interest to the present experiment are the wave slope spectra calculated and the slope time series displayed for the case when a mechanically generated swell is present in combination with the wind driven wave system. The wind wave spectra, as well as the time series, identify the wave system as having two scales of motion separated in

frequency space by about an order of magnitude. In addition, he found that when the wind is strong enough to generate regular, large scale waves the small scale waves congregate on the front face of the longer waves. Cox generated large free gravity waves mechanically and found that capillary waves were present on the front face of the long waves even when no wind was blowing. The addition of wind enhanced the capillary wave amplitudes, but they remained concentrated on the long wave forward faces until the mean wind speed exceeded at least 9 m/s. Finally, Cox exhibited the wind speed dependence of wave slope through the spectral representation of the wave system and its integral. The mean square slope increases rapidly with increasing wind speed, corresponding to a systematic increase in peak slope energy. However, at frequencies higher than the peak region the spectral energy does not show a systematic dependence on wind speed.

Wu et al. (1969) devised an optical reflection instrument for use in a wind-wave tank that measured discrete occurrences of a given surface slope and curvature in a given time interval. Time series could not be generated, so the wave analysis is of a probabilistic nature only. Wu (1971) illustrated the slope distribution functions calculated from his data. The function shapes are generally Gaussian for each wind speed. However, at the lower wind speeds skewness occurs toward slope angles favored by the orientation of the forward face of the long waves. As the wind speed increases, the skewness goes to zero. The skewness indicates a high concentration of very short waves on the forward face of the long wave that becomes a more uniform concentration along the profile with increasing wind speed. The maximum skewness occurred at a mean wind speed of 5 m/s. At the higher mean wind speeds the distribution function becomes peaked. Wu attributed this to wave breaking.

Wu (1975) proceeded to the problem of the measurement of short wave slope distributions in the presence of a mechanically generated long wave. He calculated the fractions of the total number of capillaries that occurred at various positions on the long wave profile. The maximum capillary activity concentrated on the forward face of the long wave. Only four wind speeds from 4.2 m/s to 12.3 m/s were tested. The front face dominance had a maximum at 7 m/s and decreased elsewhere. His results for other segments of the long wave did not show clear trends with wind speed.

At the University of Florida Shemdin et al. (1972) recorded wave slope time series, using an optical refraction measurement system. The statistics were based on the large scale magnitude of time, over which they were assumed to be stationary. The wind wave slope spectra exhibited a shift in the peak to lower frequencies and higher values with increasing wind speed, as the height spectra do. Spectral observations showed that the intensity of high frequency waves, for example 20 Hz, increased linearly with mean wind speed from 5 to 10 m/s. Short wave intensities at somewhat lower frequencies, for example 8 Hz, were beginning to saturate at a reference wind as low as 7 m/s. It was found that the addition to the wave system of a larger scale, mechanically generated wave produced a reduction in the wind wave peak value, which was in the vicinity of 3 Hz, and somewhat of an increase in the energy levels above 5 Hz.

Long and Huang (1975) described an optical device they had constructed for the detection of wave slopes in a wind-wave tank. The instrument operates on the refraction principle. The position of a laser beam after refraction at the surface is sensed in one dimension by an array of parallel photodiode strips. Each strip responds to the

presence of the laser beam with a different output voltage. The receiving array has 19 elements, allowing 19 angles of slope measurement. The discretized electrical output of the array is then a step approximation to the true wave slope. This approach introduces a large quantity of high frequency energy into the spectral computation. The mean square slope values obtained for mean winds of 3 to 5 m/s are comparable to the values of Cox (1958) and Wu (1971), and increase with wind speed. In the range 5 to 10 m/s the values obtained by Long and Huang are higher than in the earlier studies and maintain a rather constant value over the wind speed changes.

The nonphotographic, optical devices used for the measurement of wave slopes all require a transducer to convert an optical signal to a continuous electrical signal. Two devices have been employed in the previously mentioned experiments. A direct discrete measurement can be obtained with an array of photodiode devices. A measurement based on the intensity value of the optical signal can be obtained with a photomultiplier and optical attenuator. A third type of device, used in this experimental investigation, is a continuous Schottky diode that measures optical position directly. Each method has weaknesses. The diode array provides only a discontinuous signal, the attenuator and photomultiplier combination is quite nonlinear, and the Schottky diode is very expensive. Scott (1974) proposed the use of a device called a "photentiometer" to inexpensively measure the position of a laser beam in a refraction type of slope measurement device. The device operates as an optically activated slide wire resistor, giving perfect linearity.

Mitsuyasu and Honda (1974) took a nonoptical approach to the investigation of the high frequency spectrum of wind waves in a wind-wave tank. They measured wave height with very thin wire, resistance wave

gauges. Both single and double wire types were used with wire diameters of 0.1 mm. The frequency response was found to be reasonably flat to 80 Hz through a dynamic calibration scheme that oscillated the gauge in a tank of water. Electronic differentiation of the wave height signal was used to derive the time derivative of wave height to emphasize the high frequencies. At frequencies beyond 40 Hz this technique could not be used because the results, when converted to height spectra, did not agree with the spectra of the direct height measurement. At a fetch of 8.25 meters they found the wave height energy to increase with wind speed over the mean speed range of 0 to 15 m/s. No approach to an equilibrium range for the energy level was identifiable as wind speed increased to the maximum, even though breaking was clearly visible beyond a mean wind of 10.0 m/s. It is possible that the somewhat low stability of the spectral estimate, there being only 10 FFT calculations averaged, obscured a trend toward saturation.

Ruskevich, Leykin, and Rozenberg (1973) described a measurement system that can measure both time and spatial series of wave height in a wind-wave tank. The device uses an array in either one horizontal dimension or two of resistance wave gauges. The wires are 0.2 mm in diameter. The signal from each wire passes through a correcting amplifier with a gain function designed to compensate for the drop off in frequency response of the wave gauge wires at high frequencies. The device is designed to operate on waves in the range of 3 to 40 Hz. A discretized spatial series is produced by sampling the output of each wire in turn with an electronic switch at a rate of 10 kHz. The output of the switch then represents an almost synoptic look at the wave height at each gauge. At any time the spatial series can then be constructed. Sinitsyn, Leykin and Rozenberg (1973) used this device to investigate

the effect a long wave has on a short wave field that it is passing through. The experiment was performed for both mechanically and wind generated ripples. The frequency and wave number assigned to the ripples were those of the peak of the ripple frequency and wave number spectra, respectively. On this basis long wave crest to trough short wave frequency shifts were measured and found to agree with the expression

$$\omega(\underline{k}, \underline{x}, t) = \omega_0(\underline{k}, \underline{x}, t) + \underline{k} \cdot \underline{U}(\underline{x}, t) \quad , \quad (2-73)$$

where  $\omega_0$  is the free wave frequency, modified to account for the change in body force due to vertical acceleration over the long wave.  $\underline{k}$  is the short wave wavenumber, and  $\underline{U}$  is the long wave horizontal particle velocity. The mechanically generated ripples followed the linear expression, (2-73), somewhat more closely than the wind ripple. Frequency maxima occurred at long wave crests, while wavenumber changes along the long wave profile were insignificant.

## CHAPTER III

### MEASUREMENT OF WAVE SLOPE

#### III.A. Measurement of Slope Versus Height

Munk (1955) pointed out that, because the wave slope statistics emphasize the higher frequency components of the wave system, the study of high frequency waves would be facilitated by the measurement of slope rather than amplitude. For a fixed point, one dimensional measurement of the sort used in the present study, the high frequency emphasis can be demonstrated in the following way.

The aperiodic height and slope descriptions of the surface motion can be expressed as (Kinsman, 1965)

$$\eta(x,t) = \iint_{-\infty}^{\infty} A(k,\sigma) e^{-i(kx - \sigma t)} dk d\sigma \quad , \quad (3-1)$$

and

$$\eta_x(x,t) = -i \iint_{-\infty}^{\infty} kA(k,\sigma) e^{-i(kx - \sigma t)} dk d\sigma \quad , \quad (3-2)$$

where  $A(k,\sigma)$  is the spectral representation of the water surface, and is assumed to be a stationary and homogeneous function.  $k$  is the scalar wavenumber in the direction of the  $x$ -axis. At the fixed position,  $x_1$ , which may be selected as zero for simplicity, we may write

$$\eta(x_1,t) = \iint_{-\infty}^{\infty} A(k,\sigma) e^{i\sigma t} dk d\sigma \quad , \quad (3-3)$$

and

$$\eta_x(x_1, t) = -i \iint_{-\infty}^{\infty} kA(k, \sigma) e^{i\sigma t} dk d\sigma \quad . \quad (3-4)$$

The temporal correlation functions for the wave height and slope time series may then be constructed by application of the expressions (3-3) and (3-4). The correlation functions are defined as (Lee, 1960)

$$\phi_{\eta\eta}(\tau) = \int_{-\infty}^{\infty} \eta(t) \eta(t + \tau) dt \quad , \quad (3-5)$$

and

$$\phi_{\eta_x \eta_x}(\tau) = \int_{-\infty}^{\infty} \eta_x(t) \eta_x(t + \tau) dt \quad . \quad (3-6)$$

Introduction of the transforms of the time series from equations (3-3) and (3-4) yields

$$\begin{aligned} \phi_{\eta\eta}(\tau) &= \int_{-\infty}^{\infty} \left[ \iint_{-\infty}^{\infty} A(k, \sigma) e^{i\sigma t} dk d\sigma \right] \\ &\cdot \left[ \iint_{-\infty}^{\infty} A(k, \sigma) e^{i\sigma(t + \tau)} dk d\sigma dt \right] \quad , \quad (3-7) \end{aligned}$$

and

$$\begin{aligned} \phi_{\eta_x \eta_x}(\tau) &= \int_{-\infty}^{\infty} \left[ -i \iint_{-\infty}^{\infty} kA(k, \sigma) e^{i\sigma t} dk d\sigma \right] \\ &\cdot \left[ -i \iint_{-\infty}^{\infty} kA(k, \sigma) e^{i\sigma(t + \tau)} dk d\sigma \right] dt \quad . \quad (3-8) \end{aligned}$$

Since the surface being described in equations (3-3) and (3-4) is real, one can substitute the complex conjugates,  $\eta^*(t)$  and  $\eta_x^*(t)$ , for the wave

height and slope, respectively, at time,  $t$ , with no change in physical meaning (Kinsman, 1965). The result of the substitution for one group of terms in each of equations (3-7) and (3-8) is

$$\phi_{\eta\eta}(\tau) = \left\{ \left[ \iint_{-\infty}^{\infty} [A(k, \sigma) A^*(k, \sigma) e^{i\sigma\tau}] \right] \int_{-\infty}^{\infty} e^{i(\sigma - \sigma')t} dt \right\} dk d\sigma \quad , \quad (3-9)$$

and

$$\phi_{\eta_x \eta_x}(\tau) = \left\{ \iint_{-\infty}^{\infty} [kA(k, \sigma)] [kA(k, \sigma)]^* e^{i\sigma\tau} \cdot \int_{-\infty}^{\infty} e^{i(\sigma - \sigma')t} dt \right\} dk d\sigma \quad , \quad (3-10)$$

where the terms are regrouped to allow the time integral to stand alone. The time integral of equations (3-9) and (3-10) can be represented by a unit impulse function (Lee, 1960) where

$$\delta(\sigma - \sigma') \equiv \frac{1}{2\pi} \int_{-\infty}^{\infty} e^{i(\sigma - \sigma')t} dt \quad . \quad (3-11)$$

Then for equations (3-9) and (3-10) we may write

$$\phi_{\eta\eta}(\tau) = 2\pi \iint_{-\infty}^{\infty} A(k, \sigma) A^*(k, \sigma) e^{i\sigma\tau} dk d\sigma \quad , \quad (3-12)$$

and

$$\phi_{\eta_x \eta_x}(\tau) = 2\pi \iint_{-\infty}^{\infty} [kA(k, \sigma)] [kA(k, \sigma)]^* e^{i\sigma\tau} dk d\sigma \quad . \quad (3-13)$$

The wave field being considered is two dimensional so there is only one wavenumber associated with each wave frequency, and it is given by the dispersion relation as  $f(\sigma)$ . Equations (3-12) and (3-13) are written as

$$\phi_{\eta\eta}(\tau) = 2\pi \iint_{-\infty}^{\infty} |A(\sigma)|^2 \delta[k - f(\sigma)] dk e^{i\sigma\tau} d\sigma, \quad (3-14)$$

$$\phi_{\eta_x \eta_x}(\tau) = 2\pi \iint_{-\infty}^{\infty} |kA(\sigma)|^2 \delta[k - f(\sigma)] dk e^{i\sigma\tau} d\sigma, \quad (3-15)$$

where the wavenumber dependence of  $A(k, \sigma)$  is expressed by  $A(\sigma)$  and the delta function representing the physically correct result of the dispersion relation. It is then appropriate to write

$$\phi_{\eta\eta}(\tau) = 2\pi \int_{-\infty}^{\infty} |A(\sigma)|^2 e^{i\sigma\tau} d\sigma, \quad (3-16)$$

and

$$\phi_{\eta_x \eta_x}(\tau) = 2\pi \int_{-\infty}^{\infty} |kA(\sigma)|^2 e^{i\sigma\tau} d\sigma, \quad (3-17)$$

where  $k$  is restricted to those values given by the wave dispersion relation.

By definition the spectral density functions,  $\phi_{\eta\eta}(\sigma)$  and  $\phi_{\eta_x \eta_x}(\sigma)$ , are the coefficients of the exponential term in the integrands of equations (3-16) and (3-17), respectively (Lee, 1960). It is then clear that

$$\phi_{\eta_x \eta_x}(\sigma) = k^2 \phi_{\eta\eta}(\sigma).$$

Wave slope intensity is, therefore, emphasized toward the higher frequency range by the value of the wavenumber squared.

The measurement of the slopes of high frequency waves, rather than the corresponding heights, has another advantage. Up to the present time devices used to measure short wave height have all required physical contact with the flow. Obviously the smaller the waves being

measured, the more significant the distortion of the flow created by the insertion of an obstruction. Slope measurements can be made without resorting to physical contact with the surface, leaving the flow undisturbed. So slope measurement seems to be the more attractive technique for measurement of small waves.

### III.B. The Wind-Wave Facility

The measurements required for the present study were conducted in the wind-wave facility at the University of Florida. Figure 1 illustrates the general size and shape of the wind-wave tank. Waves may be generated in the model with a hydraulically powered, mechanical wave generator and through the action of the air flow created by a large blower.

Shemdin (1969) described the wind-wave tank in detail, but the major features will be mentioned here. The tank is a 36.6 meter long channel, divided along its length into two equal bays of 0.86 meter width and 1.9 meter height. At the upwind end of the tank a wind duct system, shown in Figure 2, conveys the air flow produced by the blower into one of the wave tank channels. The air inlet modifies the flow to simulate rough turbulent air flow in the wind channel. Below the ductwork the hydraulically operated wave generator paddle produces large scale waves as specified by a signal generator. The waves propagate through the 36.6 meter long test section. A 5.8 meter long wave absorber, composed of baskets filled with stainless steel turnings, is placed at the downwind end of the tank.

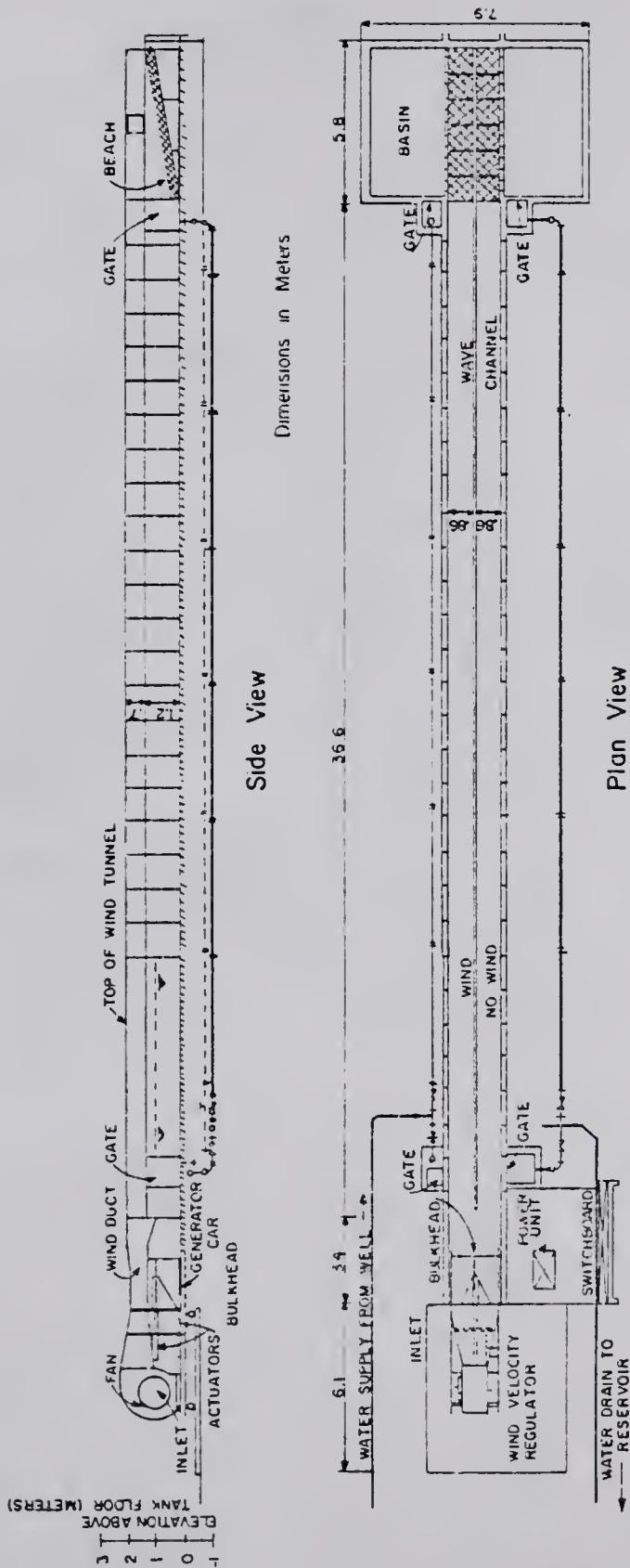


Figure 1. Plan and side views of the wind-wave tank model.

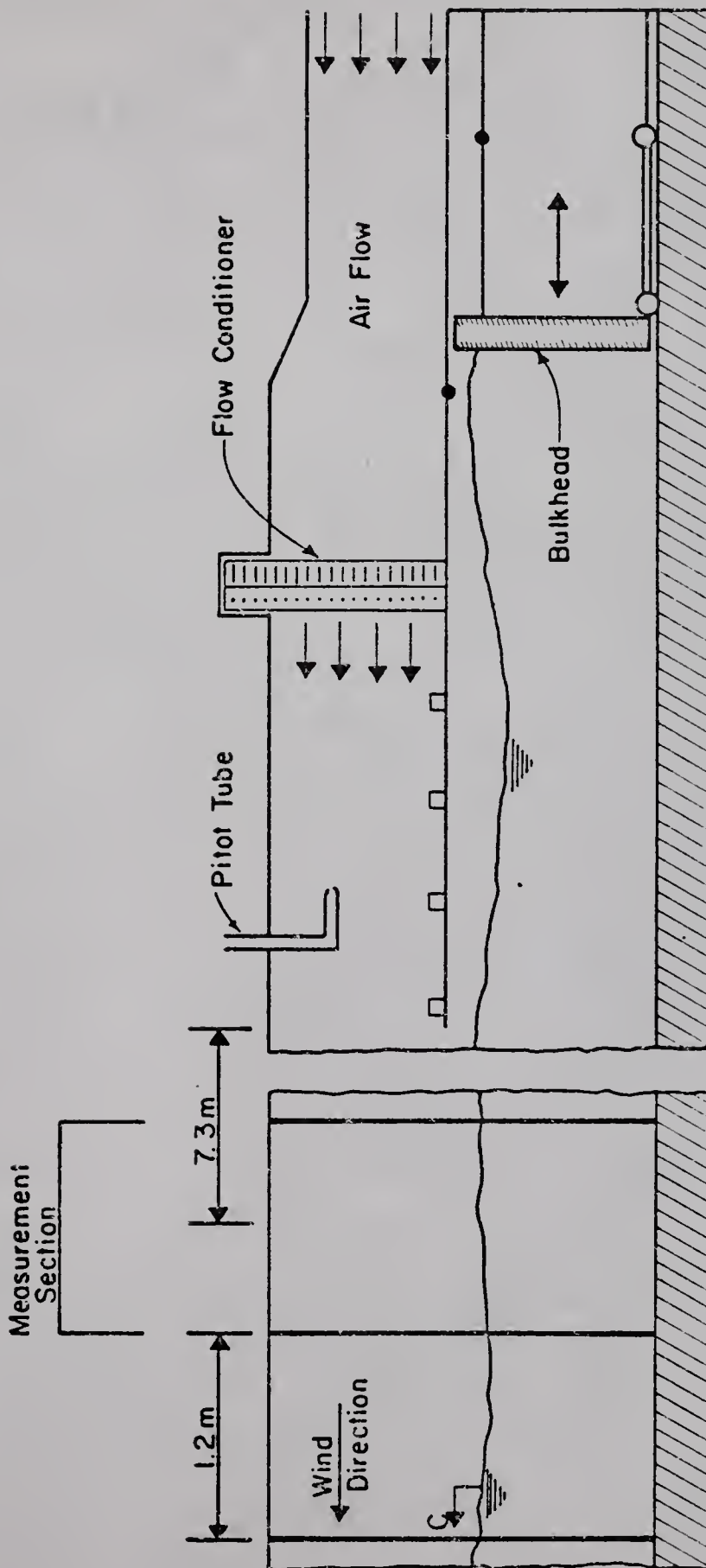


Figure 2. Wave generator section and test section of the wind-wave model.

### III.C. Laser-Optical System for Measuring Slope

The objectives of this experiment required the accurate detection of high frequency wave slopes. A device was designed and built at the University of Florida (Palm, 1975) to accomplish this task. The instrument is a laser-optical system which operates on the principle of optical refraction at the air-water interface. It is capable of obtaining analog time series records of wave slope along two principle axes in the interfacial plane. It features an insensitivity to the local wave height and to light source intensity variations.

The quantities required to discuss the principle of operation of the instrument for one axis of measurement are shown in Figure 3. For simplicity consider a system of plane waves to be passing through the fixed point of measurement. The laser beam pathway is stationary and aligned with the vertical while in the water layer, before incidence on the air-water interface. The angle formed between the submerged laser pathway and the surface normal, the angle of incidence, is designated as  $\theta_i(t)$ . The light beam is refracted at the interface and proceeds along a pathway in the air forming an angle,  $\theta_r(t)$ , the angle of refraction, with the local surface normal. The relationship between the instantaneous angles of incidence and refraction is known as Snell's Law and is specified by

$$n_i \sin \theta_i(t) = n_r \sin \theta_r(t) \quad ,$$

where  $n_i$  is the index of refraction of the water, which contains the incident beam, and  $n_r$  is the index of refraction of the air, which contains the refracted beam. By virtue of the geometry shown in Figure 3, it is possible to define a deflection angle,  $\phi(t)$ , in terms of the angles of incidence and refraction that specifies the deflection of the

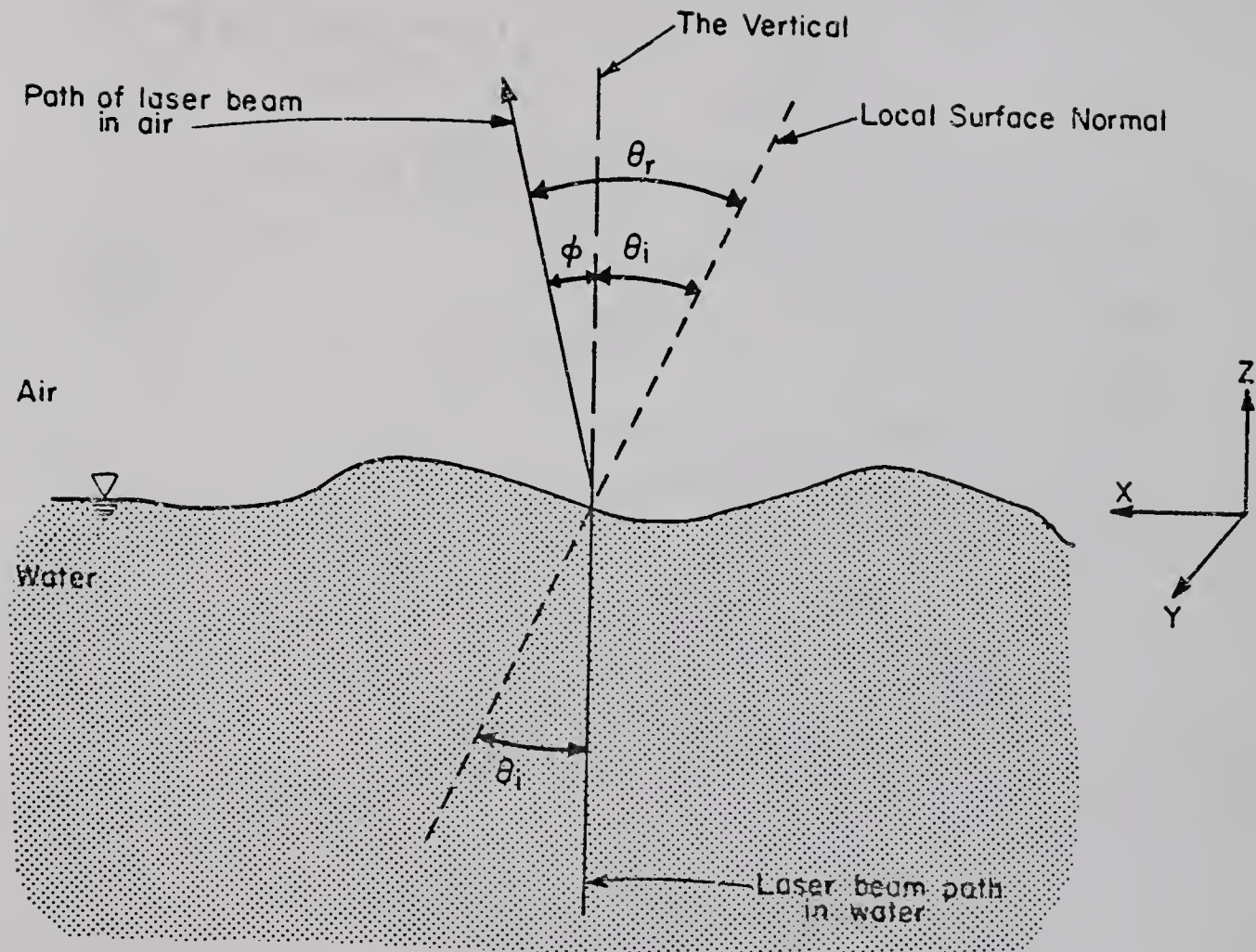


Figure 3. Orientation diagram for laser beam refraction at the air water interface.

refracted beam away from the true vertical axis as

$$\phi(t) = \theta_r(t) - \theta_i(t) \quad . \quad (3-18)$$

Using Snell's Law in equation (3-18), one can express the deflection angle in terms of the angle of incidence

$$\phi(t) = \sin^{-1} [n \sin \theta_i(t)] - \theta_i(t) \quad , \quad (3-19)$$

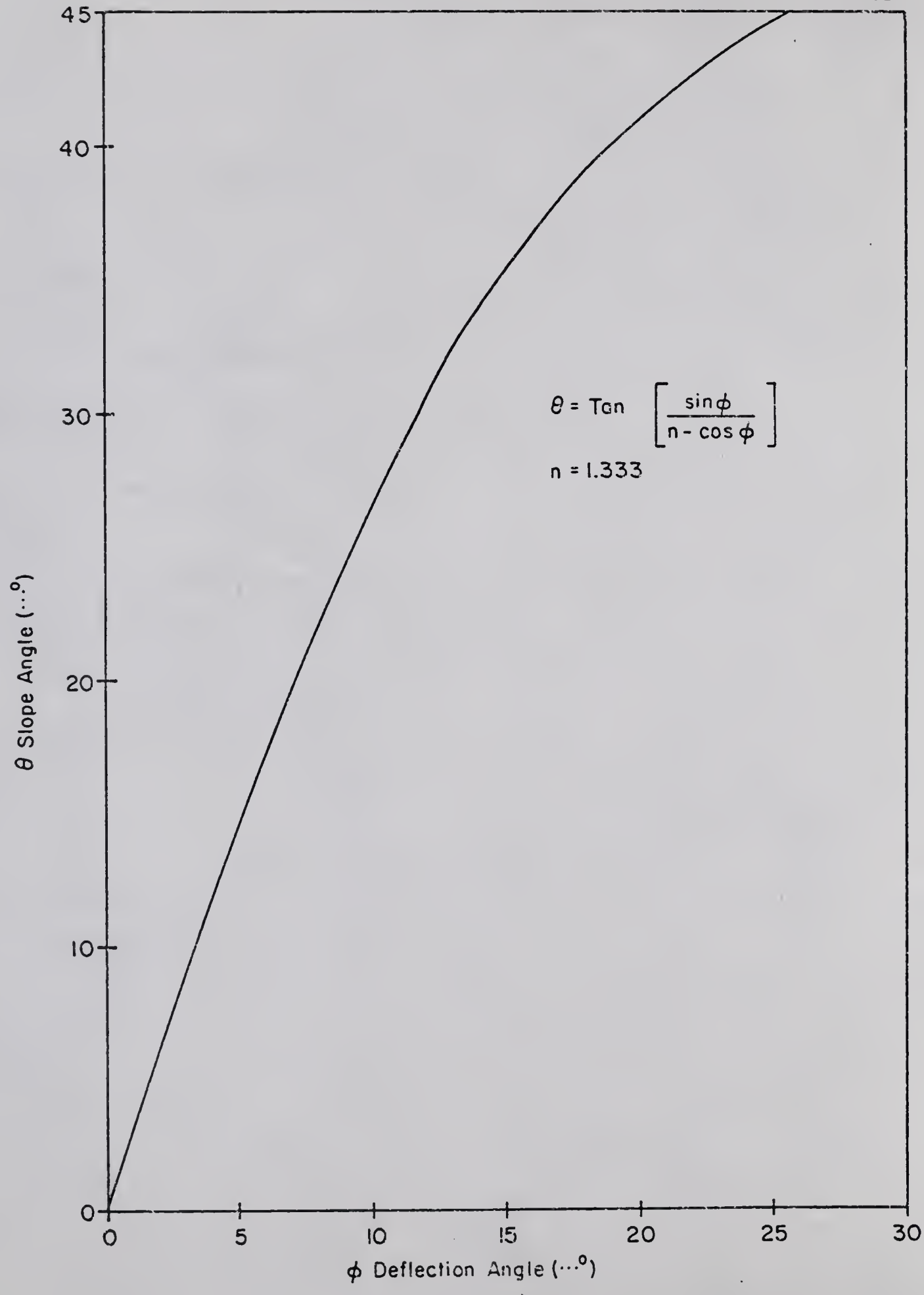
where  $n = n_i/n_r$  is the relative index of reflection, and it is ascribed a constant value of 1.333. Since the laser beam is aligned with the vertical axis, the angle,  $\theta_i(t)$ , defines the time history of the local wave slope in the x direction as shown in Figure 3. Solving equation (3-19) for  $\theta_i(t)$  shows that measurement of the deflection angle yields information about the local slope. The expression becomes

$$\theta(t) = \theta_i(t) = \tan^{-1} \left[ \frac{\sin \phi(t)}{n - \cos \phi(t)} \right] \quad , \quad (3-20)$$

where  $\theta(t)$  is understood to be the local value of slope. This relation is plotted in Figure 4. The instrument receiver measures the deflection angle through the means of electronic detection of the corresponding deflection distance in a horizontal plane on which the beam is made to impinge. The resultant electrical signal is related directly to deflection angle through calibration, and then to wave slope through relation (3-20).

Figure 5 schematically depicts the optical receiver. It consists of an aluminum housing containing four essential components; the objective lens, the diffusing screen, the imaging lens, and the photodiode detector. The refracted laser beam enters the receiver through the objective lens at the lower end of the receiver. The lens is an Aero-Ektar,  $f/2.5$ , 30.48 cm focal length lens. After passing through the objective lens the laser beam is incident on the diffusing screen of

Figure 4. The conversion of deflection angle to wave slope.



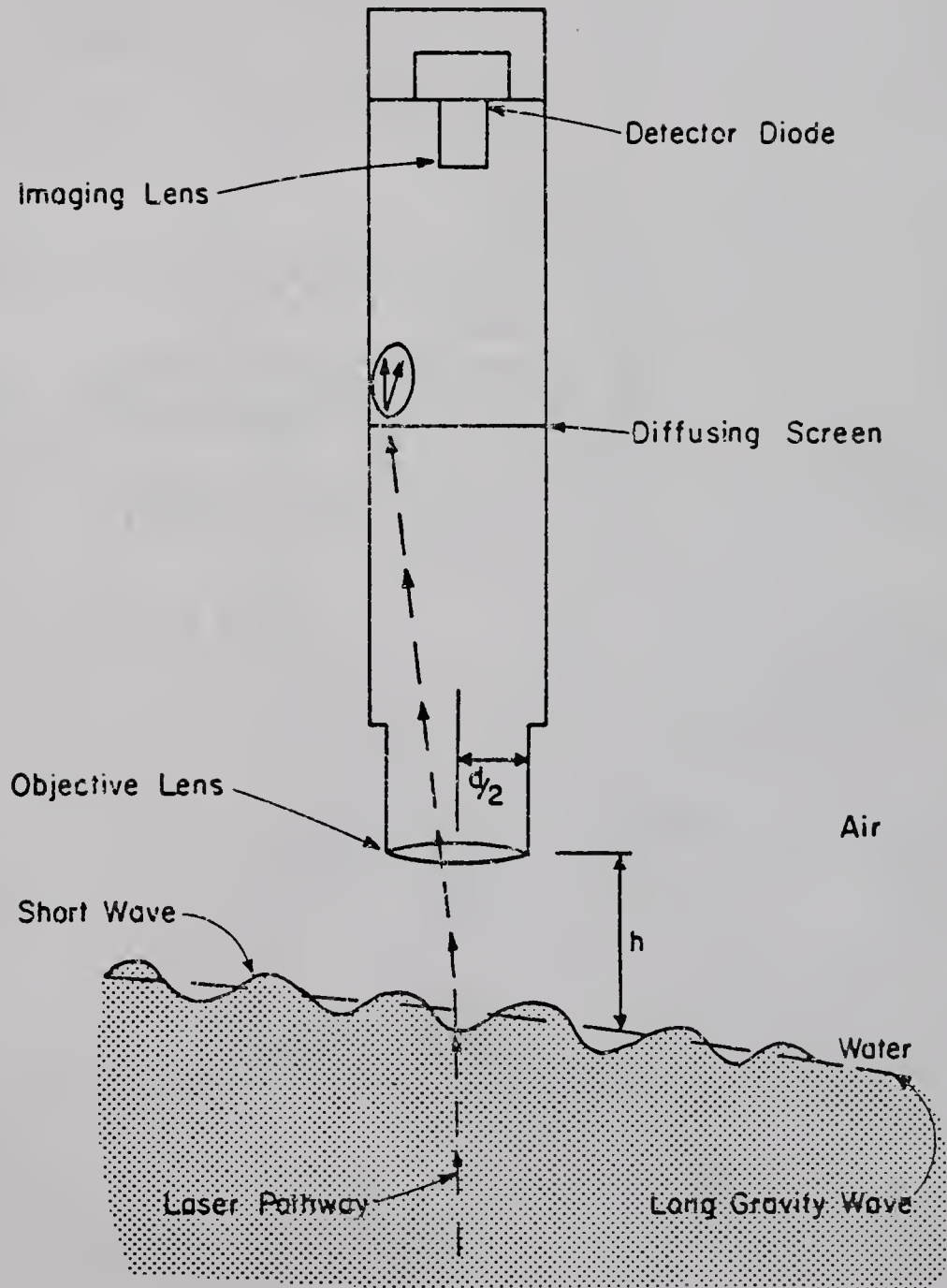


Figure 5. Schematic view of the receiver of the optical wave slope measurement system.

frosted acrylic, placed in the lens rear focal plane. The objective lens is set to focus at infinity, so that a ray of light entering the lens at an angle,  $\phi$ , away from the instrument axis is focused at a fixed distance from the axis on the diffusing screen, regardless of its point of entry through the lens. Hence, at the screen the problem has been converted from one of angle measurement to one of displacement measurement. The fact that the displacement in the plane of the screen is uniquely related to the deflection angle means that the beam can originate at any distance from the lens and still have the same effect. So the changing wave height will not affect the slope measurement. The imaging lens is necessary to reduce the size of the diffusing screen to that of the photodiode area. The lens is a 35 mm camera lens, the input to which is bandpass filtered at 6328 Angstroms with 100 Å half power width. The lens is an f/1.4, 55 mm focal length, Super Takumar. The image of the laser spot on the diffusing screen is thereby focused on the surface of the detector, which is a United Detector Technology model SC/50 Schottky barrier two dimensional photodiode with a 3.56 cm square active area.

The maximum deflection angle that is detectable is a function of the objective lens aperture and distance from the water surface. This relation is

$$\phi_{\max} = \tan^{-1} \left[ \frac{1}{2} \frac{d}{h} \right], \quad (3-21)$$

where  $d$  is lens diameter and  $h$  is distance between the lens and the water surface. Figure 6 shows the maximum measurable values of deflection and slope angle for a given instrument height above the water surface.

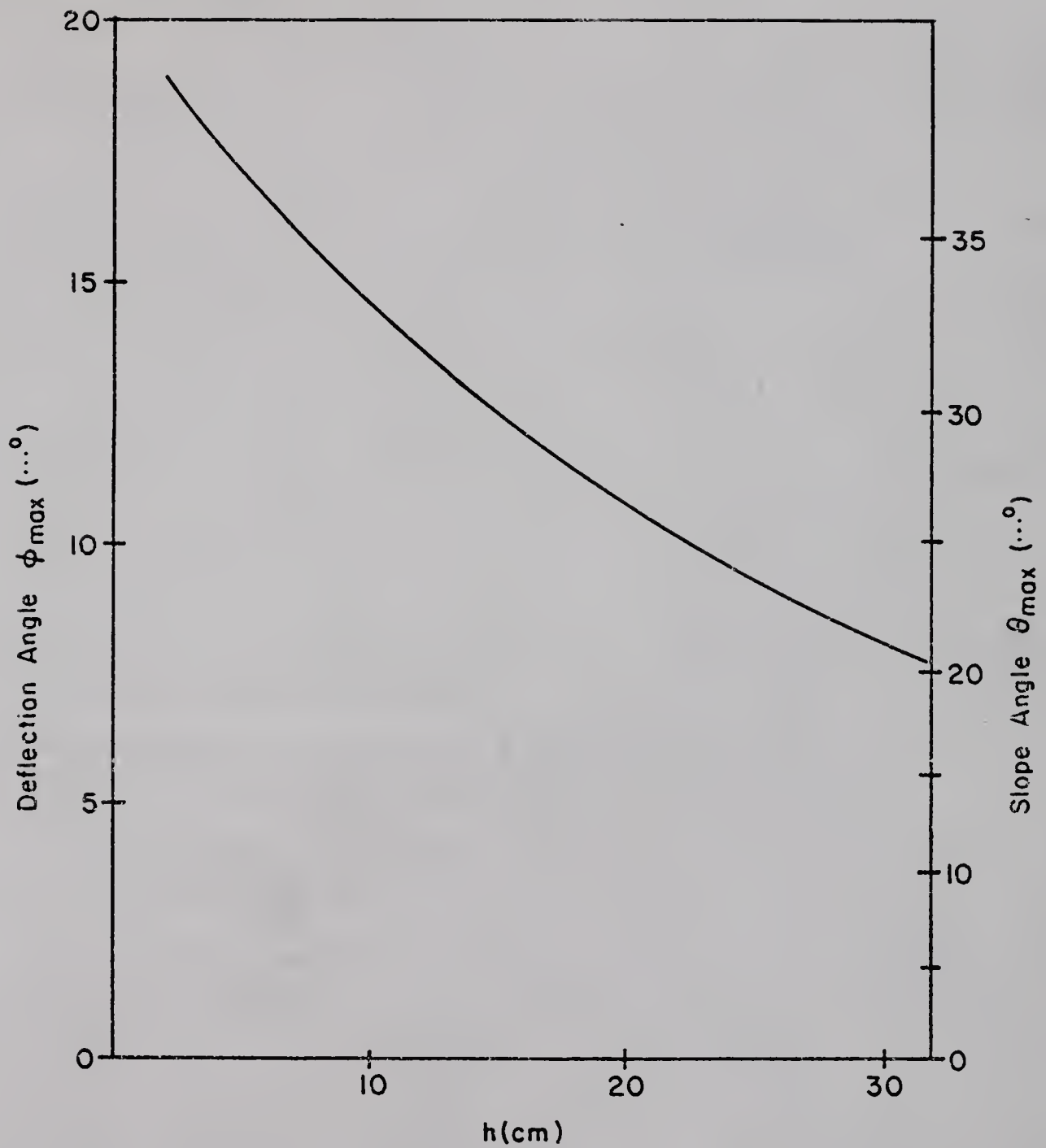


Figure 6. Maximum deflection and slope angles measurable as a function of distance from the objective lens to the local water level (Palm, 1975).

In reality, of course, the water surface is two dimensional and the laser beam is deflected along the two orthogonal dimensions of any horizontal plane it is incident on. In this situation the location of the laser beam in the incident horizontal plane is described by the deflection angle,  $\phi(t)$ , and the azimuthal angle,  $\theta_a(t)$ . The electrical outputs from the diode are combined as shown in Figure 7 to yield electrical signals relating to slope along two orthogonal directions, x and y, that correspond to the physical deflections of the laser beam along the same axes. The result is the analog measurement of wave slope in two dimensions at an interfacial point. The normalization operation performed by the analog divider shown in Figure 7 is very useful, because it eliminates the effect of a variation in laser beam intensity on the slope output.

The errors in the measurement result from several sources. These are calibration and alignment, laser beam size and nonuniformity, optical aberrations, and amplifier drift. Searching the system behavior for local anomalies indicated that optical aberrations were negligibly small.

When calibrations were performed on an optical bench in an optics laboratory at a constant temperature, it was possible to duplicate them to within 2 to 3%. However, when installed in the wind-wave tank, changing instrument temperature produced sizeable amplifier drift. It was found that the output drift could be reduced by performing the signal division pictured in the output circuitry of Figure 7 in the computer analysis rather than in the analog circuit of the instrument. To further reduce temperature drift, it was possible to adjust the amplifier offset voltage without changing the calibration. The maximum

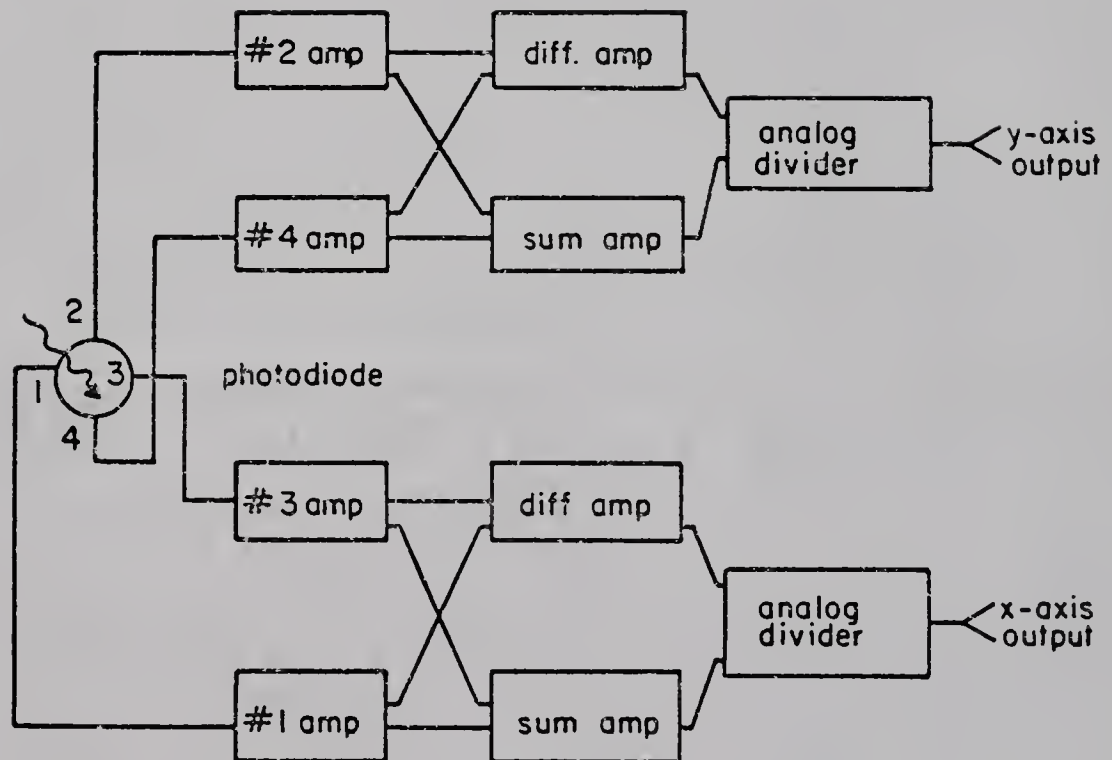


Figure 7. Analog conversion of the photodiode output signals to orthogonal axes of deflection (Palm, 1975).

uncertainty in the calibration after moving the instrument to the field was +7%.

Laser beam size and nonuniformity restrict the size of the smallest resolvable water wave lengths. Cox (1958) performed an analysis of his measurement, assuming a uniform light intensity across the beam diameter,  $2r_0$ . He concluded that waves of measurable length,  $\lambda$ , satisfy the relation,  $\lambda \geq 6.8r_0$ . Palm (1975) performed a more complex analysis for the present instrument, assuming the laser beam to have a Gaussian distribution of light intensity across its diameter. In this case the distance,  $r_0$ , is the radius at which the intensity reaches  $1/e^2$  of its maximum value. The calculated error in the slope measurement resulting from the finite size and Gaussian intensity distribution of the laser beam is shown in Figure 8, as a function of the actual maximum slope and beam radius normalized by water wavelength. The beam radius to the  $1/e^2$  points is 0.4 mm. Therefore, if a wave of the highest measurable peak slope of  $35^\circ$  is passing through the laser spot, Figure 8 would predict a 10% measurement error if the length of the wave is 2.4 mm. Figure 8 shows that this error decreases as  $\lambda$  increases, increases rapidly as  $\lambda$  decreases, and decreases if the slope of a wave with a given  $r_0/\lambda$  ratio is decreased.

The frequency response of the electronics was estimated by chopping the laser beam input to the receiver. The response was found to be flat to above 400 Hz.

The calibration of the instrument was carried out in an optics laboratory. The laser source and instrument housing were lined up at right angles to each other, such that their axes lay in the same horizontal plane. Light from the laser was reflected by a rotatable prism into the receiver. Rotation of the prism caused the laser beam to sweep

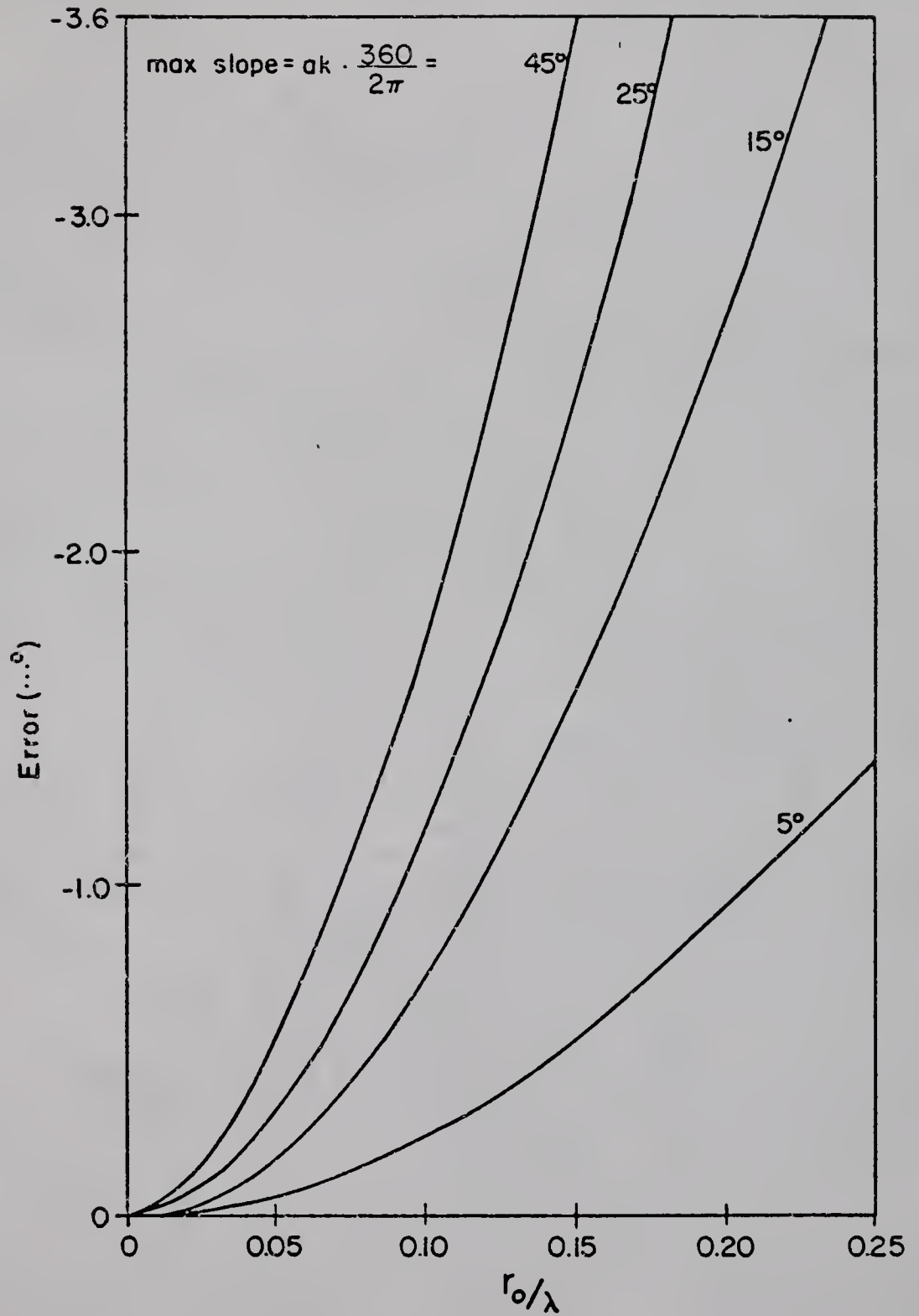


Figure 8. Error introduced into the slope measurement due to the finite size of the laser beam (Palm, 1975).

across the objective lens along the horizontal axis. The device output was recorded in deflection angle increments of  $2^{\circ}$ . To ascertain the response of the device over its entire active area the instrument housing was rotated and the deflection angle sweep was performed along the new azimuth. The result is a calibration net, as shown in Figure 9 (Palm, 1975).

In this study the x-axis of the receiver is aligned with the longitudinal axis of the wave tank. To measure the x-component of surface slope only a one dimensional calibration, in this case the x-axis calibration, is required. Combining the instrument calibration of deflection angle versus voltage output with the conversion to slope angle of equation (3-20) gives the calibration result of Figure 10. It was found that the slope could be calculated with more precision and less concern about thermal drift if the analog divider was bypassed and the computation performed by the computer. Figure 10 applies to the situation when computer computation of the quotient was done.

The measurement system is installed roughly at the center of the wind-wave channel at a fetch of 7.3 m. Figure 11 schematically illustrates the orientation of the measurement system components in the cross section of the wave tank. The laser is a Coherent Radiation Model 80-2S, 2 mw, 12 volt unit. It is submerged and held in place by a pipe mounting so that its highest point above the bottom is 25 cm below the still water level. The beam is aligned with the vertical by adjusting the clamping bolts that penetrate the wall of the pipe. The receiver is supported by a gimbal mount, rigidly suspended from the top of the tank, such that the x measurement axis coincides with the longitudinal axis of the tank. The center of the objective lens is placed directly over the laser beam with the use of a template and lowered to a

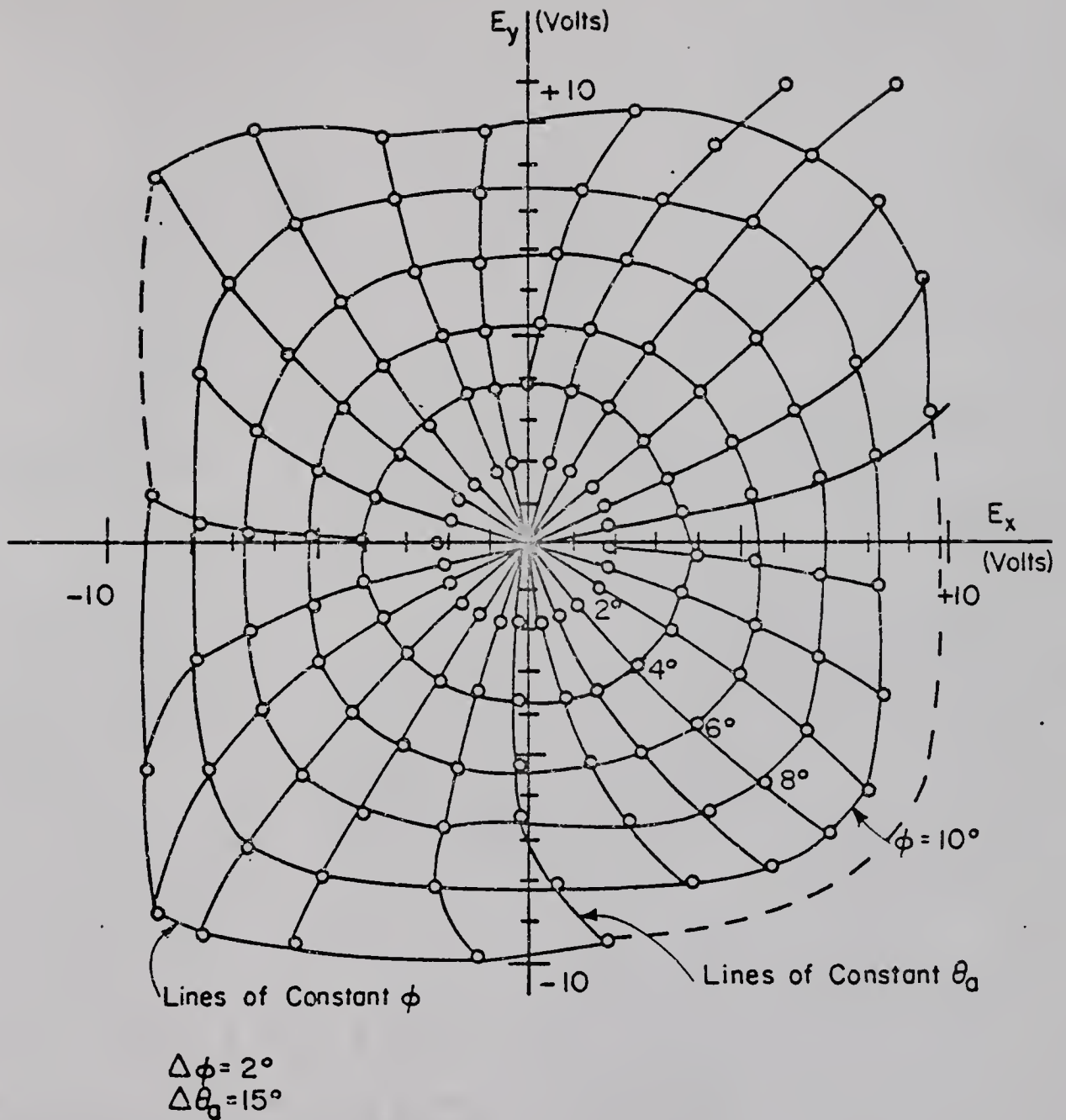


Figure 9. Static response of the instrument receiver to deflection and azimuth changes (Palm, 1975).

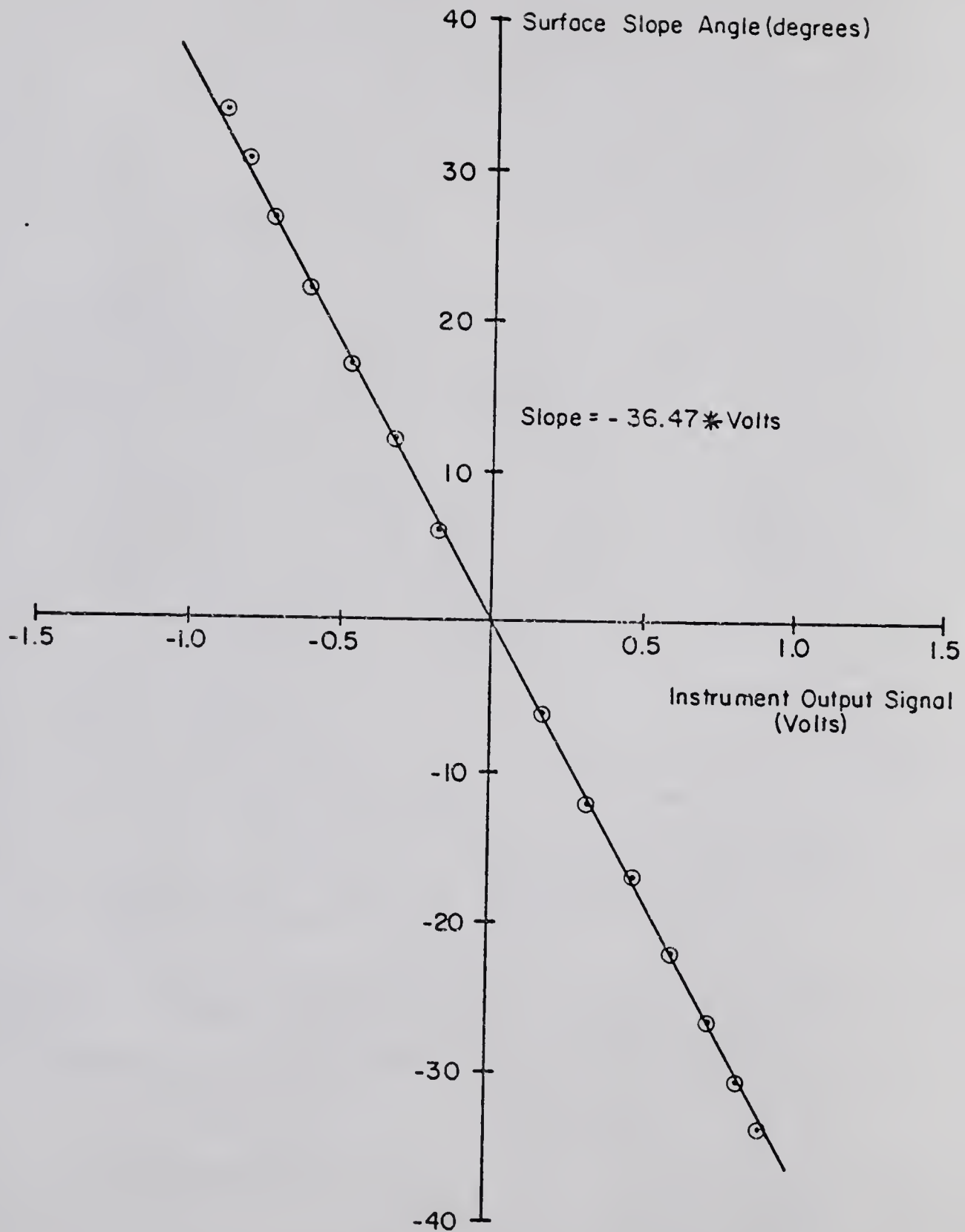


Figure 10. X channel instrument calibration curve.

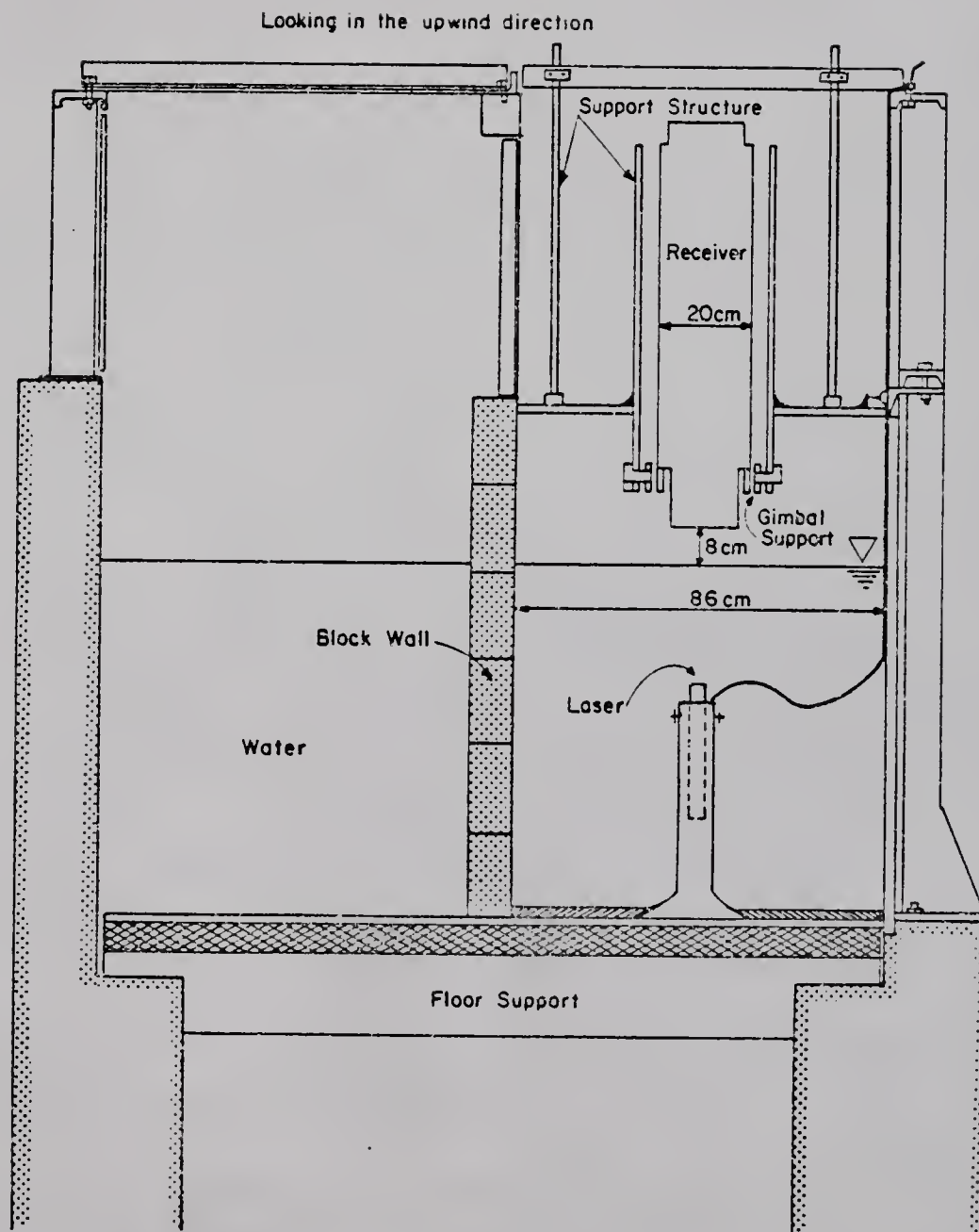


Figure 11. Schematic cross section of the wave tank at the instrument installation site.

height of 8 cm above the still water surface. Alignment with the vertical is achieved by rotating the receiver about the gimbal pivots until the beam passing through the center of the objective lens strikes the center of the photodiode, giving a zero signal on both channel outputs.

Figure 12 shows the slope detector receiver, mounted and emplaced in the wave tank. Figure 13 shows the physical relationship between the submerged laser and the end of the receiver.

The optical receiver was placed close to the water surface to allow high angle measurements. At reference wind speeds exceeding 11.9 m/s wave slopes exceeding the  $35^{\circ}$  measurable maximum at the instrument height of 8 cm were not uncommon. It is reasonable to assume that the instrument produced some alteration of the air flow that was related to the instantaneous height of the water surface directly below it. The short waves remained in the region of most severe air flow modification at the long wave crest (taken as 20 cm in length), due to the reduced distance between receiver and water surface, for 0.1 to 0.2 s. It is felt that changes in the short waves brought about by the altered wind field in this period of time would be small. Visually no effects due to the presence of the receivers could be seen.

Slope measurements were made, prior to the development of the device described here, with a slope detector that had a limited slope range, but was located 35 cm from the still water surface. Slope intensity variations calculated from time series obtained from the 35 cm height had maxima located at the long wave crest and forward face. The similar phase angles obtained from these measurements with two different devices leads to the conclusion that the high slope intensities at the long wave crest are not induced by the modification of the air flow created by the presence of the instrument.

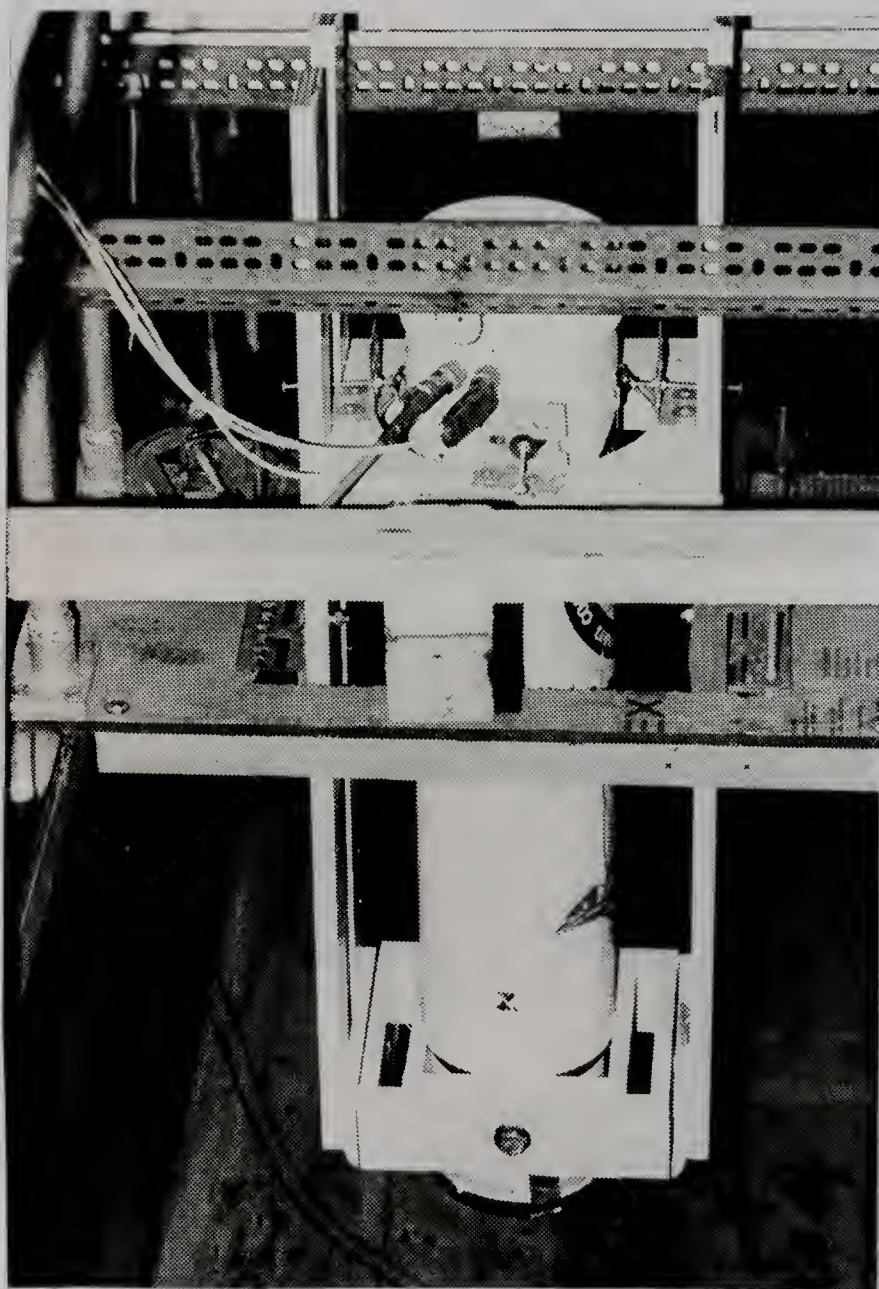


Figure 12. The slope measurement receiver in operating position in the wave tank.

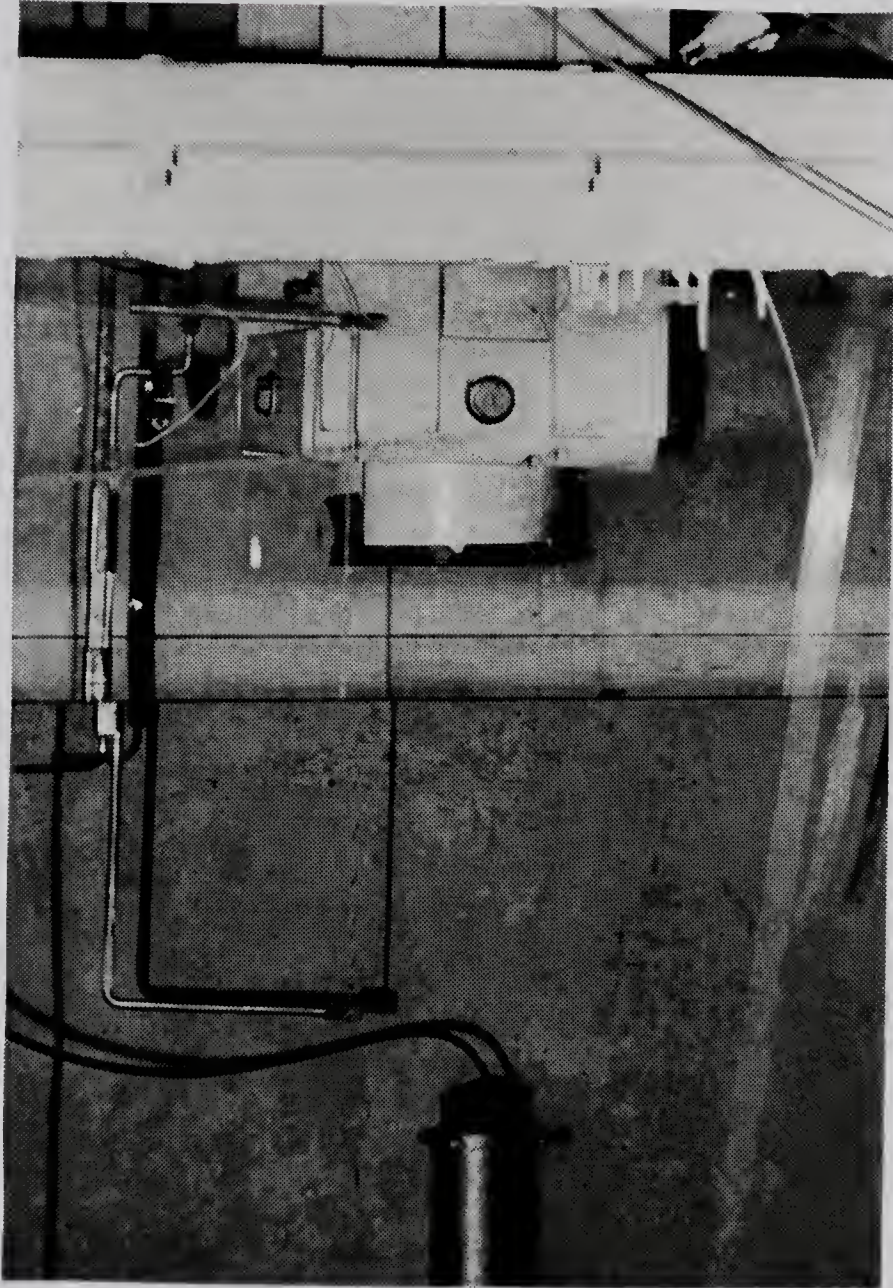


Figure 13. Side view of the installed relationship between the system light source and receiver.

### III.D. Supporting Measurements

The wind speed at the reference location was measured with a Pitot-static probe and a Pace differential pressure transducer. The flow through the fan was set according to the velocity figure obtained at the reference location.

A capacitance wire wave gauge was installed alongside the slope detector, about 20 cm laterally from and 10 cm downwind from the point of laser beam surface penetration. The dynamic response of the wave gauge is such that it is not able to respond to waves of high frequency. Its sole function was to monitor the mechanically generated long wave, so that the phase of the slope measurement relative to the long wave could be determined. The wave gauge static calibration curve obtained during experiment three is shown in Figure 14. The figure shows the calibrations obtained before and after the experiment. The DC shift between the two is a result of electrical drift and water level change. The final calibration was selected for use, although either would have been satisfactory because the DC level is removed in the analysis.

Three local wind velocity profiles were made at reference wind speeds of 4.4, 8.3, and 11.9 m/s. The leading tip of the Pitot-static probe was located 71 cm upstream of the most forward portion of the slope detector receiver, and traversed the wind section from about 1.0 to 54.0 cm above the still water level. A large diameter United Sensors probe was used in conjunction with a type 1014A Datametrics electronic manometer. The measurement transducer was a Barocel unit of 10 mm Hg full scale range. The DC output of the manometer, representing the local dynamic pressure, was electronically time averaged over a 20 s interval to obtain a reliable estimate of its mean value. The wind

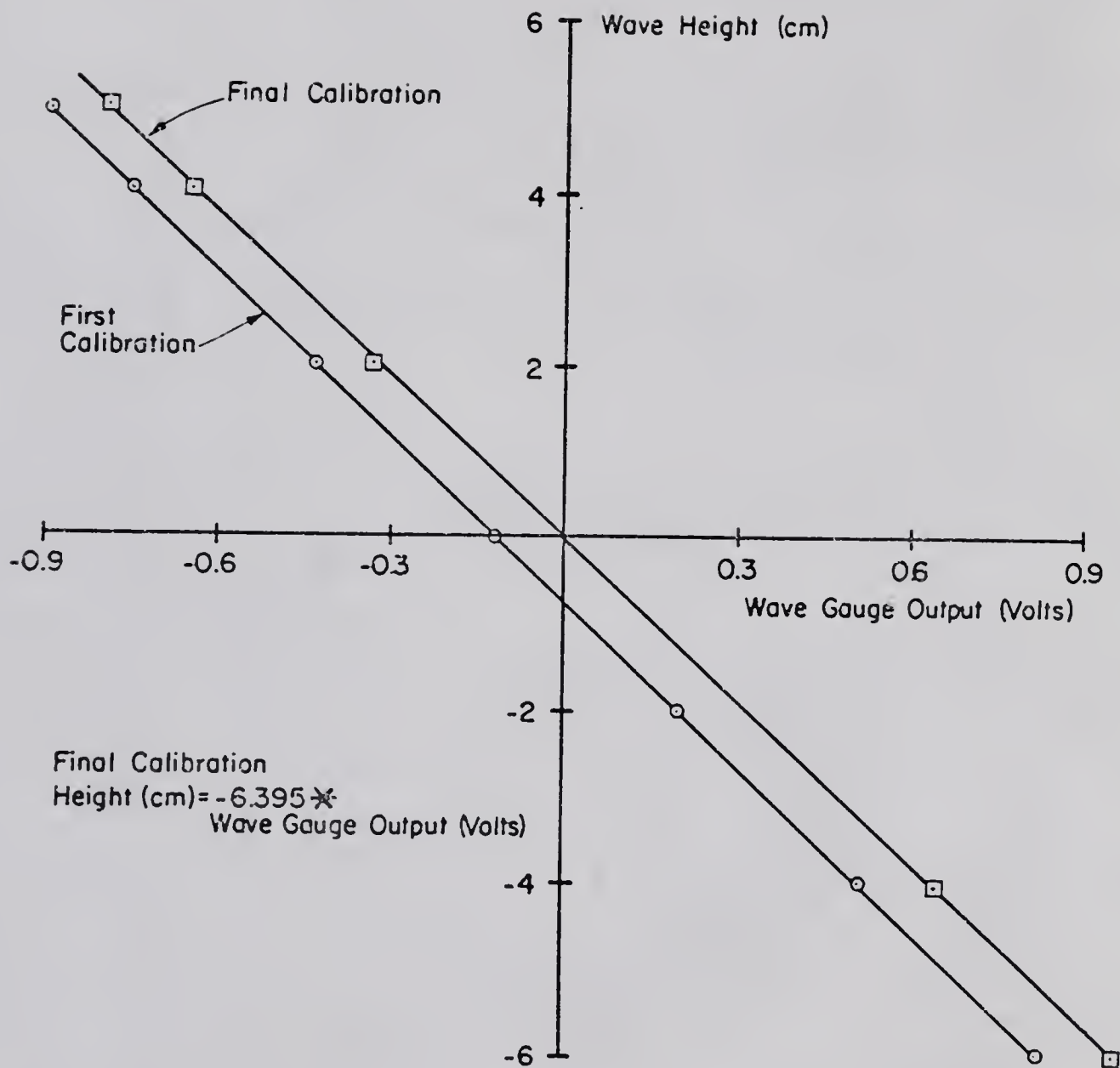


Figure 14. The wave gauge calibration for Experiment 3.

section was completely enclosed from the fan to 1.2 m upstream of the local wind measurement. From that point and on downstream the tank top was left open. Figure 15 shows the three velocity profiles obtained. The friction velocity,  $U_*$ , was calculated in the usual way from the profile data by assuming that they have a logarithmic distribution with height. This assumption seems reasonable based on data in the lower levels shown in Figure 15.

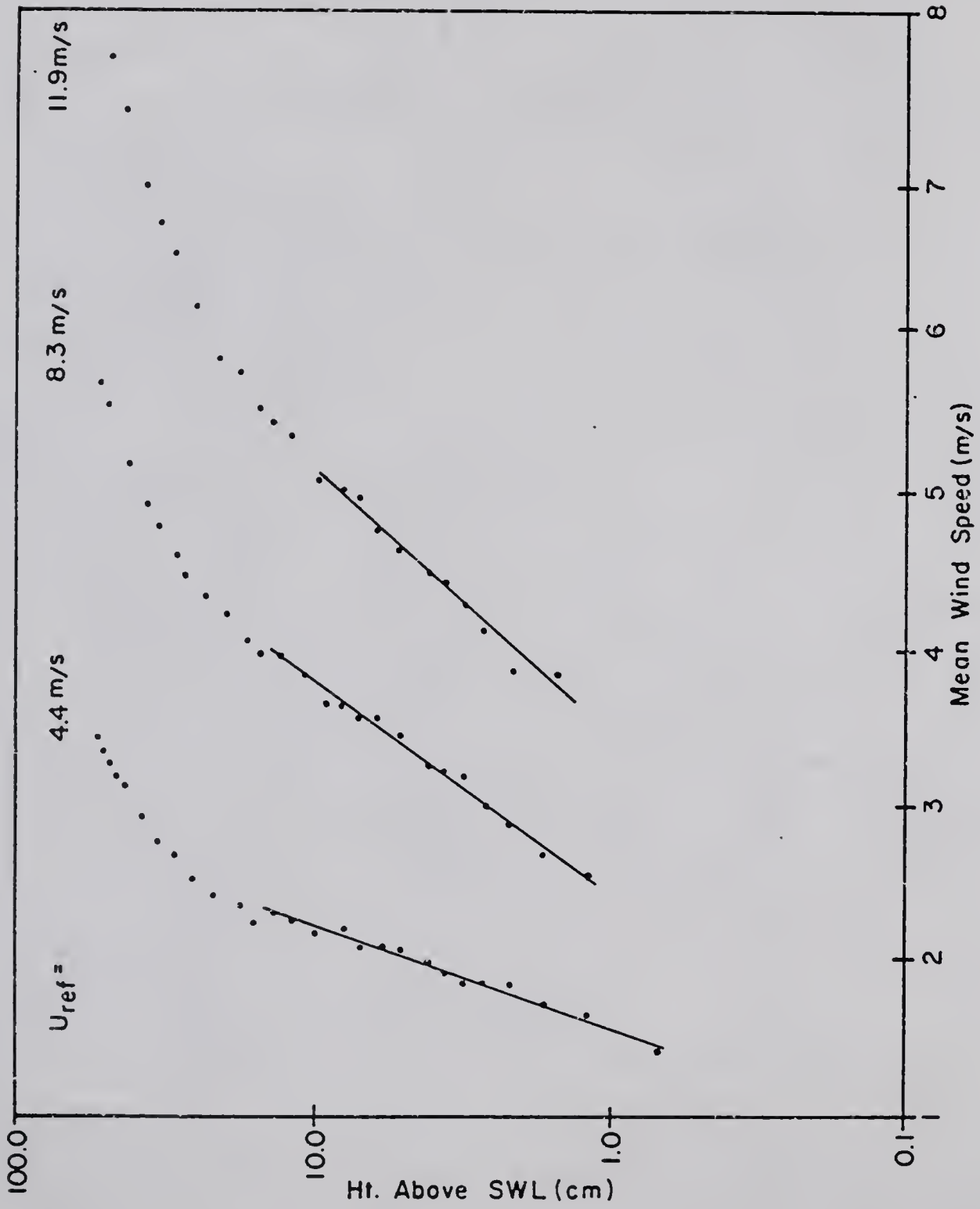


Figure 15. Three local wind velocity profiles. Reference wind speeds: a) 4.4 m/s, b) 8.3 m/s, c) 11.9 m/s.

### III.E. Experimental Conditions

Several experiments utilizing the laser-optical system were conducted in the wind-wave tank. The data to be discussed presently were all obtained in the nine tests of experiment number three (E3). Each test corresponded to a different set of conditions as detailed in Table I, the experimental test conditions. The tests are numbered T13 through T21 and are completely identified as E3T13 through E3T21. The basic long wave parameters of height and period were the same for each test. To aid in comparison with results of other investigations, the wind speeds are reported as reference value, local value at the measurement site, and friction velocity value at the measurement site. For the tests with reference wind speeds other than 4.4, 8.3, and 11.9 m/s the local velocities were not measured, but were projected from those values that were actually measured.

Prior to the start of the experiment, the wave tank walls and bottom were cleaned. For five hours immediately before the experiment the surface layer in the water was skimmed by an overflow weir. These measures were designed to minimize surface contamination. During the experiment, a light, oily film appeared on the water surface. The oil source is unknown, but it must have been either leached from an accumulation on the wave absorbing beach material or washed from the hydraulic piston of the wavemaker. Since the formation of a surface slick was anticipated, surface water was sampled during the experiment and the surface tension measured with a ring tensiometer. Before the experiment began the surface tension value was 68.8 dynes/cm. The water sample obtained during the experiment indicated a surface tension value of 70.6 dynes/cm.

TABLE I  
EXPERIMENTAL TEST CONDITIONS

Experiment and Test Designation	Reference Wind (m/s)	Local Wind at 7.3 m Fetch (m/s)	$U^*$ at 7.3 m Fetch (m/s)	Wave Period (s)	Wave Height (cm)
E3T13	3.8	2.7	0.099	2.0	10.0
E3T14	4.4	3.4	0.110	2.0	10.0
E3T15	4.9	3.5	0.127	2.0	10.0
E3T16	5.6	4.0	0.145	2.0	10.0
E3T17	5.9	4.2	0.153	2.0	10.0
E3T18	7.2	5.1	0.187	2.0	10.0
E3T19	8.3	5.7	0.223	2.0	10.0
E3T20	9.2	6.5	0.239	2.0	10.0
E3T21	10.1	7.2	0.262	2.0	10.0

DATE: Sept. 18, 1975

TIME: 12:00 p.m.

Before testing began the laser-optical system and wave gauge were installed in the wind-wave channel at a fetch of 7.3 m. The laser beam was aligned with the vertical and the optical detector was aligned with the laser beam, allowing the use of the calibration data obtained in the optics laboratory. The wave gauge was calibrated by changing its position along the vertical axis and by physically and electrically measuring the changes.

After alignment, warm up, and calibration the test was begun by setting the long wave parameters. The mechanical, wave generator was set in motion during the no wind condition in the wind-wave tank. The wave form produced by the wave generator was specified at the input of the mechanical-hydraulic system by a function generator. The input function was a sinusoid. Thus, the wave period was set by control of the period of the input sinusoid. The wave amplitude was varied by control of the amplitude of the input sinusoid, and set according to the direct measurement of its height in the wind-wave tank. The long wave profile for all of the tests was a slightly irregular sinusoid of 2.0 s period and 10.0 cm height.

The fan was then turned on to provide a wind field for the development of the wind driven portion of the wave spectrum. The wind condition was started at the lowest value and increased for each succeeding test to the maximum. Each individual test required a minimum of 15 minutes to complete. Five minutes were used for the recording of the data signals. The remainder of the time was allowed to permit the water motion to reach a steady state at each wind speed.

The testing procedure was halted after approximately every hour to check water level, surface condition, and instrument drift. In each

case the laser beam was turned off and the instrument amplifier outputs rezeroed for the no light condition. The DC drifts generally experienced were within 40 mv, representing somewhat less than 5% of the full scale slope.

### III.F. Digital Data Acquisition and Reduction

The data signals were recorded in the FM mode on a Hewlett Packard model 3960A instrumentation tape recorder. According to Hewlett Packard, the tape deck and tape combination had a frequency response of 0 to 312 Hz with a variation of less than  $\pm 1.0$  db within that range. The signal to noise ratio was 45 db and the peak to peak flutter was 0.70% of full scale.

The recorded data signals were sampled at a rate of 400 Hz without prior filtering, and rerecorded in digital format on magnetic tape. The three signals recorded for digital processing were the water surface displacement, and the x-channel sum and difference outputs of the slope detector. The three channels of data were sampled essentially at the same instant to maintain their parallel relationship to one another in time.

The digitized data were used in two different analysis schemes. The first, to be discussed below, yields the experimental short wave modulation figures. The second, to be discussed in Chapter VI, yields the first order spectral parameters required to calculate modulation by way of the Hamiltonian formulation of the problem.

The purpose of this analysis is to produce a stable estimate of short wave slope intensity at selected regions of the long wave profile. In doing this the technique of ensemble averaging is applied to specific subsets of the set of data epics available.

For every test condition data from 133 cycles of the long wave are available for data processing. For each of the long wave cycles the positive going wave height zero crossing is located. Starting at each zero crossing, the slope time series is divided into eight overlapping

segments, as shown in Figure 16. Each segment spans 200 data points and overlaps 100 points of the previous segment. Each segment may be thought of as an individual member of several different ensembles of data epics. For example, two of the ensembles, those of every epic and of every other epic, can be operated on to yield good estimates of the first order spectrum of the short wave slope record. If the ensemble is taken as being composed of all the segments appearing at the same phase location of a long wave profile (for example, all segments numbered one in Figure 16) it can be operated on to yield an estimate of the phase averaged spectrum of the slope record. The phase averaged spectral estimate calculated for each segment is assumed to be representative of the "typical" spectrum associated with a point central to the segment on any given long wave cycle.

The slope intensity spectrum for each data segment results through the application of a Fast Fourier Transform (Robinson, 1967) routine. Before Fourier transformation a cosine bell is applied to the first and last 10% of the data points in each segment and 56 zero value points are added to each segment. The FFT is then performed on the eight segments in the long wave cycle. Without further smoothing the slope intensity spectra are calculated for each of the transformed segments and retained in memory for subsequent averaging with the 132 additional spectra to be calculated that have the same phase relationship to the long wave height signal.

The slope time series measured at the low wind speeds of 3.8 m/s to 5.9 m/s contain a slope component due to the long wave that appears to be significant relative to the wind driven wave slopes. The low frequency component appears as a trend in the segmented data. The low resolution of the spectral calculation and the large amount of energy

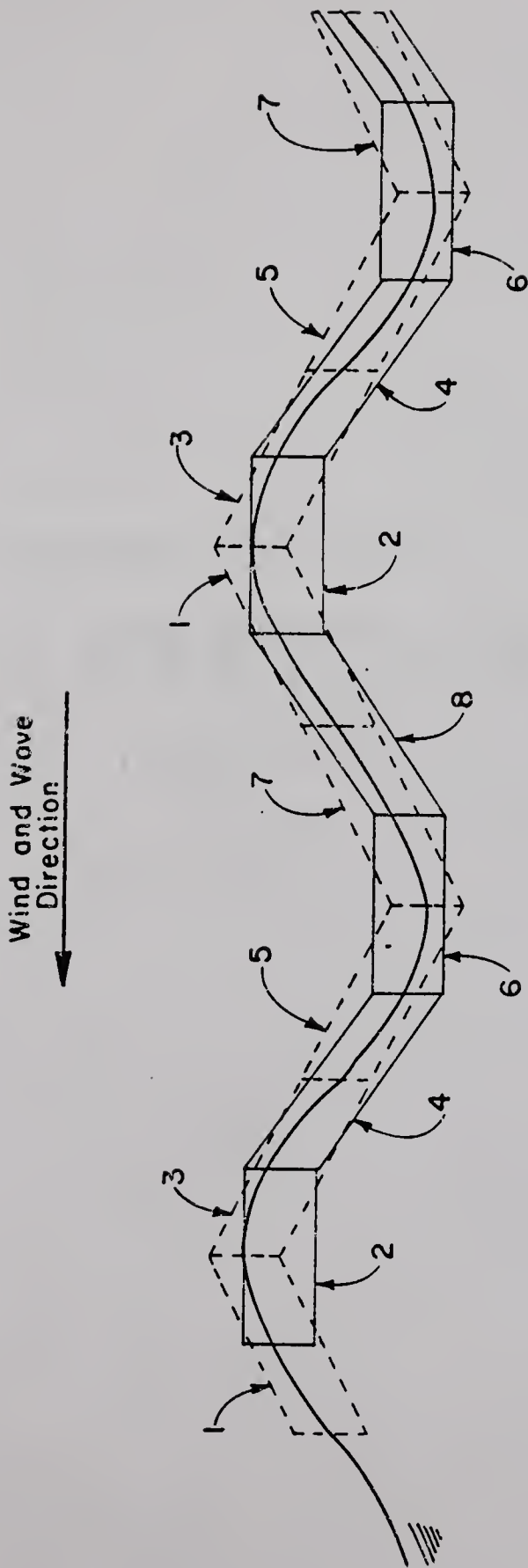


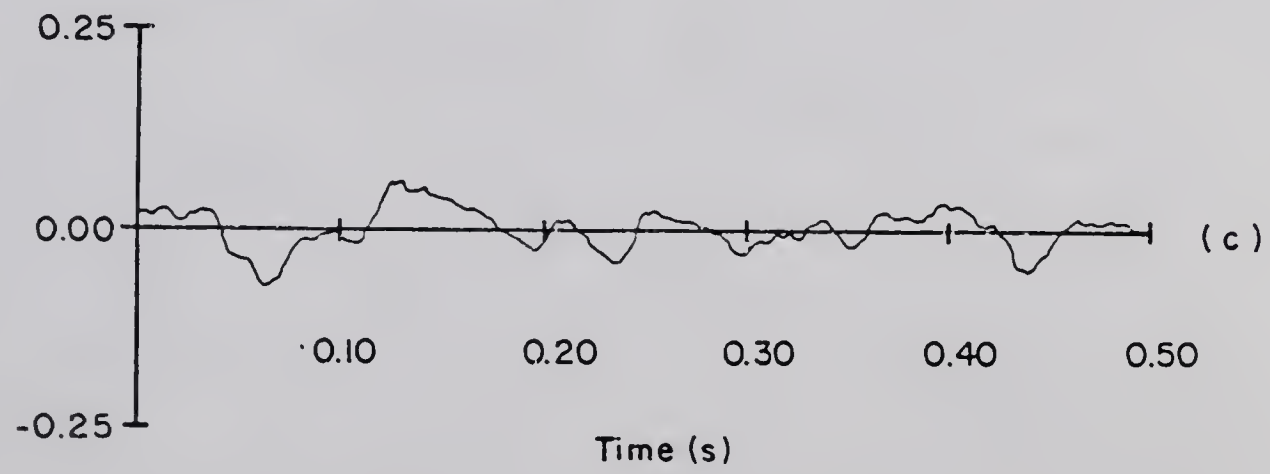
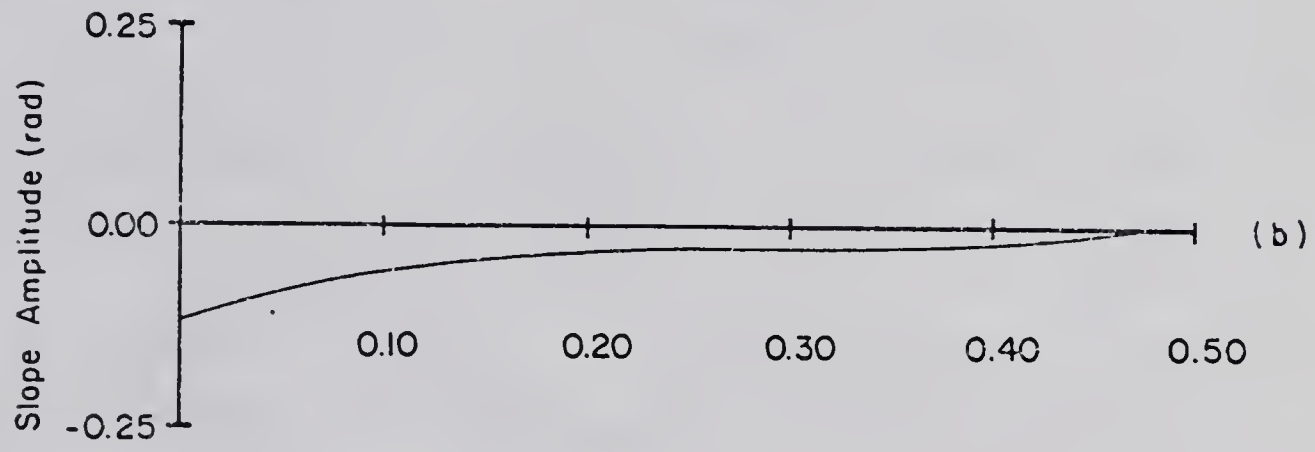
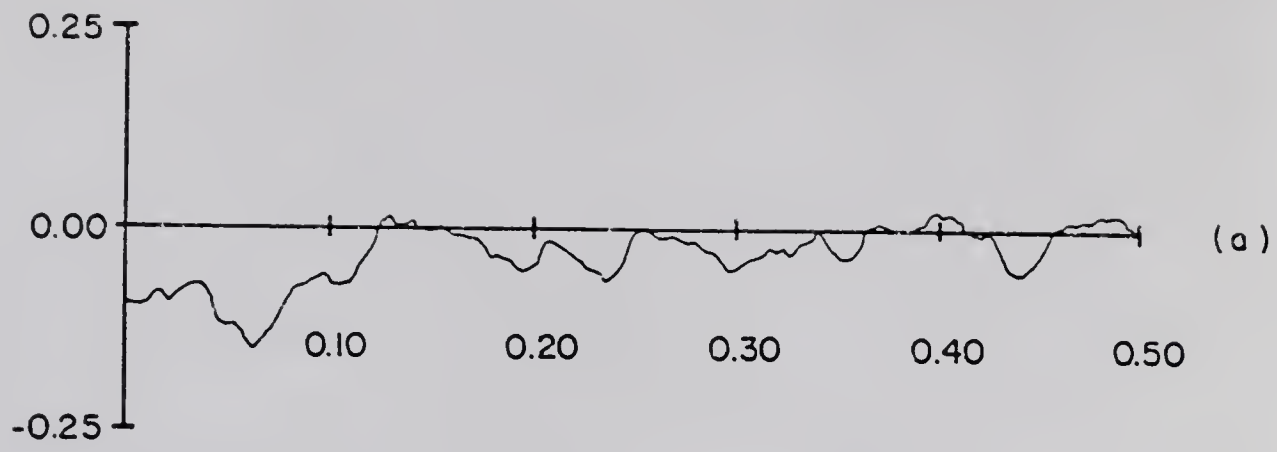
Figure 16. Wave record segmenting scheme used to produce short wave slope epics for phase averaging.

placed at low frequency by the trend create concern that the low frequency energy may spread to the higher frequency portion of the spectrum. To alleviate this difficulty the trend is removed by fitting a third degree polynomial to the data of each time series segment and subtracting it point by point from the original series. Figure 17 illustrates the effect on the time series of the trend removal operation for a typical segment of data. For low wind speeds the constructed polynomials fit the observed trends very well. At higher wind speeds the polynomial fit becomes erratic because it tends to follow the larger and longer period excursions in slope related to the wind driven wave system. Figure 18 illustrates the effect that trend removal has on the spectrum. For the conditions considered the figure shows that the long wave energy did not spread significantly into the high frequency region of most interest (above 9 Hz). However, good practice and the cases where the high frequency regions were affected to a greater extent dictated that the trend removal routine be applied to the low wind speed data. At higher wind speeds the low frequency trend assumes much less importance relative to the short wave slope values, so trend removal was not attempted for reference wind speeds above 5.9 m/s.

Simply stated, the results of the analysis for each test condition yield eight phase averaged slope spectral estimates, each attributed to a phase location along the wave profile as in Figure 16. The 256 point spectra have a frequency axis resolution of 1.56 Hz. The window function,  $W(j)$ , has the value 1.0 for the central 160 points of actual slope data in each segment and assumes the slope of half of a cosine bell for the data points 1 to 20 and 181 to 200. The spectral intensity estimates,  $I_k(n)$ , for the  $k$  time series segments,  $X_k(j)$ , of length,  $L$ , are corrected for the reduction in energy due to the window by a formulation

Figure 17. Visualization of a typical trend removal sequence. Reference wind speed: 4.9 m/s. Long wave:  $T = 2.0$  s,  $H = 10.0$  cm.

- a) Appearance of the front face total slope time series segment.
- b) The corresponding trend by third degree polynomial fit.
- c) Appearance of the high frequency slope time series after trend removal.

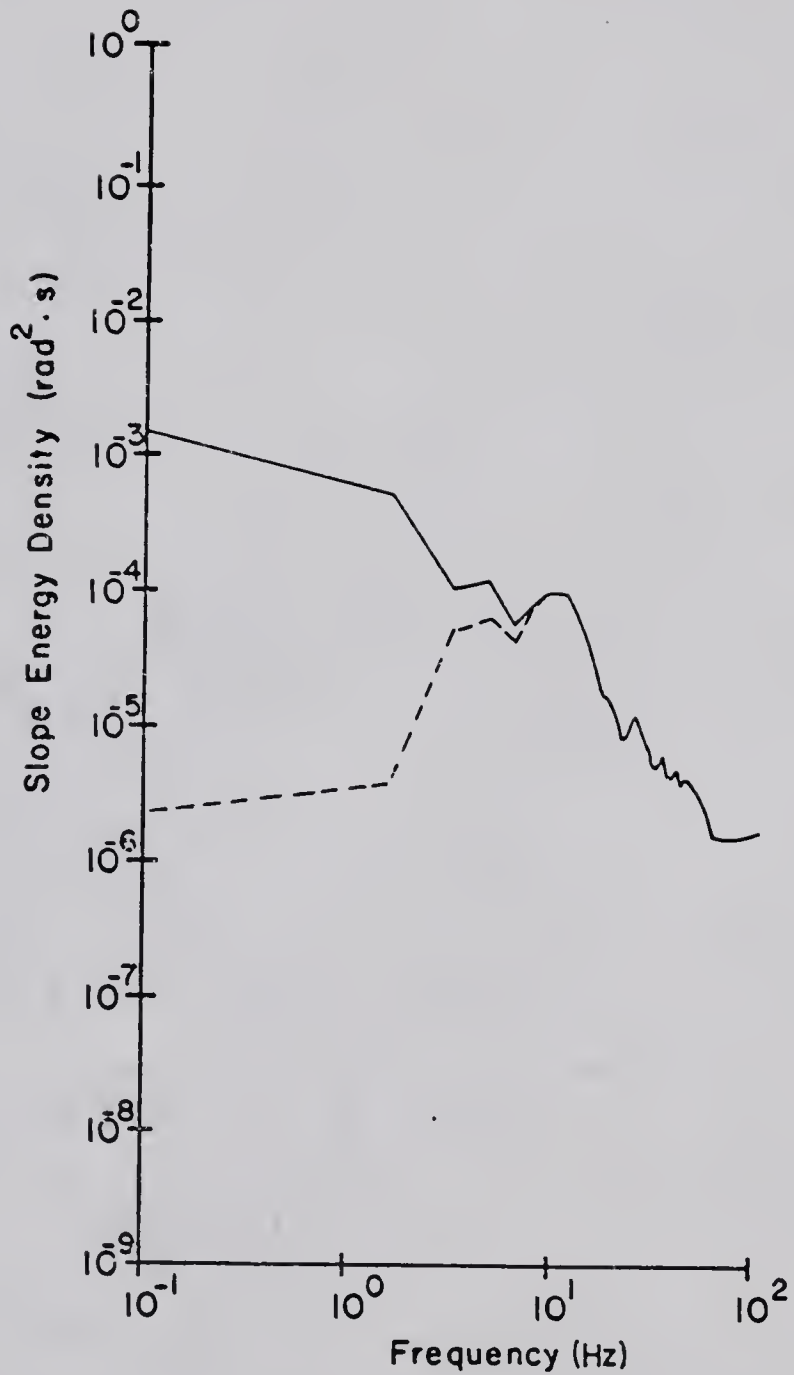


Time (s)

Figure 18. Phase averaged slope energy spectral estimate at the front face of the long wave crest. Reference wind speed: 4.9 m/s. Long wave:  $T = 2.0$  s,  $H = 10.0$  cm.

a) Without trend removal ———.

b) With trend removal - - - -.



suggested by Welch (1967) in his important paper on the FFT. The finite Fourier transform of each of the  $k$  segments is given by

$$A_k(n) = \frac{1}{L} \sum_{j=1}^{L-1} X_k(j) W(j) e^{-2\pi i(nkj/L)} \quad , \quad (3-22)$$

where  $L$  equals the 200 points of real data and  $i = \sqrt{-1}$ . The estimate of the energy spectrum for the  $k^{\text{th}}$  segment is then given by

$$I_k(n) = \frac{|A_k(n)|^2}{U} \quad , \quad (3-23)$$

where  $U$  is given as

$$U = \frac{1}{L} \sum_{j=1}^{L-1} W^2(j) \quad . \quad (3-24)$$

Hence, the effect of the cosine tapered window to reduce the spectral intensity values calculated by the FFT, as in equation (3-22), is normalized out by dividing each spectral point by the mean square value of the window, equation (3-24). For the computations here two windows were utilized. The 200 point window described above has a mean square value,  $U = 0.880$ . The 4064 point window to be described in Chapter VI has a mean square value,  $U = 0.938$ .

The stability of the estimate based on the ensemble of 133 independent sampled epics from a Gaussian process is specified in terms of the number of equivalent degrees of freedom (EDF) of the approximating chi-square distribution (Welch, 1967). For the short wave slope intensity estimates described above we have

$$\text{EDF} = 266 \quad . \quad (3-25)$$

This value holds for all but the end points of the spectrum, and implies a very stable spectral prediction.

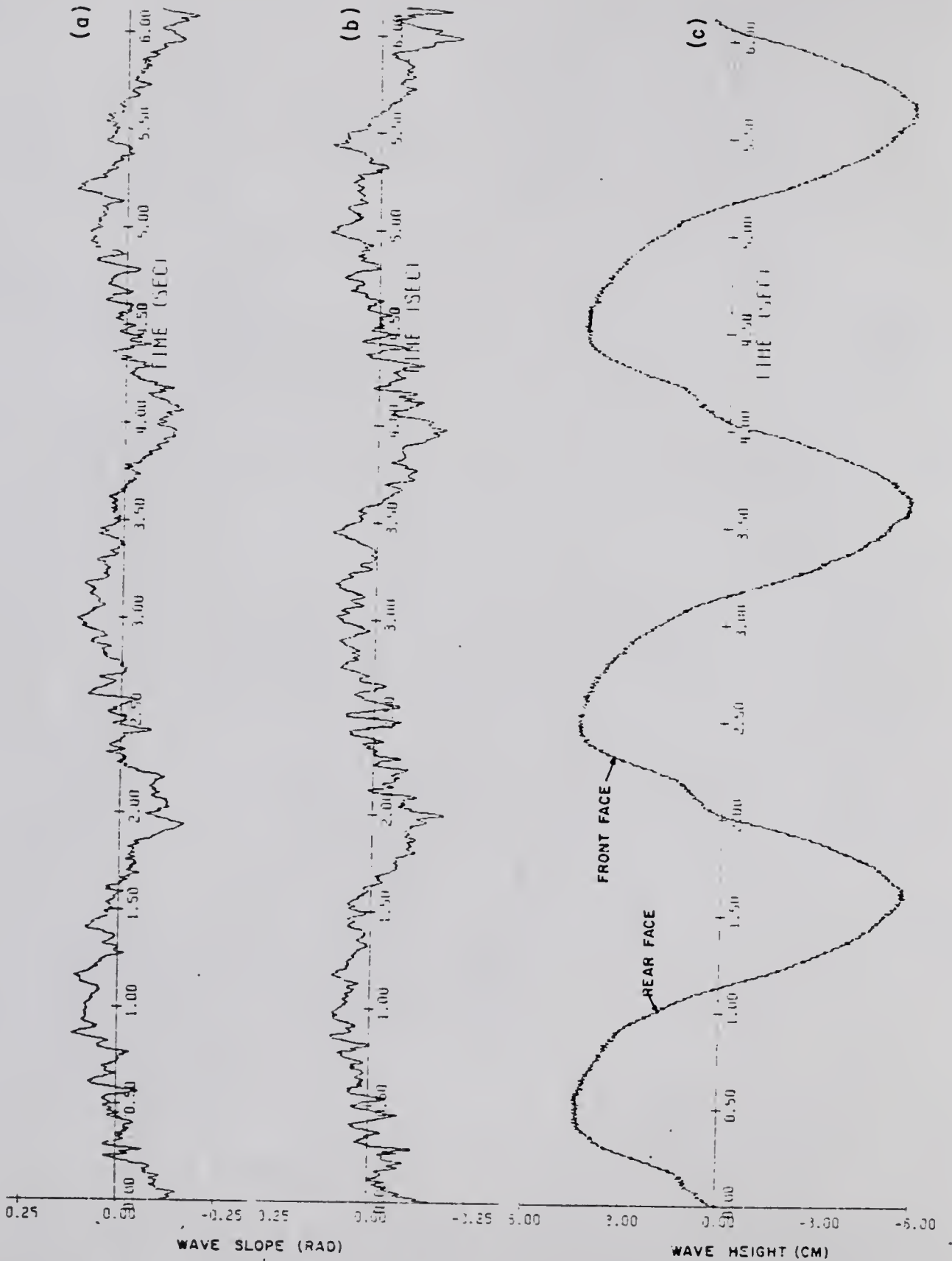
CHAPTER IV  
EXPERIMENTAL RESULTS

IV.A. Time Series Data

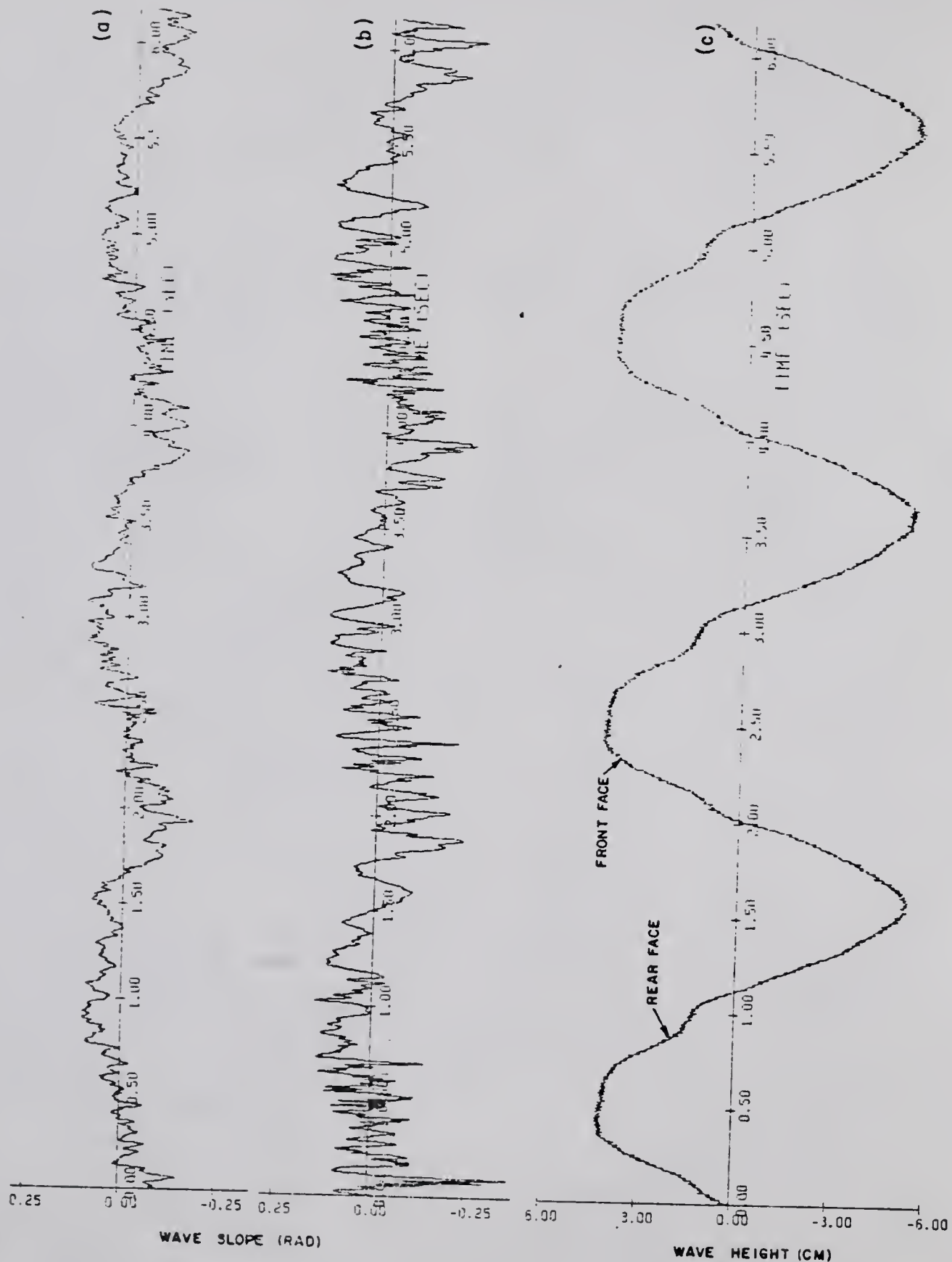
The time series data displayed in Figures 19 through 25 illustrate in a literal way the effects of the long wave motion on the short wave field at the nine different reference wind speeds from 3.8 m/s to 10.1 m/s. For the four lowest wind speeds it is seen from Figures 19 and 20 that the slope of the long wave represents a large portion of the total slope value measured at any instant. At a reference wind speed slightly larger than 5.0 m/s the intensity of the wind waves increases significantly. This is indicated in Figure 20, when the wind speed increases from 4.9 m/s to 5.6 m/s, by the increase in peakedness of the slope time series from parts a) to b).

At the reference wind speed of 5.6 m/s the effect of the presence of the long wave on the short wave field becomes manifest in the short wave time series. The resultant changes in the short wave field are most clearly visible in Figures 20b through 23. The long wave - short wave field interdependence results in two distinguishable effects on the short wave field characteristics. Firstly, if one thinks of a curve lying, as an envelope along the outer edges of the slope time series, containing the slope maxima and minima; it is clearly seen from Figures 20b through 23 that the envelope width is not constant and is in fact related to the long wave phase. Secondly, the frequency range

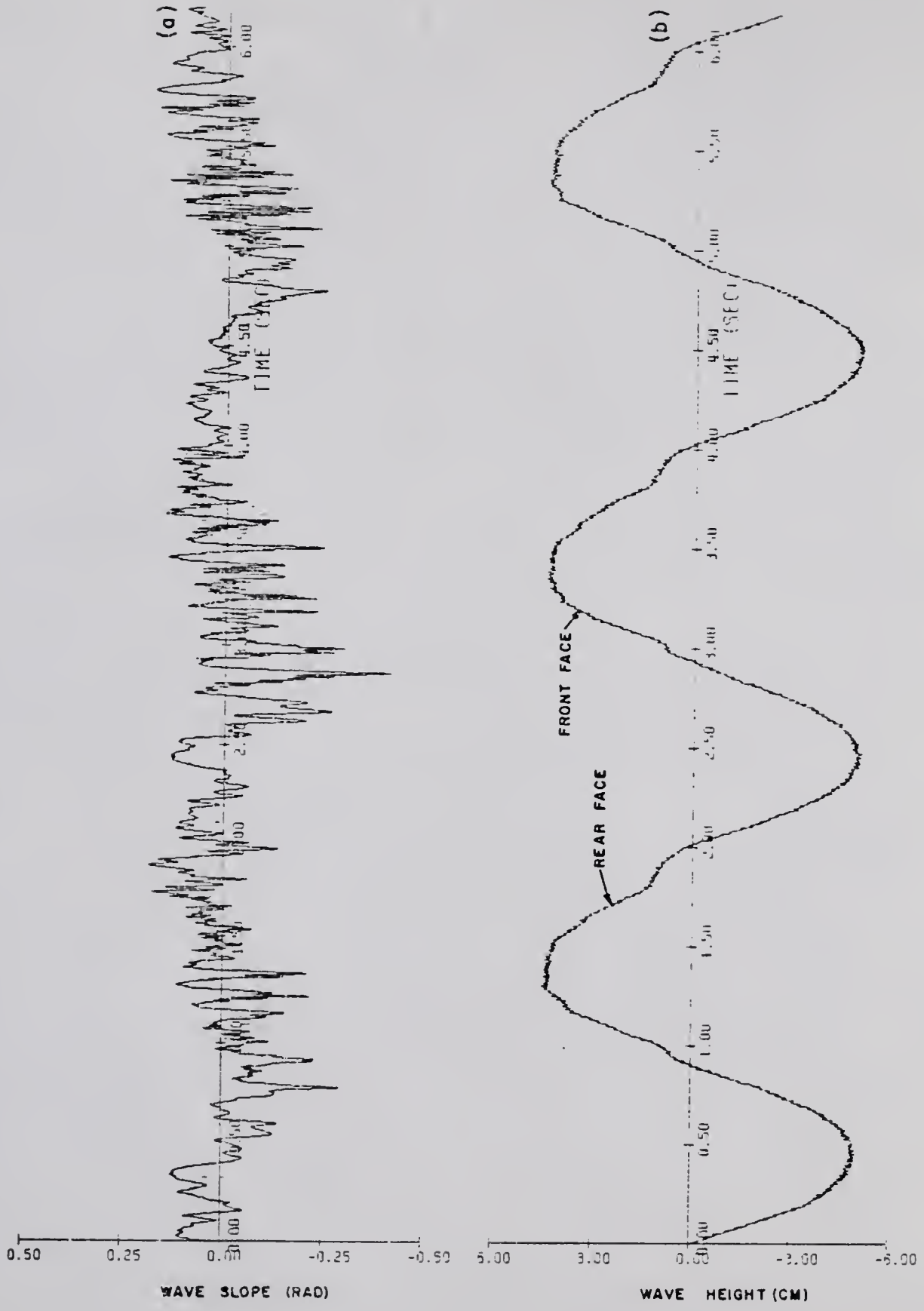
- Figure 19. Wave slope and height time records.
- a) Wave slope for reference wind speed = 3.8 m/s.
  - b) Wave slope for reference wind speed = 4.4 m/s.
  - c) Wave height:  $T = 2.0$  s,  $H = 10.0$  cm.



- Figure 20. Wave slope and height time records.
- a) Wave slope for reference wind speed = 4.9 m/s.
  - b) Wave slope for reference wind speed = 5.6 m/s.
  - c) Wave height:  $T = 2.0$  s,  $H = 10.0$  cm.



- Figure 21. Wave slope and height time records.
- a) Wave slope for reference wind speed = 5.9 m/s.
  - b) Wave height:  $T = 2.0$  s,  $H = 10.0$  cm.



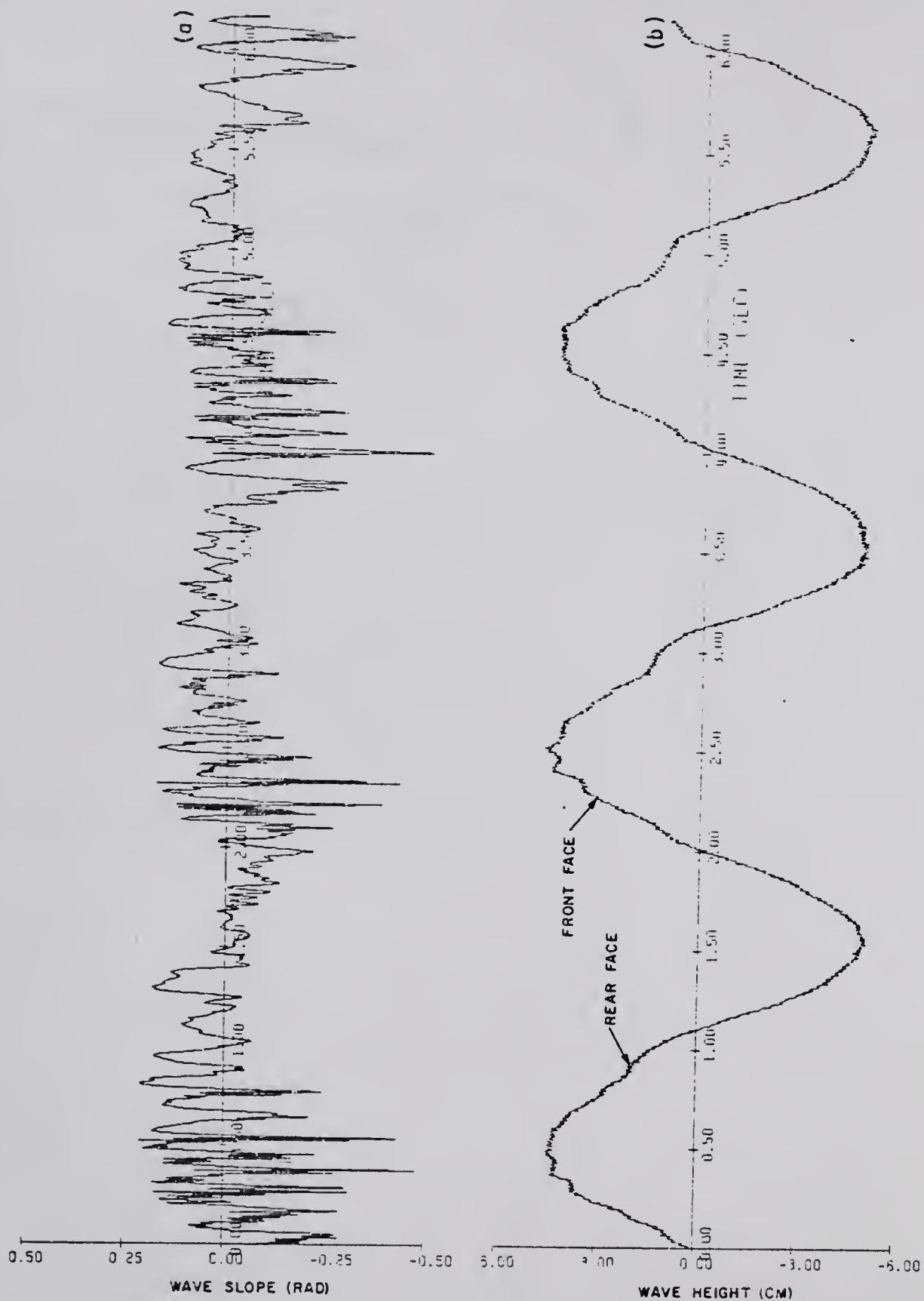
(a)

(b)

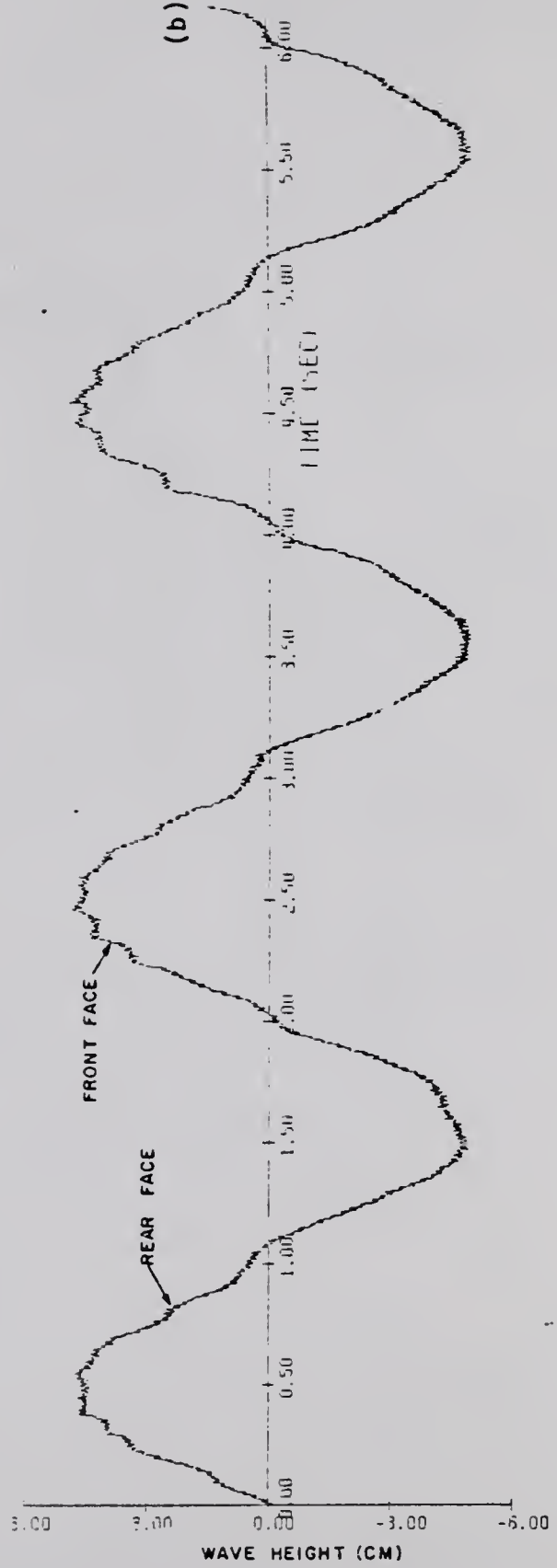
WAVE SLOPE (RAD)

WAVE HEIGHT (CM)

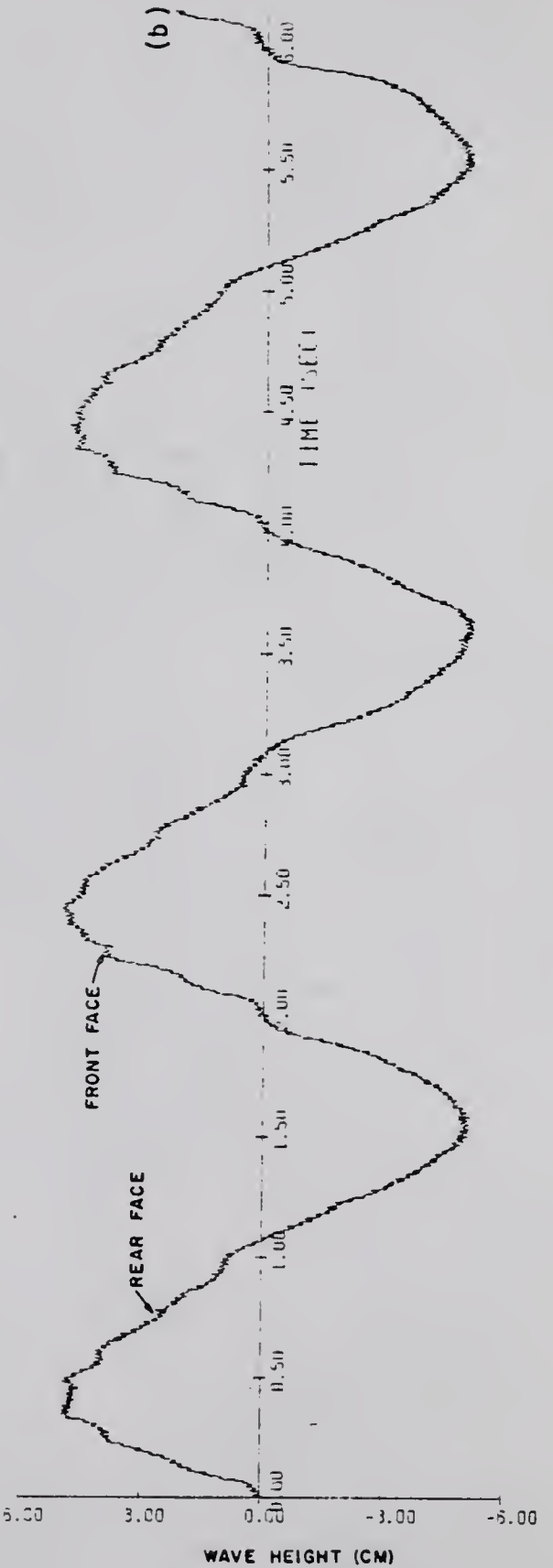
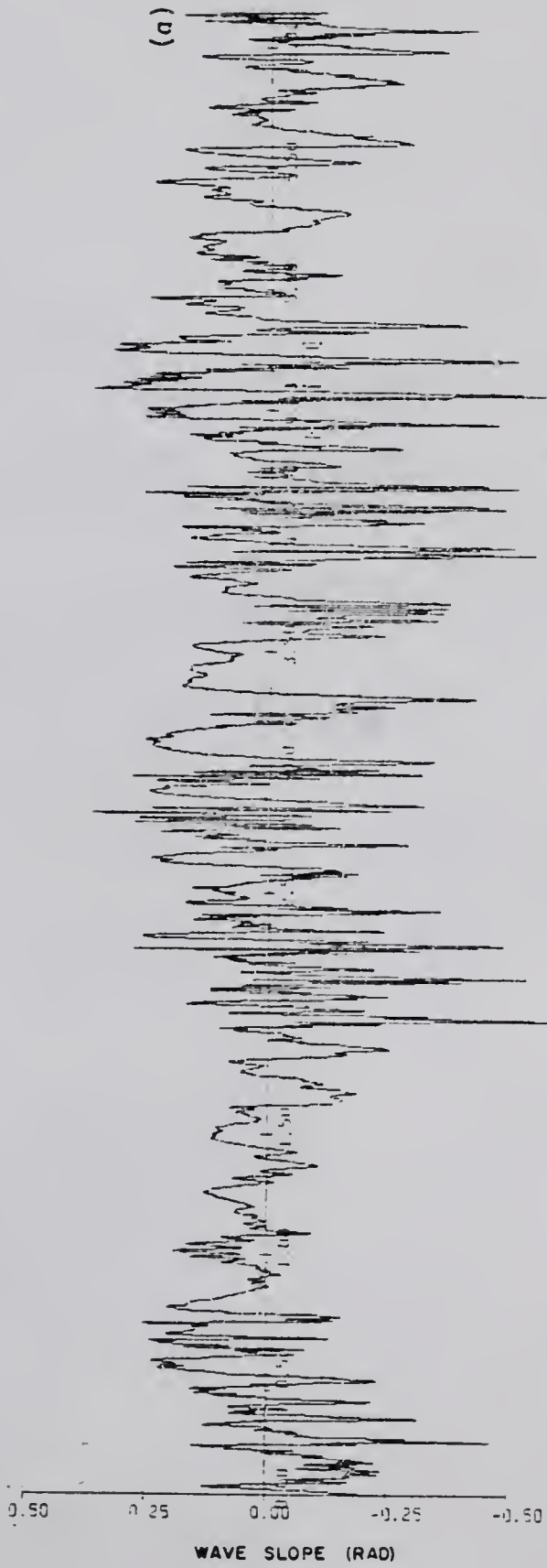
- Figure 22. Wave slope and height time records.
- a) Wave slope for reference wind speed = 7.2 m.s.
  - b) Wave height:  $T = 2.0$  s,  $H = 10.0$  cm.



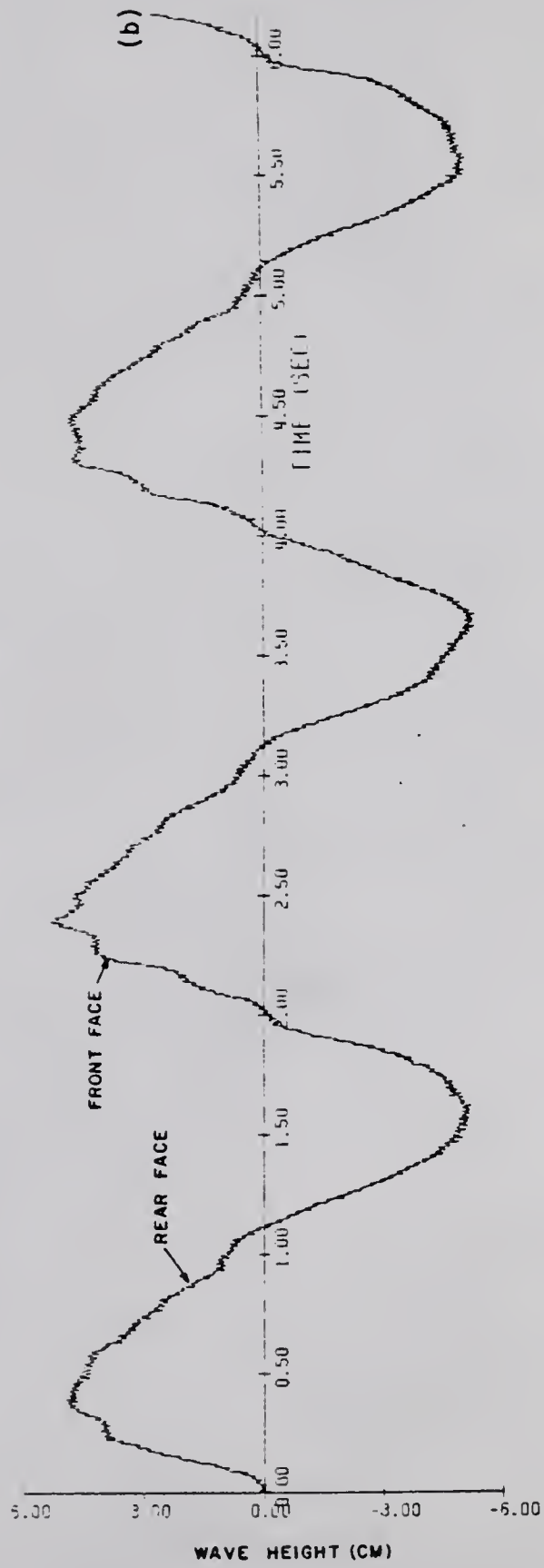
- Figure 23. Wave slope and height time records.
- a) Wave slope for reference wind speed = 8.3 m/s.
  - b) Wave height:  $T = 2.0$  s,  $H = 10.0$  cm.



- Figure 24. Wave slope and height time records.
- a) Wave slope for reference wind speed = 9.2 m/s.
  - b) Wave height:  $T = 2.0$  s,  $H = 10.0$  cm.



- Figure 25. Wave slope and height time records.
- a) Wave slope for reference wind speed = 10.1 m/s.
  - b) Wave height:  $T = 2.0$  s,  $H = 10.0$  cm.



associated with the short wave field varies along the long wave profile. This is illustrated quite clearly by the variation in raggedness of the slope time series of Figures 20b through 23 in relation to the long wave profile. Both wind wave frequencies and slope envelope widths reach maximum values in the vicinity of the front face of the long waves. When the reference wind speeds exceed 9 m/s, as they do for Figures 24 and 25, the frequency and envelope variations still occur but are not as apparent because they are obscured by the generally high intensity and broad frequency composition of the slope signal. By virtue of the physical appearance of these long wave related variations in the slope time series, it seems reasonable to designate them frequency and amplitude modulations. That is, the short wave slope time series is modulated in frequency and amplitude.

#### IV.B. First Order Spectra

The total slope spectra, displayed in Figures 26 through 28 for the nine different wind speeds, illustrate the effect of changing wind speed on the wave field. All of the spectra show an increase in slope intensity with increasing wind speed. It can be seen from the series of spectra that the first and second harmonics of the long wave, appearing at 0.977 and 1.465 Hz, respectively, suffer alteration at the higher wind speeds, while the fundamental, which appears at 0.488 Hz, remains unchanged by wind speed. The intensity level calculated for the first harmonic increases slightly at the highest wind speeds. The second harmonic intensity level decreases with increasing wind, so that by the 10.1 m/s wind speed it has been reduced to the level of the wind driven portion of the spectrum.

It has already been noted that the time series indicate a somewhat abrupt increase in the slope intensity for a reference speed in the neighborhood of 5.0 m/s. A frequency by frequency comparison of the spectra calculated for 4.9 m/s and 5.6 m/s wind speed (Figures 26 and 27, respectively) shows that there is a large increase in slope intensity in the regions from 2.0 to 10.0 Hz and 20.0 to 60.0 Hz. The 2.0 and 10.0 Hz region shows the most striking increase.

The highest spectral level in the wind driven portion of the spectrum is reached in the frequency band at 3.22 Hz. Also in that region, say from 2.0 to 10.0 Hz, the spectra tend to develop a plateau region where the spectral intensity does not vary greatly. In the middle range of wind speed, Figure 27, a second plateau region begins to form in the 20.0 to 70.0 Hz region. As wind speed increases further, Figure 28, the

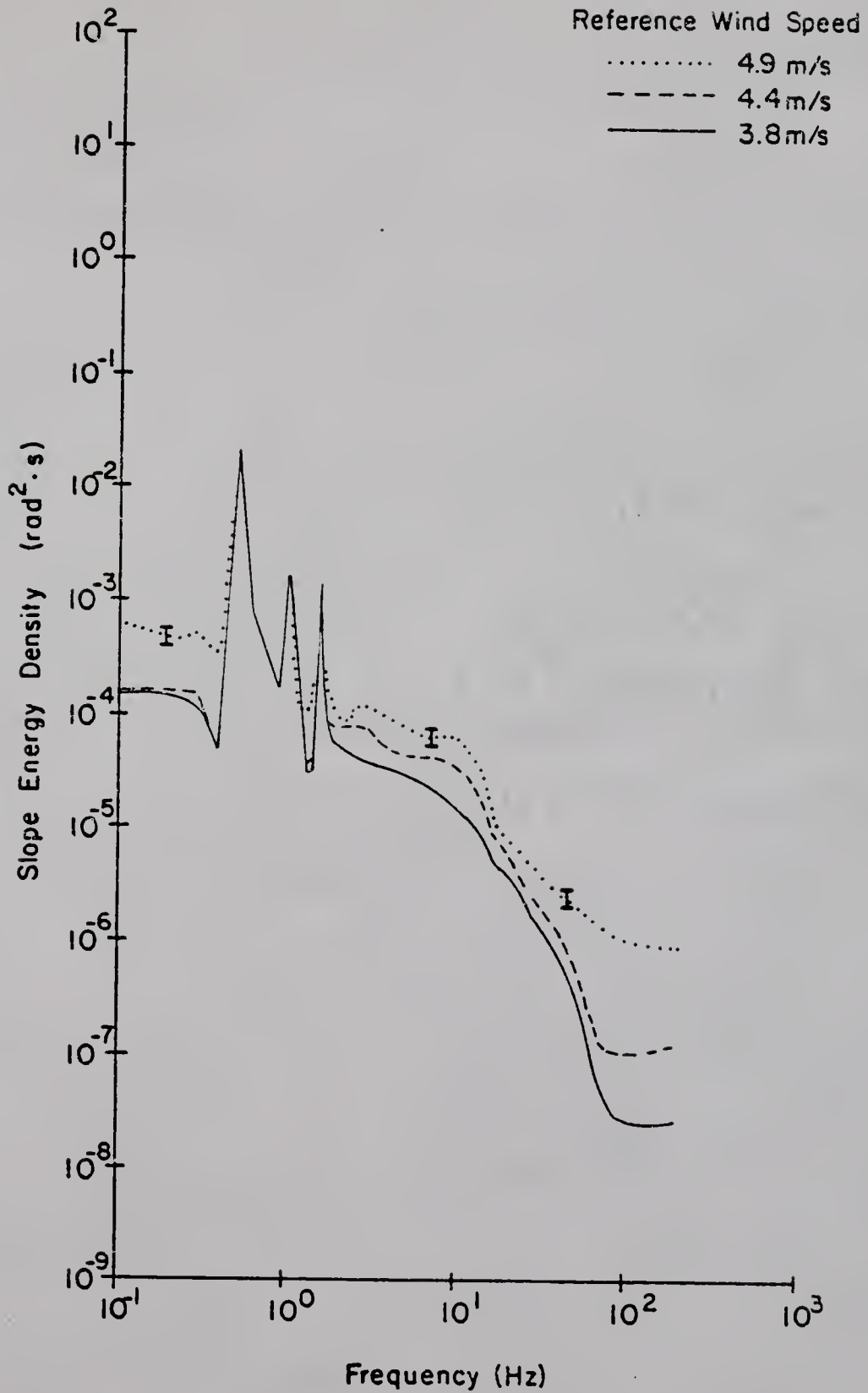


Figure 26. Average total wave slope spectra for wind speeds 3.8 to 4.9 m/s. Long wave:  $T = 2.0$  s,  $H = 10.0$  cm.

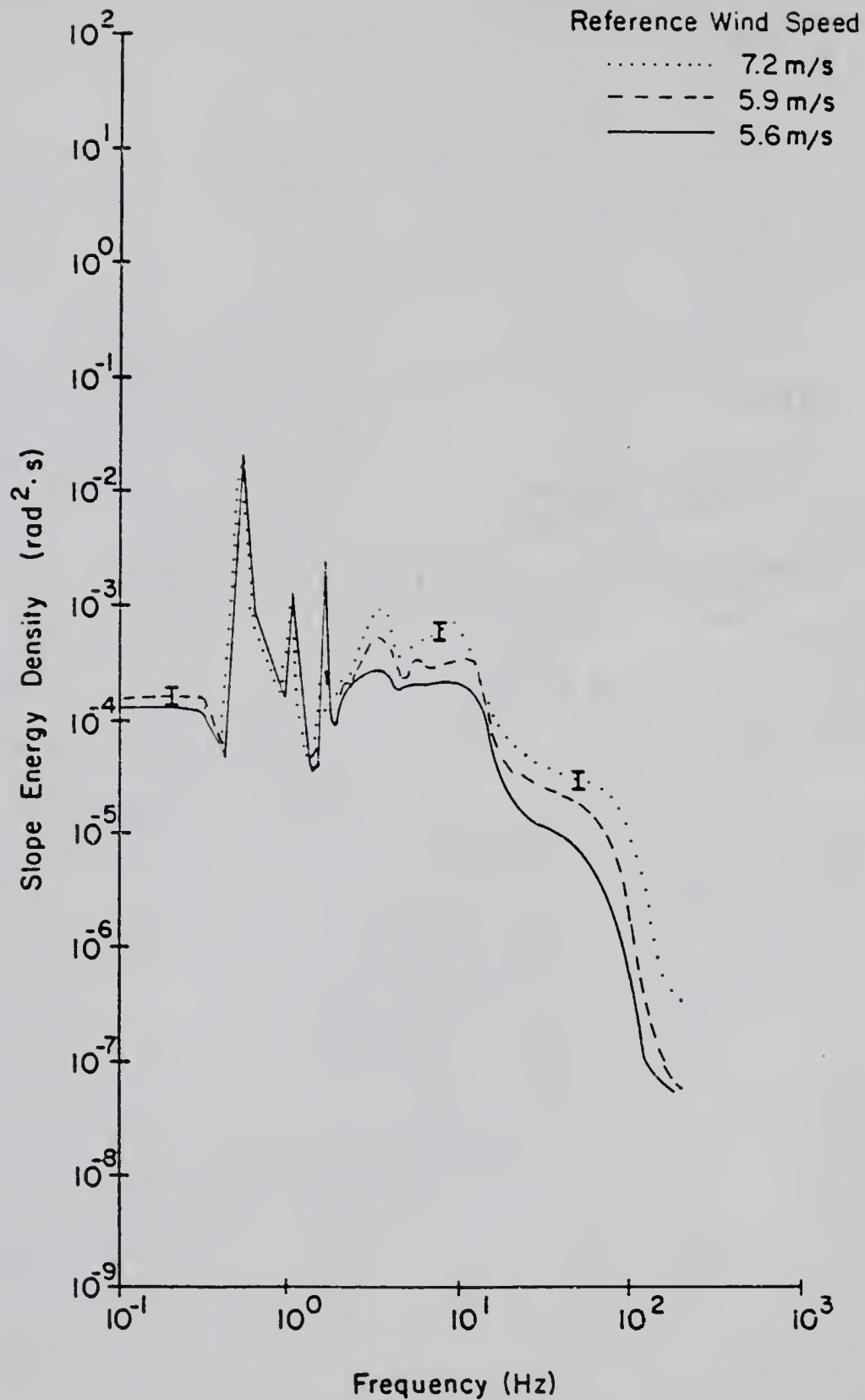


Figure 27. Average total wave slope spectra for wind speeds 5.6 to 7.2 m/s. Long wave:  $T = 2.0$  s,  $H = 10.0$  cm.

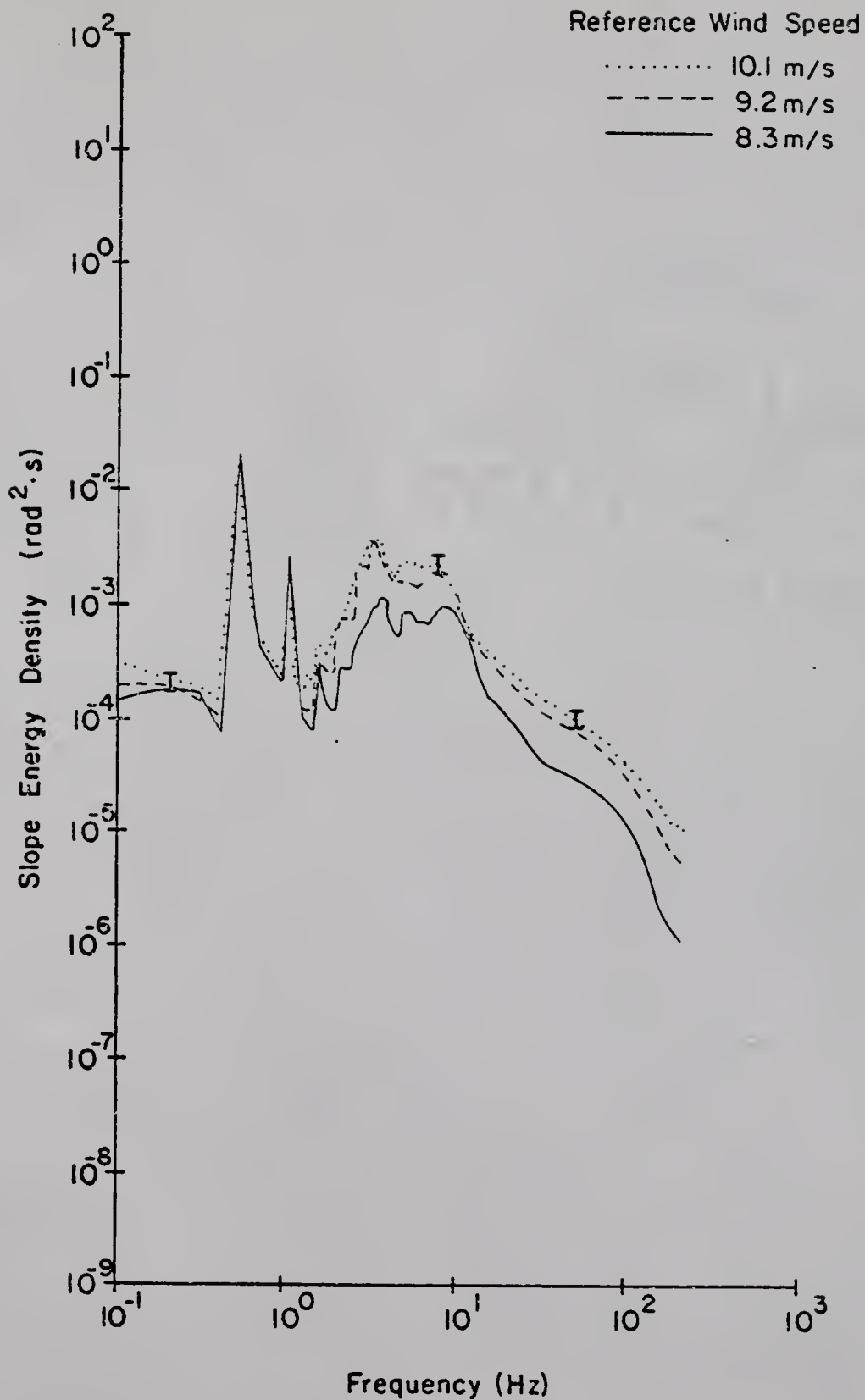


Figure 28. Average total wave slope spectra for wind speeds 8.3 to 10.1 m/s. Long wave:  $T = 2.0$  s,  $H = 10.0$  cm.

region between the two plateaus fills in, as a result of rising intensities, and eliminates the second plateau.

Error bars shown at three positions in each of the Figures 26 through 28 indicate the variability of the estimates for a 90% confidence interval.

#### IV.C. Spectral Modulations

Modulation effects produced by the long wave are clearly detectable in the short wave slope intensity spectra. For the spectrum to be a good tool for quantifying the modulation, it is necessary to discriminate between the two modulation components - frequency and amplitude. The overall changes in the shape of the short wave slope intensity spectra, as a result of phase location along the long wave profile, are illustrated at the two wind speeds of 4.9 m/s and 5.6 m/s in Figures 29 and 30, respectively. Note that the curve representing the intensity calculated for the crest region is similar in shape to but located considerably to the right of the curve representing the intensity calculated for the trough region.

If the frequency modulation of the variance elements that compose the spectrum was quantified, it would be possible to identify the remainder of the spectral variation related to the long wave as an amplitude modulation of the intensity level within a selected variance element. There are two ways to approximate the frequency modulation of the spectrum. The first is by a graphical calculation. This method is applied by shifting the spectral plots, generated for each of the eight phase point segments, along the frequency axis until the best match is found. In Figure 29, for example, this would require shifting the solid line to the left until it most accurately overlaid the dashed line. The indicated frequency shift would be a measure of the relative advection effect between the two phase locations being compared. No consideration of the mean advection due to wind drift and inconsistent shifts related to the irregularities in the spectral shape are weaknesses of this method.

Figure 29. Phase averaged short wave slope spectra from the crest and trough regions of the long wave profile for Experiment E3 and Test T15. Reference wind speed = 4.9 m/s. Long wave:  $T = 2.0$  s,  $H = 10.0$  cm.

- a) ——— Calculated from the crest region.
- b) - - - Calculated from the trough region.
- c) . . . Spectral density calculated for the crest region after the removal of the frequency advection shift predicted to occur between the crest and trough locations.

The error bars indicated on the solid line apply to the other lines as well and suggest the limits of the 90% confidence interval.

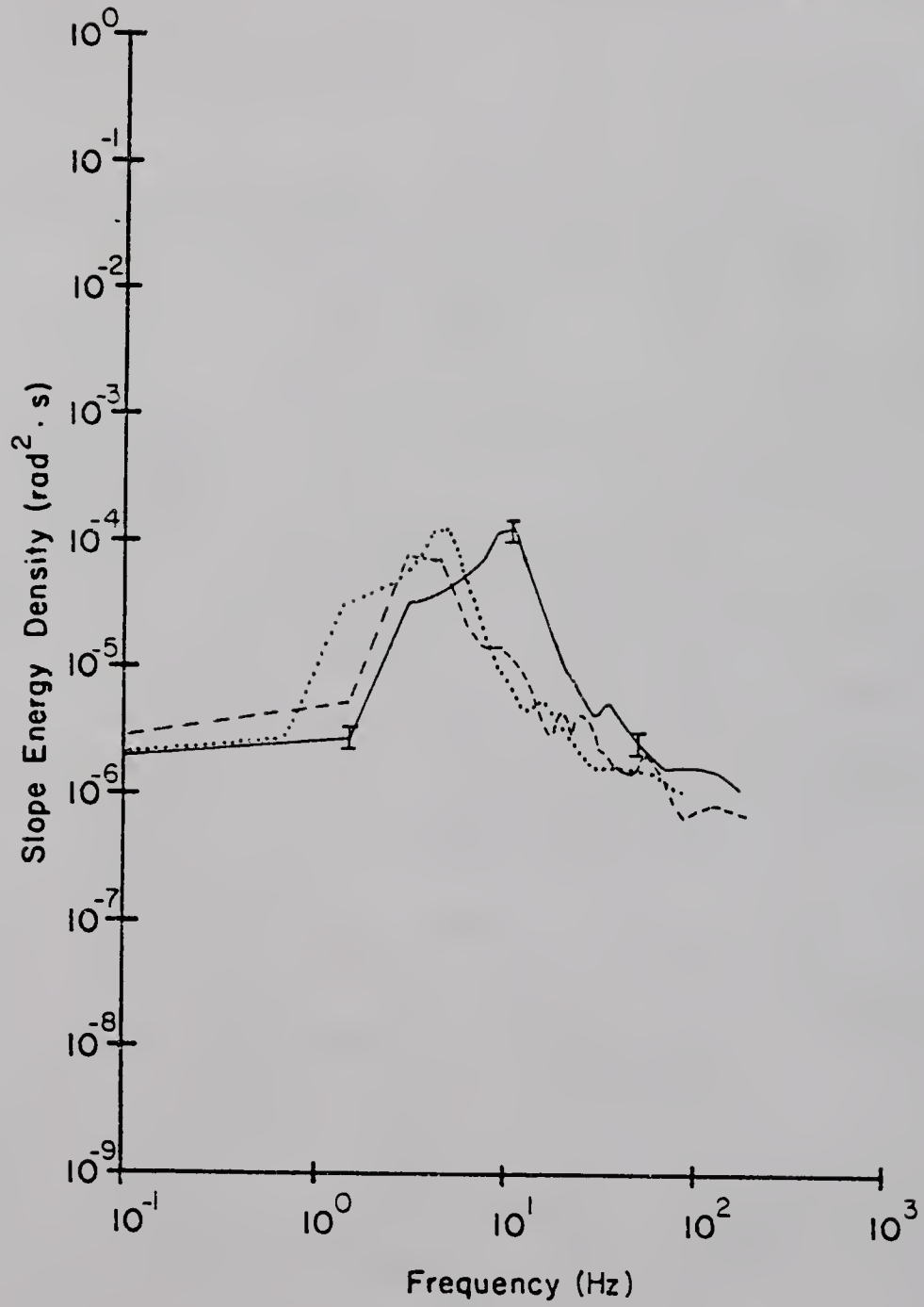
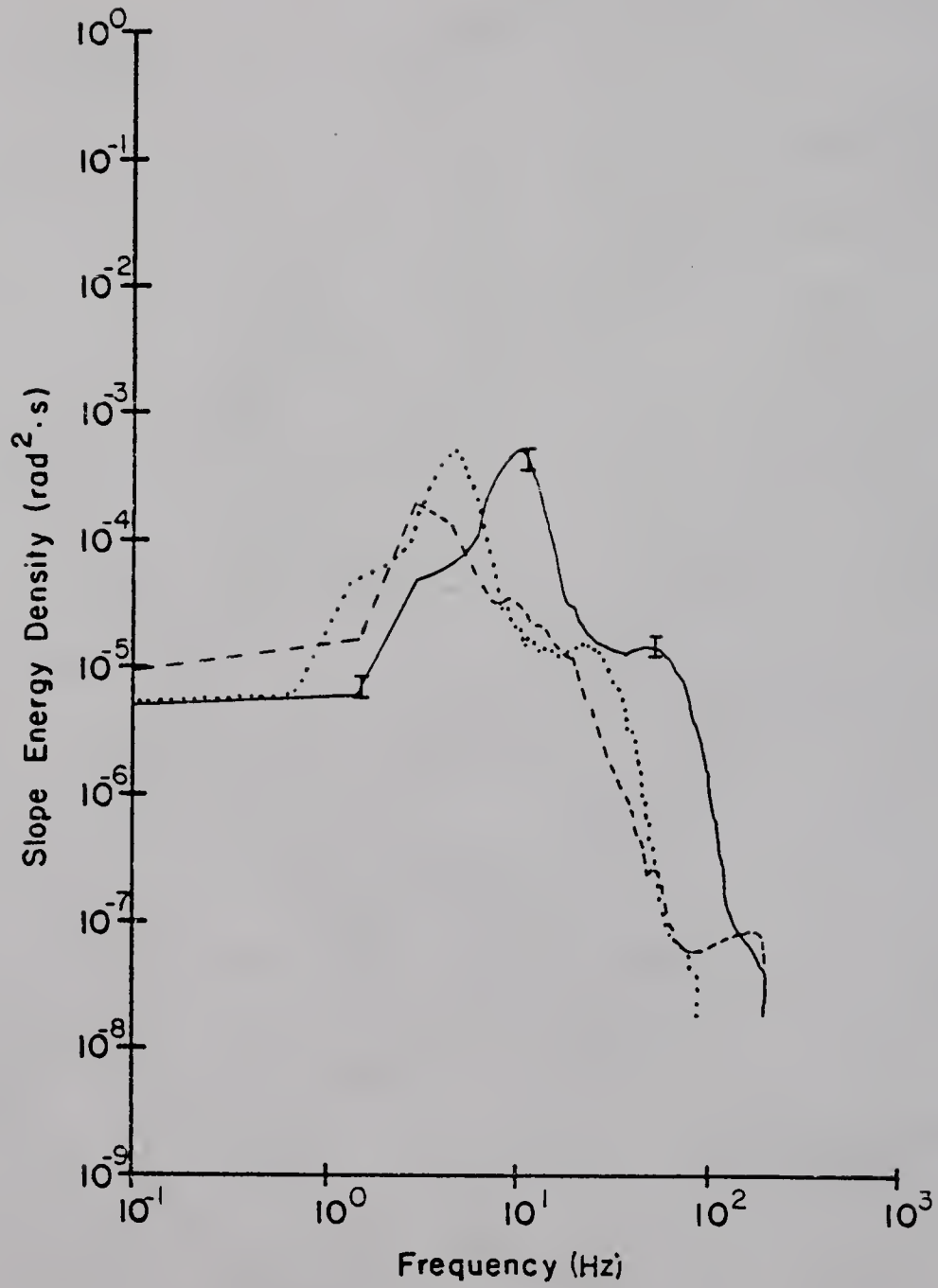


Figure 30. Phase averaged short wave slope spectra from the crest and trough regions of the long wave profile for Experiment E3 and Test T16. Reference wind speed = 5.6 m/s. Long wave:  $T = 2.0$  s,  $H = 10.0$  cm.

- a) ——— Calculated from the crest region.
- b) - - - Calculated from the trough region.
- c) . . . Spectral density calculated for the crest region after the removal of the frequency advection shift predicted to occur between the crest and trough locations.

The error bars indicated on the solid line apply to the other lines as well and suggest the limits of the 90% confidence interval.



The second method of obtaining an approximation to the frequency modulation is through the calculation of local frequency based on the changing short wave phase speed,  $c_s(x)$ , corresponding to wavenumber,  $k_s(x)$ . In what follows the subscript 0 refers to quantities obtained from the linear wave solution. The subscript, s, refers to the modified local value of a quantity. The subscript  $\ell$  refers to a quantity associated with a long wave. For this formulation the long wave orbital velocity is specified at the surface to first order by

$$U_\ell(x) = a_\ell \sigma_\ell \sin(k_\ell x) \quad . \quad (4-1)$$

The wind drift velocity is assumed to be a constant value at the surface,  $U_d$ . The velocity of propagation of a short wave form to first order in wave slope is given by the sum of the short wave phase velocity,  $c_0$ , the long wave orbital component,  $U_\ell(x)$ , and the wind drift  $U_d$ . So we have

$$c_s(x) = c_0 + U_d + a_\ell \sigma_\ell \sin(k_\ell x) \quad . \quad (4-2)$$

The local short wave wavenumber,  $k_s$ , can be approximated by use of the second order radiation stress calculations of Longuet-Higgins and Stewart (1960). For the long wave under consideration  $k_s$  is given by

$$k_s(x) = k_0 + a_\ell k_\ell k_0 \sin(k_\ell x) \quad . \quad (4-3)$$

The product of equations (4-2) and (4-3) then yields an expression for the local short wave frequency,  $\omega_s(x)$ . The expression is

$$\begin{aligned} \omega_s(x) = k_s(x)c_s(x) = & k_0 c_0 + k_0 c_0 a_\ell k_\ell \sin(k_\ell x) + k_0 a_\ell \sigma_\ell \sin(k_\ell x) \\ & + a_\ell k_\ell (a_\ell \sigma_\ell k_0) \sin^2(k_\ell x) + k_0 U_d + k_0 U_d a_\ell k_\ell \sin(k_\ell x) \quad , \quad (4-4) \end{aligned}$$

through the order  $(a_\ell k_\ell)^1$ . Retaining those terms of order  $(a_\ell k_\ell)^0$ , equation (4-4) becomes

$$\omega_s(x) = \omega_0(k_s) + k_0 [U_\ell(x) + U_d] \quad . \quad (4-5)$$

The dotted curves of Figures 29 and 30 represent the spectra calculated at the long wave crests shifted in frequency location by the amount indicated by equation (4-5). The expression (4-5) in practice used a wind drift velocity estimated to be 3% of the reference wind speed (Shemdin, 1972).

It was found that by retaining terms up through first order in long wave slope that only a 4% change in the approximation resulted. This fact, and the good results of Sinitsyn et al. (1973) with the linear expression are felt to justify its use here as an approximation for the frequency modulation. For the wind speeds of 3.8, 4.4, 4.9, 5.6, 8.3, 9.2, and 10.1 m/s the graphically and linearly calculated frequency shifts were in substantial agreement. The tests with the wind speeds of 5.9 and 7.2 m/s exhibited shifts that may have been underestimated by the linear calculation of equation (4-5). An additional graphical shift almost as large as the calculated shift could have made the peaks and very high frequency spectral values from the crest and trough segments overlay.

#### IV.D. Amplitude Modulation of the Spectrum

Figures 31 and 32 illustrate for two tests at 4.9 and 5.6 m/s wind speeds, respectively, the overall spectral variation that occurs along the wave profile for the selected frequencies of 6.25, 9.38, 12.50, and 15.63 Hz. To construct Figures 31 and 32 the value of the spectral density for the variance element represented by the indicated free wave frequency is plotted at each of the eight phase locations along the wave profile. These values are obtained by entering the phase averaged estimates of the short wave spectrum, calculated at each of the eight positions along the long wave profile, with the same frequency (for example, 6.25 Hz), and reading the spectral density associated with that variance element. The intensity excursions are large relative to the mean intensity of a given variance element, and the peaks occur in the region of the long wave crests. Figures 33 and 34 display results from the same tests as Figures 31 and 32, respectively. Again the eight spectral density values plotted for each indicated frequency come from the phase averaged estimates of short wave intensity at one of the eight long wave phase locations. However, in Figures 33 and 34 the advection correction calculated by equation (4-5) has been applied to the free wave frequencies indicated on the figures. Each of the phase averaged estimates of the short wave intensity is then entered with a frequency related to the free wave frequency selected, but adjusted for the local advection effect. The spectral density associated with the resultant frequency is recorded on the figures. The variation in intensity indicated by these plots represents the amplitude modulation effect on the short wave spectrum induced by the long wave. The figures show a trend toward a significant reduction in modulation as frequency is increased,

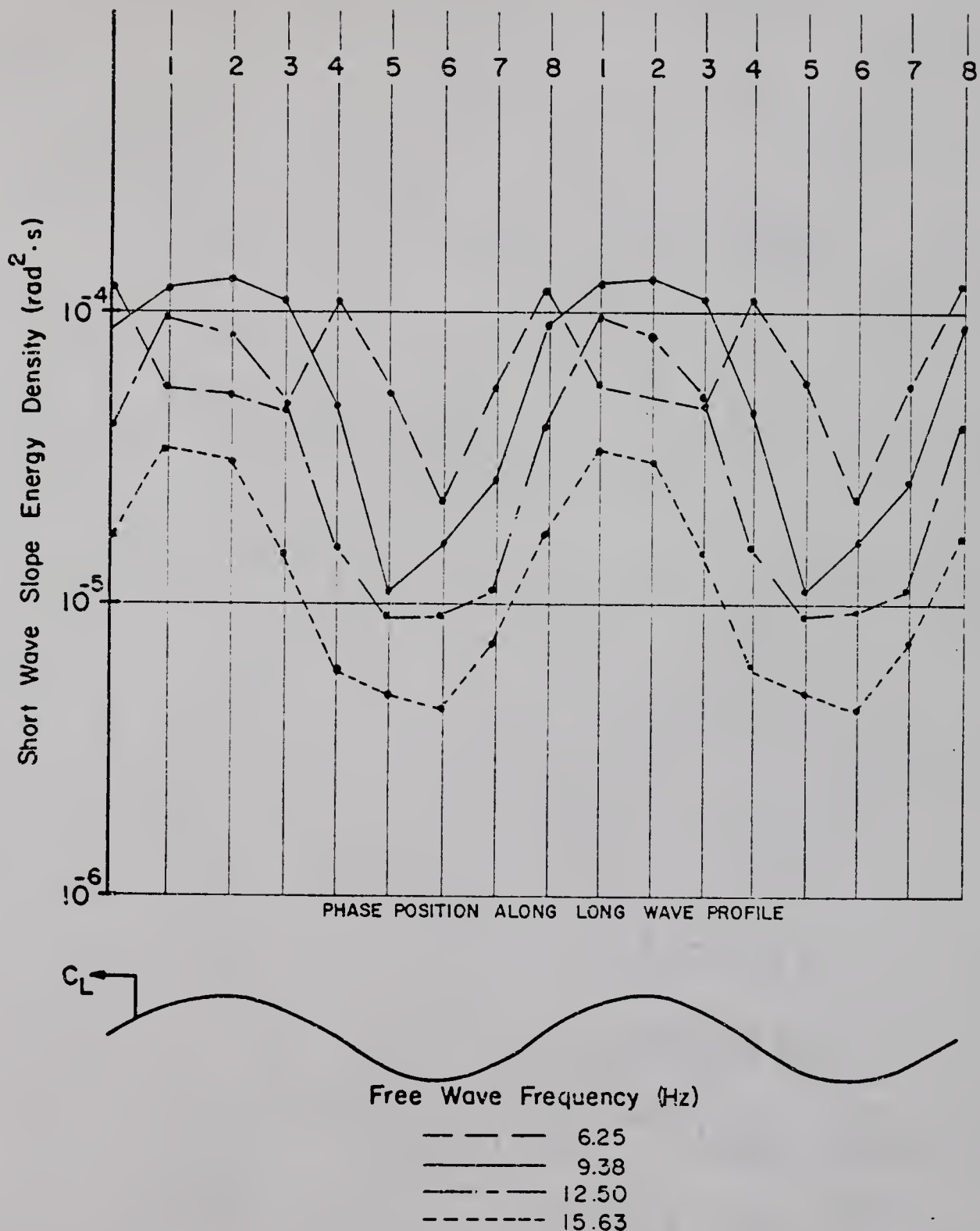


Figure 31. Example of the short wave energy modulation for selected free wave frequencies from experiment E3 and test T15. Advection is not considered. Reference wind speed = 4.9 m/s. Long wave:  $T = 2.0$  s,  $H = 10.0$  cm.

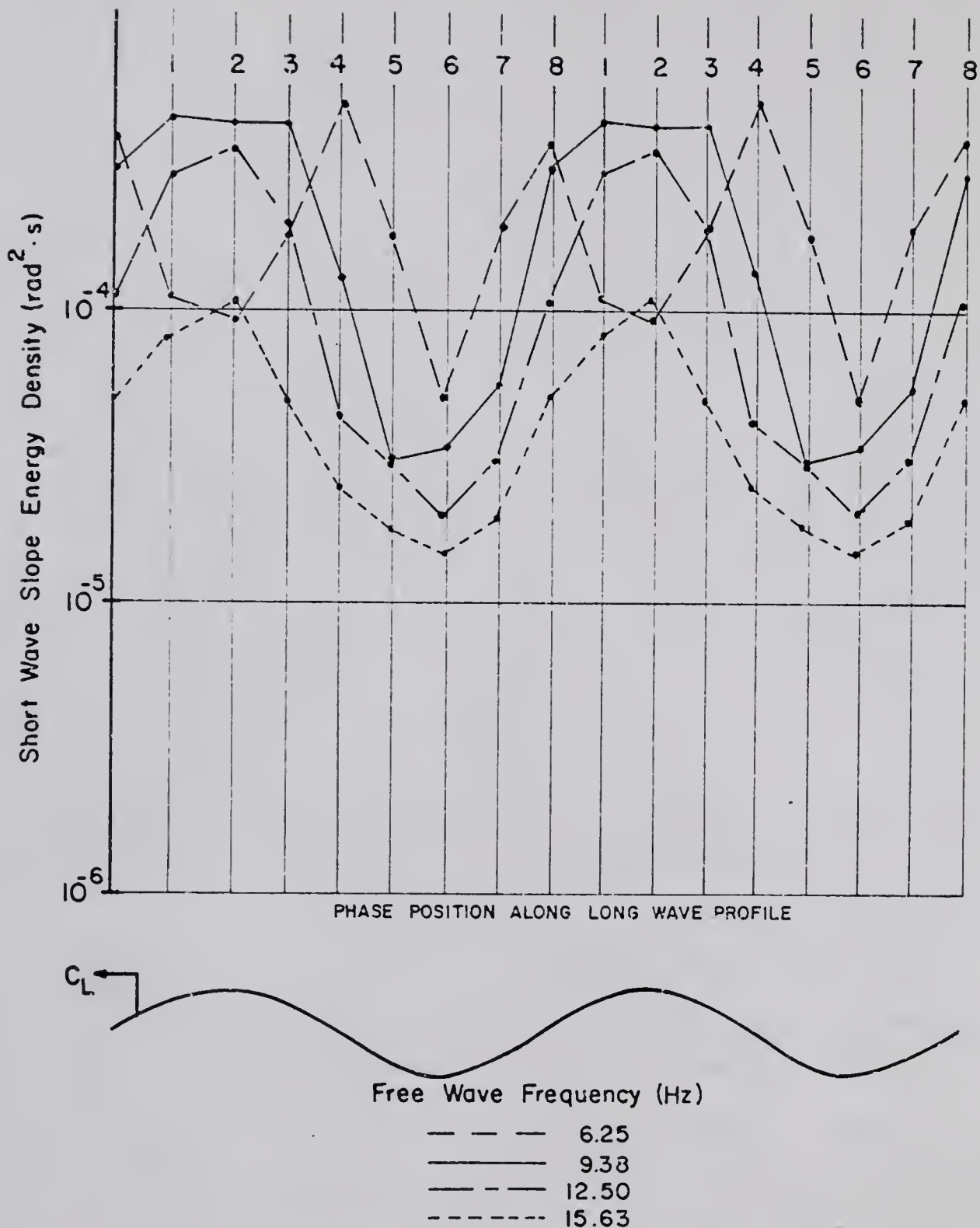


Figure 32. Example of the short wave energy modulation for selected free wave frequencies from experiment E3 and test T16. Advection is not considered. Reference wind speed = 5.6 m/s. Long wave:  $T = 2.0$  s,  $H = 10.0$  cm.

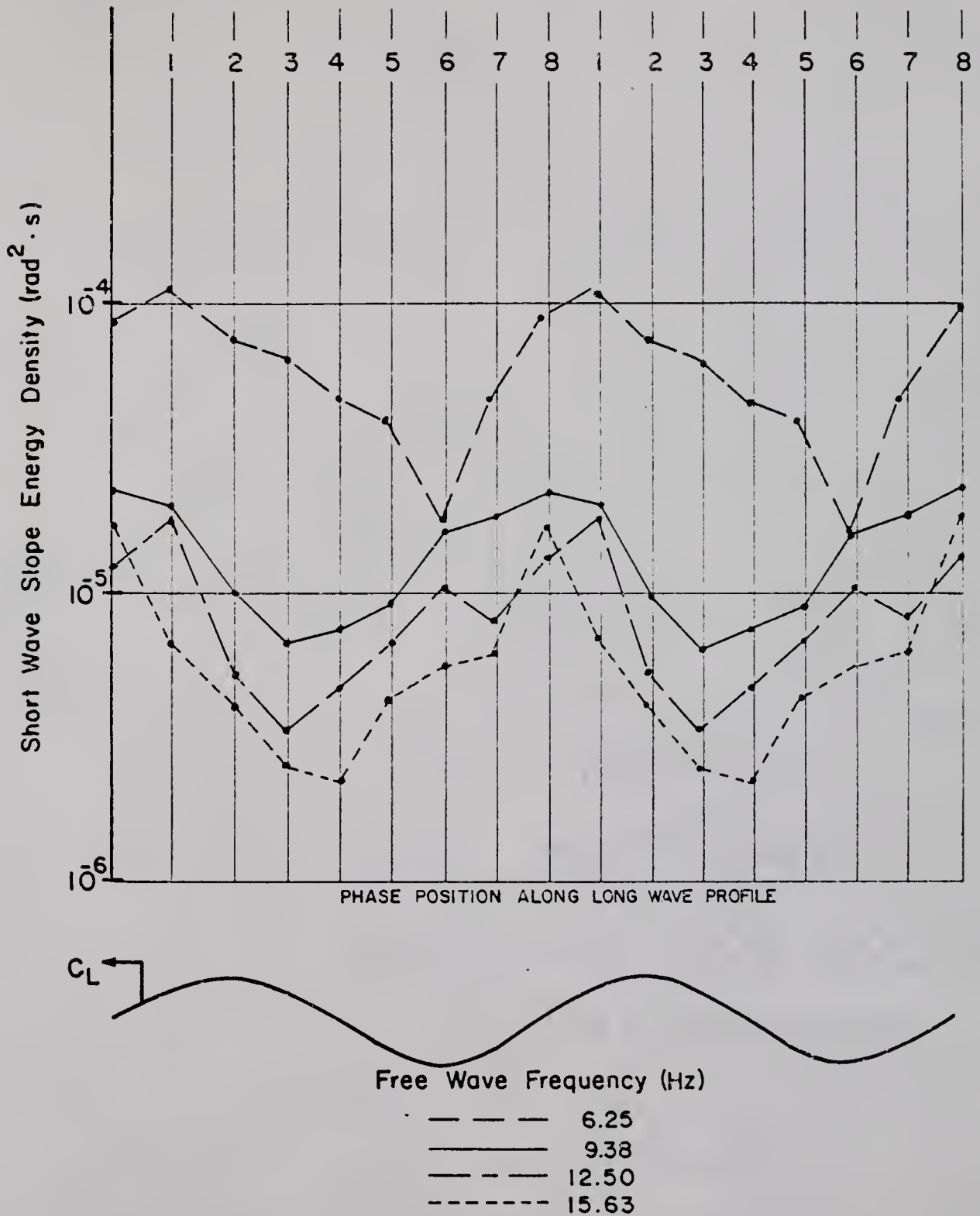
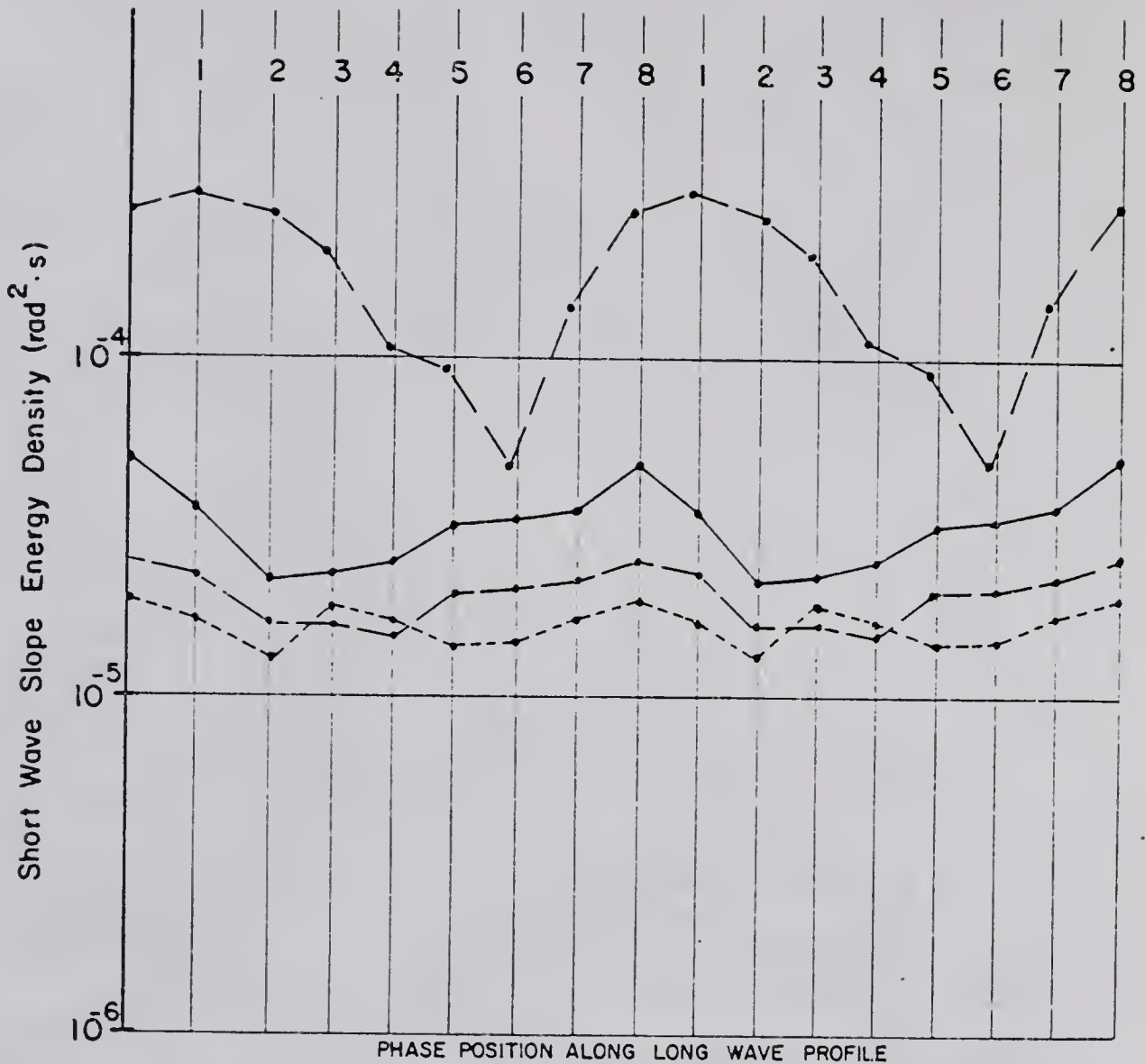


Figure 33. Example of the short wave energy modulation for selected free wave frequencies from experiment E3 and test T15. The advection correction is applied. Reference wind speed = 4.9 m/s. Long wave:  $T = 2.0$  s,  $H = 10.0$  cm.



Free Wave Frequency (Hz)

- 6.25
- 9.38
- · - · - 12.50
- · · · · 15.63

Figure 34. Example of the short wave energy modulation for selected free wave frequencies from experiment E3 and test T16. The advection correction is applied. Reference wind speed = 5.6 m/s. Long wave: T = 2.0 s, H = 10.0 cm.

a reduction in the actual energy excursion as frequency is increased, and a small shift in peak location toward the crest front face when compared to Figures 31 and 32.

CHAPTER V  
THEORIES OF INTERACTION  
BETWEEN SHORT WAVES AND LONG WAVES

In a wind generated sea the spectrum of waves is rather broad, ranging in frequency from 0.05 to 50 Hz. The waves interact in a continuous manner across the spectrum as mentioned in Chapter II.B.5. and II.B.6. Interactions between waves in noncontiguous frequency scales in a spectrum, such as the interaction between capillary waves and long gravity waves, are key issues in the energy transfer from wind to waves and in the remote detection of waves. This type of interaction was not discussed previously and is the focus of discussion in this chapter.

A simplified approach used to deal with noncontiguous scales of motion is to consider only two scales in which the large scale is composed of a periodic wave with known frequency and wavenumber. In an approximation of this sort one may consider the small scale waves (wind sea) to be closely tied to the wind field. The small scale waves may be considered either as a single, periodic wave (Longuet-Higgins and Stewart, 1960) or a wind generated spectrum (Keller and Wright, 1975). The small waves are modulated by the long wave, but are steady and homogeneous in the mean. Models of such interactions are discussed in what follows to develop a basis for evaluating the experimental results.

V.A. The Two-Scale Model of Longuet-Higgins and Stewart

Longuet-Higgins and Stewart (1960) considered the motion of two interacting waves when no generation or decay is occurring, and the two waves have significantly different scales. The boundary value problem, described below, corresponds to two dimensional irrotational motion of an inviscid, incompressible fluid of infinite depth. We have

$$\underline{U} = \nabla\phi(x, z, t) \quad , \quad (5-1)$$

$$\nabla^2\phi(x, z, t) = 0 \quad , \quad (5-2)$$

$$gz + \frac{1}{2} |\underline{U}|^2 + \frac{\partial\phi}{\partial t} = 0 \quad \text{at} \quad z = \eta \quad , \quad (5-3)$$

and

$$\nabla\phi(x, z, t) = 0 \quad \text{at} \quad z = -\infty \quad . \quad (5-4)$$

The equations are perturbed in the usual manner and expanded in Taylor series about the mean level,  $z = 0$ .

The first order problem is solved in the usual way, with the exception that the solution is taken to be the linear combination of two progressive wave motions well separated from each other in frequency or wavenumber scale. The solution is

$$\begin{aligned} \phi^{(1)} = & - \frac{a_1\sigma_1}{k_1} e^{k_1 z} \cos(k_1 x - \sigma_1 t + \theta_1) \\ & - \frac{a_2\sigma_2}{k_2} e^{k_2 z} \cos(k_2 x - \sigma_2 t + \theta_2) \quad . \end{aligned} \quad (5-5)$$

As is customary with second order problems, the solution arises in part from the driving action of the first order problem, which in this case is represented by  $\phi^{(1)}$ . The total value of the surface elevation resulting from the problem up through second order is given by

$$\eta = a_1 \sin \chi_1 - \frac{1}{2} a_1^2 k_1 \sin 2\chi_1 + a_2 \sin \chi_2 - \frac{1}{2} a_2^2 k_2 \sin 2\chi_2 - a_1 a_2 (k_1 \cos \chi_1 \cos \chi_2 - k_2 \sin \chi_1 \sin \chi_2) \quad , \quad (5-6)$$

where

$$\chi_i = k_i x - \sigma_i t + \theta_i \quad .$$

Now invoking the conditions that the wave of wavenumber,  $k_1$ , is of a much smaller scale than the second wave, and that we want to see how the second wave affects the wave of wavenumber,  $k_1$ ; the expression for  $\eta$  can be reduced to

$$\eta = a_1 \sin \chi_1 (1 + a_2 k_2 \sin \chi_2) - a_1 \cos \chi_1 (a_2 k_1 \cos \chi_2) \quad . \quad (5-7)$$

This result can be interpreted as having amplitudes and wavenumbers for the small scale wave that are modulated in response to the large wave with phase,  $\chi_2$ . The modulated amplitude is given by

$$a_1 = a_1 (1 + a_2 k_2 \sin \chi_2) \quad , \quad (5-8)$$

and the modulated wavenumber is given by

$$k_1 = k_1 (1 + a_2 k_2 \sin \chi_2) \quad . \quad (5-9)$$

The effect the solution displays is that both the small scale wave amplitude and wavenumber are tied at second order to the long wave motion. Both factors vary in phase with the long wave surface displacement.

Physically this result corresponds to a cyclic energy exchange between the two wave motions due to the flow of the long wave working against the radiation stress associated with the small scale motion (Phillips, 1969). As the short waves move from the trough to the crest of the long wave, the flux of energy is toward the short wave motion, and its energy density increases due to that and flow convergence. Traveling from long wave crest to trough, the short waves return energy

through the radiation stress, to the long wave motion and spread their energy due to flow divergence. The variation in short wave energy per unit surface area for two waves traveling in the same direction is given by

$$E = E_0 \left[ 1 + \frac{3}{2} a_2 k_2 \cos (k_2 x - \sigma_2 t) \right] , \quad (5-10)$$

where  $E_0$  is the energy density at the large scale wave zero crossing.

The action of radiation stress in the two-wave periodic model has led to speculation concerning the effect of introducing external fluxes of energy to the short wave. Phillips (1963) investigated the situation when short waves approaching the long wave crest from the forward face are forced to lose their energy through breaking, due to local steepening. At least some of the short wave steepening is a result of the convergent flow field induced by the long wave. Then as the remaining portion of the short wave proceeds down the rear face of the long wave, the short wave's steepness is reduced due to flow divergence. Since the short waves are so much smaller in that region, as a result of prior breaking, a net flow of energy results from the long wave to the short waves.

Longuet-Higgins and Stewart (1964) investigated the damping of the long wave energy, due to the flux of energy from the long wave through the radiation stress to capillary waves trapped on the front face of the long wave. The capillary waves have no phase velocity relative to the long wave, and their energy content exists in a steady state condition. The wind and straining input of energy to them is balanced by the viscous and breaking outflow of energy.

Longuet-Higgins (1969b) suggested that modulation of the short wave by the radiation stress effect could lead to short wave energy loss at

the long wave crest region. He assumed that the momentum lost there,  $\Delta m$ , would correspond to a long wave energy gain of  $\Delta m \cdot U_L$ , where  $U_L$  is the peak long wave orbital velocity.

Hasselmann (1971) realized that in a two scale situation there is coupling between the short and long waves due to a force arising from the interaction stress and due to a surface mass transfer arising from the gradient in the short wave mass flux. Hasselmann's interaction stress and Longuet-Higgins's radiation stress are similar; the radiation stress being related to the whole of the motion by the integration of the interaction stress over the water depth. It turns out that in a stationary, homogeneous wave field composed of two linear waves the average energy input to the long wave due to the interaction stress is almost exactly balanced by the short wave mass transport. The net result of the coupling is a slight long wave attenuation.

V.B. The Solution of the Two-Scale Wave Model by Direct Integration of the Wave Energy Equation

One may start with the equation for the conservation of slope energy of the small scale motion,  $\Psi(\omega; x, t)$ , and arrive at a result differing from that of Longuet-Higgins if wind input and decay are included. Equation (5-11) is derived from the hydrodynamic equations when two scales of motion are present.

$$\frac{\partial \Psi}{\partial t} + \frac{\partial(\Psi U_T)}{\partial x} + \gamma \Psi \frac{\partial U_o}{\partial x} = \beta_g \Psi - \beta_d \Psi \quad (5-11)$$

The two scales are considered to be sinusoidal with wavenumbers  $k_L$  and  $k_s$ . The variables in equation (5-11) are defined as

$\Psi(\omega; x, t)$  = short wave slope energy density,

$\beta_g$  = short wave growth rate due to wind input,

$\beta_d$  = short wave energy loss rate due to viscosity and turbulence,

$U_T$  = total horizontal short wave energy propagation velocity  
 $= U_o + U_d + c_{gs}$ ,

$U_d$  = wind induced surface drift,

$U_o$  = long wave orbital velocity,

$\gamma$  = Longuet-Higgins's strain factor,

and

$c_{gs}$  = short wave group velocity.

Transforming the above equation to coordinates moving with the long wave celerity,  $c_L$ , and assuming that  $\Psi$  is stationary, we have

$$\Psi \frac{\partial U_o}{\partial x} + (U_T - c_L) \frac{\partial \Psi}{\partial x} + \gamma \Psi \frac{\partial U_o}{\partial x} = -(\beta_g - \beta_d) \Psi \quad (5-12)$$

Rearranging (5-12) yields the integrable expression

$$\frac{d\Psi}{\Psi} = \left[ \frac{-(\beta_g - \beta_d)}{U_T - c_L} \right] dx - \left[ \frac{(1 + \gamma) \partial U_o}{(U_T - c_L) \partial x} \right] dx, \quad (5-13)$$

where  $U_o$  and  $U_T$  are known functions of  $x$ . The result of the integration is

$$\frac{\Psi_{x_2}}{\Psi_{x_k}} = \frac{(1 + U_L/K_1 \cos k_L x_1)^{1 + \gamma}}{(1 + U_L/K_1 \cos k_L x_2)^{1 + \gamma}} e^{\left[ \frac{-2(\beta_g - \beta_d)}{k_L K_1 \sqrt{1 - U_L^2/K_1^2}} (\phi_2 - \phi_1) \right]}, \quad (5-14)$$

where

$$K_1 = U_d + c_{gs} - c_L, \\ \phi_1 = \tan^{-1} \left[ \frac{\sqrt{1 - U_L^2/K_1^2}}{1 + U_L/K_1} \tan \frac{k_L x_1}{2} \right],$$

and

$$\phi_2 = \tan^{-1} \left[ \frac{\sqrt{1 - U_L^2/K_1^2}}{1 + U_L/K_1} \tan \frac{k_L x_2}{2} \right].$$

The first part of expression (5-14) yields a small sinusoidal perturbation of the energy as  $x$  changes. The exponential factor yields a continuous growth or decay in energy with  $x$ .  $K_1$  is always less than zero.  $|U_L/K_1|$  is less than one.  $\phi_1$  and  $\phi_2$  represent the phase points along the long wave profile, and by integration convention,  $\phi_2 > \phi_1$ . Therefore, at all positions along the long wave profile away from  $x_1$  a steady growth in short wave energy is found when  $\beta_g > \beta_d$ .

Equation (5-14) may be simplified in an interesting manner by referencing the intensity of the small waves to its value at the long wave zero crossing where  $\cos(k_L x_1) = 0$ , and assuming a short gravity wave where  $\gamma = 1/2$ . The result becomes

$$\frac{\Psi_{x_2}}{\Psi_{x_1}} = \left[ 1 - \frac{3 U_L}{2 U_d + c_{gs} - c_L} \cos k_L x_2 \right] e^{\frac{-2(\beta_g - \beta_d)}{k_L K_1 \sqrt{1 - U_L^2/K_1^2}} (\phi_2 - \phi_1)} \quad (5-15)$$

If growth and decay are ignored, and  $U_d$  and  $c_{gs}$  are neglected relative to  $c_L$ , the result reduces to that of Longuet-Higgins and Stewart (1960)

$$\frac{\Psi_{x_2}}{\Psi_{x_1}} = 1 + \frac{3 U_L}{2 c_L} \cos k_L x_2 \quad , \quad (5-16)$$

where  $\Psi_{x_1}$  is now the mean value of  $\Psi$ .

Equation (5-16) predicts an intensity variation that is in phase with the long wave horizontal orbital velocity,  $U_L \cos k_L x$ , but does not include any energy source effects. Equation (5-15) predicts a different sort of behavior that is controlled to a large extent by the expected value of the quantity  $(\beta_g - \beta_d)$ . If  $(\beta_g - \beta_d)$  was greater than zero, as one would expect, but much smaller than unity, the sinusoidal variation would dominate and local energy maxima would occur in phase with the long wave. This does not seem to be a useful result, as it is not consistent with observation. If  $(\beta_g - \beta_d)$  was a large quantity, growth would be the dominant factor and the short wave energy would predominantly grow with increasing  $x$ . This also is not consistent with observation.

It should be noted that for the typical test condition used in this study (a long wave of 10.0 cm height and 2.0 s period) the peak to peak variation in  $\Psi$  predicted by equation (5-15) is only 20% of the mean value. The measured variations have greater values for most of the frequencies considered.

V.C. The Solution of the Two-Scale Wave Model by Perturbation of the Wave Energy Equation

To obtain a strong, cyclic variation in  $\Psi$  one perhaps must assume that it is so, as Keller and Wright (1975) did, before the analysis. The growth term,  $(\beta_g - \beta_d)$ , then provides cyclic forcing to the problem, rather than continuous forcing. The latter leads to the unrealistic result of exponential growth over the large scale of motion.

A perturbation analysis may be pursued by considering the short wave energy conservation equation derived from hydrodynamic theory for two scales of motion. The equation may be conveniently considered in terms of wave slope intensity,  $\Psi(\omega; x, t)$ ,

$$\frac{\partial \Psi}{\partial t} + \frac{\partial}{\partial x} (\Psi U_T) + \gamma \Psi \frac{\partial U_0}{\partial x} = \beta_g \Psi - \beta_d \Psi \quad , \quad (5-17)$$

where the terms have the same meanings as in Section V.B. A complex notation is specified so that  $U_0$  becomes

$$U_0 = U_L e^{i(k_L x - \sigma_L t)} \quad . \quad (5-18)$$

The coordinate system is shifted to the frame moving at the long wave phase speed,  $c_L$ , and  $\Psi$  is considered steady but not homogeneous in the new frame. Equation (5-17) becomes

$$\Psi \frac{\partial U_0}{\partial x} + (U_T - c_L) \frac{\partial \Psi}{\partial x} + \gamma \Psi \frac{\partial U_0}{\partial x} = -(\beta_g - \beta_d) \Psi \quad . \quad (5-19)$$

All of the dependent variables except  $\Psi$  are known. Expanding  $\Psi$  in terms of a perturbation parameter defined by long wave slope,  $\epsilon$ , and assuming the mean spectrum,  $\Psi^{(0)}$ , to be a function of short wave frequency alone, we have

$$\Psi = \Psi^{(0)}(\omega) + \epsilon \Psi^{(1)}(\omega; x) + O[\epsilon^2] \quad . \quad (5-20)$$

We also assume that the change in  $\Psi$  about its mean is related to the long wave profile as

$$\Delta\Psi = \epsilon\Psi^{(1)} = \frac{U_L}{c_L} [h(\omega) + ig(\omega)] e^{ik_L x} \quad (5-21)$$

Perturbation of (5-19) and substitution for  $U_0$  yields

$$\begin{aligned} ik_L(1 + \gamma) \frac{U_L}{c_L} [\Psi^{(0)} + \epsilon\Psi^{(1)} + \dots] e^{ik_L x} + \frac{U_L}{c_L} \frac{\partial[\Psi^{(0)} + \epsilon\Psi^{(1)} + \dots]}{\partial x} e^{ik_L x} \\ + \left[ \frac{U_d + c_{gs}}{c_L} - 1 \right] \frac{\partial[\Psi^{(0)} + \epsilon\Psi^{(1)} + \dots]}{\partial x} \\ = \frac{-(\beta_g - \beta_d)}{c_L} [\Psi^{(0)} + \epsilon\Psi^{(1)} + \dots] \quad (5-22) \end{aligned}$$

The equation of order  $\epsilon$  is deduced from equation (5-22) to be

$$\begin{aligned} ik_L(1 + \gamma) \frac{U_L}{c_L} \Psi^{(0)} + \left[ \frac{c_{gs}^*}{c_L} - 1 \right] ik_L \frac{U_L}{c_L} [h(\omega) + ig(\omega)] \\ = \frac{-(\beta_g - \beta_d)}{c_L} \frac{U_L}{c_L} [h(\omega) + ig(\omega)] \quad (5-23) \end{aligned}$$

where

$$c_{gs}^* = c_{gs} + U_d \quad .$$

The real and imaginary component equations of (5-23) are solved to yield the components,  $g$  and  $h$ , of the second order spectrum. They are

$$h(\omega) = \frac{-\sigma_L^2(1 + \gamma) \Psi^{(0)} (c_{gs}^*/c_L - 1)}{\sigma_L^2 (c_{gs}^*/c_L - 1)^2 + (\beta_g - \beta_d)^2} \quad , \quad (5-24a)$$

and

$$g(\omega) = \frac{-\sigma_L(1 + \gamma) (\beta_g - \beta_d) \Psi^{(0)}}{\sigma_L^2 (c_{gs}^*/c_L - 1)^2 + (\beta_g - \beta_d)^2} \quad . \quad (5-24b)$$

Calculation of the modulation predicted by this method proceeded by the method described in the following section. The relative growth factor,  $(\beta_g - \beta_d)$ , is defined as  $K_H$ . It is seen from the equations (5-24a) and (5-24b) that for the predicted peaks to occur on the forward face of the long wave the value of  $K_H$  must be greater than zero. The predictions compared with data are only reasonable in a limited range of frequencies as will be discussed in the following chapters. It is therefore seen that additional considerations are needed to develop a theoretical prediction for acceptable comparisons with the modulation data.

V.D. The Modulation of Short Wave Spectra by Long Waves

To study the modulation of short waves by a coincident long wave during active generation, the concept of two-scale motion must be broadened beyond its use in earlier studies. The formulation should include the input to the system due to the air flow and allow for higher order energy exchanges within the wind generated spectrum of short waves.

Hasselmann (1968) first formulated the theory of weak wave interactions in terms of a Hamiltonian coordinate system. The problem formulation includes the Boltzmann transport equation and the Hamiltonian equations. The Boltzmann transport equation is commonly applied in the field of classical statistical mechanics to problems involving variations in a system from some steady state condition. See Appendix I for the derivation of the Boltzmann equation. For the problem of the short wave energy one can postulate a steady value existing over the large scales of space and time in all frequency bands. In addition one sees local variations from the steady value that are presumed to be cyclic in nature.

The Hamiltonian formulation of a problem is a general approach in which a process is specified through its momentum and generalized coordinates in phase space. The axes of phase space are designated as  $k_i$  and  $x_i$ , the wavenumber and generalized coordinate, respectively. The process is represented in phase space by a distribution function, the Hamiltonian. In this case the Hamiltonian is the wave slope spectral density function. The Boltzmann transport equation describes the evolution of the process along a path in phase space. In terms of waves the path in phase space along which the process progresses in time is

the path along which a wave packet moves with its prescribed group velocity,  $c_g$  (Dorrestein, 1960). Along this line the wave dispersion relation holds and the conservation of waves equation is valid.

For a distribution function of the form  $\Psi(k;x,t)$ , the Boltzmann equation can be written

$$\frac{D\Psi}{Dt} = \frac{\partial\Psi}{\partial t} \Big|_{k,x} + \frac{\partial x}{\partial t} \frac{\partial\Psi}{\partial x} \Big|_{k,t} + \frac{\partial k}{\partial t} \frac{\partial\Psi}{\partial k} \Big|_{x,t} = S_0, \quad (5-25)$$

where  $S_0$  represents the total effect of energy sources and sinks. However, to apply the statistical mechanics concept to the present results, it is necessary to write equation (5-25) in a form suitable for a function that is a direct function of short wave frequency,  $\omega$ . That is,  $\Psi[\omega(k_s,x,t);x,t]$ , the short wave slope spectral density is the variable of interest. Consequently the derivatives in equation (5-25) are transformed by the relationships

$$\frac{\partial\Psi}{\partial t} \Big|_{k_s,x} = \frac{\partial\Psi}{\partial t} \Big|_{\omega,x} + \frac{\partial\Psi}{\partial\omega} \frac{\partial\omega}{\partial t} \Big|_{k_s,x}, \quad (5-26)$$

$$\frac{\partial\Psi}{\partial x} \Big|_{k_s,t} = \frac{\partial\Psi}{\partial x} \Big|_{\omega,t} + \frac{\partial\Psi}{\partial\omega} \frac{\partial\omega}{\partial x} \Big|_{k_s,t}, \quad (5-27)$$

and

$$\frac{\partial\Psi}{\partial k_s} \Big|_{x,t} = \frac{\partial\Psi}{\partial\omega} \frac{\partial\omega}{\partial k_s} \Big|_{x,t}, \quad (5-28)$$

where  $\omega$  and  $k_s$  are short wave frequency and wavenumber, respectively.

Upon substitution equation (5-25) becomes

$$\begin{aligned}
\frac{D\Psi}{Dt} = & \left. \frac{\partial\Psi}{\partial t} \right|_{\omega, x} + \left. \frac{\partial\Psi}{\partial\omega} \right|_{x, t} \frac{\partial\omega}{\partial t} \Big|_{k_s, x} + \left. \frac{\partial x}{\partial t} \frac{\partial\Psi}{\partial x} \right|_{\omega, t} + \left. \frac{\partial x}{\partial t} \frac{\partial\Psi}{\partial\omega} \right|_{x, t} \frac{\partial\omega}{\partial x} \Big|_{k_s, t} \\
& + \left. \frac{\partial k_s}{\partial t} \frac{\partial\Psi}{\partial\omega} \right|_{x, t} \frac{\partial\omega}{\partial k_s} \Big|_{x, t} = S_0 . \quad (5-29)
\end{aligned}$$

For conservation of waves it is known that relation (5-30) holds between short wave wavenumber and radian frequency. That is,

$$\frac{\partial k_s}{\partial t} = - \frac{\partial\omega}{\partial x} . \quad (5-30)$$

In the Hamiltonian formulation  $\partial x/\partial t$  is the velocity of the wave energy flow. It equals the group velocity of the wave packet plus the advection velocity associated with any current underlying the wave. From the Hamiltonian formulation (see Appendix I) it is known that the energy propagation velocity,  $c_{gs}$ , is given as

$$c_{gs} = \frac{\partial\omega}{\partial k_s} . \quad (5-31)$$

Assuming that the local short wave frequency is related to wavenumber and underlying current,  $U$ , as in (5-32), it is clear than  $\partial x/\partial t = \partial\omega/\partial k_s$ . In one dimension the frequency is written as

$$\omega(k_s, x, t) = \omega_0(k_s) + k_s U(x, t) , \quad (5-32)$$

where  $\omega_0$  is the free wave frequency, we have

$$\frac{\partial\omega}{\partial k_s} = \frac{\partial\omega_0}{\partial k_s} + U = (c_{g0})_s + U = \frac{\partial x}{\partial t} . \quad (5-33)$$

Using (5-33) and (5-30) in (5-29) yields the Boltzmann transport equation,

$$\left. \frac{\partial \Psi}{\partial t} \right|_{\omega, x} + \left. \frac{\partial \Psi}{\partial \omega} \right|_{x, t} \frac{\partial \omega}{\partial t} \Big|_{k_s, x} + c_{gs} \left. \frac{\partial \Psi}{\partial x} \right|_{\omega, t} = S_0 \quad , \quad (5-34)$$

in terms of the slope spectral density function,  $\Psi(\omega; x, t)$ .

The three source terms to be considered are; atmospheric input, short wave interactions, and Lonquet-Higgins type short wave - long wave coupling. For the atmospheric input term it is assumed that the input of energy results in exponential growth of the wave spectrum. Under this assumption the rate term is proportional to the spectral value as

$$\text{Input Flux} = \beta \Psi \quad . \quad (5-35)$$

The wave-wave interaction for now is written as a function of wavenumber and spectral value as

$$\text{Wave-Wave Interaction} = H(\Psi, k_s) \quad . \quad (5-36)$$

The straining of a particular portion of the spectrum by the long wave is proportional to its own value through the radiation stress term, which takes the form for deep water waves of

$$\begin{aligned} \text{Energy Flux Due} \\ \text{To Straining} \end{aligned} = -\gamma(k_s) \Psi (\partial U_o / \partial x) \quad , \quad (5-37)$$

where  $\gamma(k_s)$  is given by Lonquet-Higgins (1964) as

$$\gamma(k_s) = \frac{1 + (3Tk_s^2 / \rho_w g)}{2[1 + (Tk_s^2 / \rho_w g)]} \quad . \quad (5-38)$$

The term  $\partial U_o / \partial x$  is the gradient of the current, and T is the surface tension force per unit length. Equation (5-34) becomes

$$\left. \frac{\partial \Psi}{\partial t} \right|_{\omega, x} + \left. \frac{\partial \Psi}{\partial \omega} \right|_{x, t} \frac{\partial \omega}{\partial t} \Big|_{k_s, x} + c_{gs} \left. \frac{\partial \Psi}{\partial x} \right|_{\omega, t} = \beta \Psi - \gamma \Psi \frac{\partial U_o}{\partial x} + H(\Psi, k_s) \quad . \quad (5-39)$$

As already noted in equation (5-32), the dispersion relation is modified by the underlying current, which is the sum of the wind drift value,  $U_d$ , and the local long wave horizontal orbital velocity,  $U_o$ . To find a substitute for the  $\partial\omega/\partial t$  term in (5-39), the dispersion relation is used in the form

$$\omega(k_s, x, t) = k_s c_s + k_s [U_o(x, t) + U_d] \quad ,$$

to yield

$$\left. \frac{\partial\omega}{\partial t} \right|_{k_s, x} = k_s \frac{\partial c_s}{\partial t} + k_s \frac{\partial U_o}{\partial t} \quad , \quad (5-40)$$

For  $U_o$  we use the relation

$$U_o(x, t) = U_L e^{i(k_L x - \sigma_L t)} + * \quad , \quad (5-41)$$

where the star indicates the complex conjugate. For the phase speed,  $c_s$ , which includes the effect of surface tension and the apparent modification to the gravitational acceleration by the vertical acceleration of the long wave surface we use

$$c_s = \left[ \frac{g - \sigma_L U_o}{k_s} + \frac{Tk_s}{\rho_w} \right]^{1/2} \quad . \quad (5-42)$$

From this expression we obtain

$$\frac{\partial c_s}{\partial t} = - \frac{\sigma_L}{2k_s c_s} \frac{\partial U_o}{\partial t} \quad . \quad (5-43)$$

Since  $\sigma_L/2k_s c_s \ll 1$ , equation (5-40) becomes

$$\left. \frac{\partial\omega}{\partial t} \right|_{k_s, x} \approx k_s \frac{\partial U_o}{\partial t} \quad . \quad (5-44)$$

The Boltzmann equation, (5-39), is further modified by the substitution of equation (5-44), the introduction of a coordinate system moving with the long wave celerity,  $c_L$ , and the assumption that the short wave slope spectral density exists in a steady state condition. The result is

$$k_s \frac{\partial(U_o - c_L)}{\partial t} \bigg|_{k_s, x} \frac{\partial \Psi}{\partial \omega} \bigg|_{x, t} + (c_{gs} - c_L) \frac{\partial \Psi}{\partial x} \bigg|_{\omega, t} = \beta \Psi - \gamma \Psi \frac{\partial(U_o - c_L)}{\partial x} + H(\Psi, k_s) \quad (5-45)$$

The equation is then perturbed in the parameter,  $\epsilon = U_L/c_L = a_L k_L$ . The dependent variable expansions are

$$\Psi(\omega; x, t) = \Psi^{(0)}(\omega) + \epsilon \Psi^{(1)}(\omega; x, t) + O(\epsilon^2) \quad ,$$

and

$$H(\Psi, k_s) = H^{(0)} + \epsilon H^{(1)}(\Psi^{(0)}, k_s) + O(\epsilon^2) \quad ,$$

so that the equation (5-45) becomes

$$\begin{aligned} & k_s \frac{\partial U_o}{\partial t} \bigg|_{k_s, x} \frac{\partial(\Psi^{(0)} + \epsilon \Psi^{(1)} + \dots)}{\partial \omega} \bigg|_{x, t} \\ & + (c_{gs} - c_L) \frac{\partial(\Psi^{(0)} + \epsilon \Psi^{(1)} + \dots)}{\partial x} \bigg|_{\omega, t} \\ & = \beta(\Psi^{(0)} + \epsilon \Psi^{(1)} + \dots) - \gamma(\Psi^{(0)} + \epsilon \Psi^{(1)} + \dots) \frac{\partial U_o}{\partial x} \\ & \quad + (H^{(0)} + \epsilon H^{(1)} + \dots) \quad . \end{aligned} \quad (5-46)$$

The component equation in (5-46) of order,  $\epsilon^{(0)}$ , simply makes the statement that if the process is steady state the energy flowing into a component of the wave system from the wind is balanced by the wave-wave energy outflow. That is,

$$\beta \Psi^{(0)} = H^{(0)} ,$$

where  $H^{(0)}$  is assumed to be that part of  $H$  representing nonlinear dissipative mechanisms.  $H^{(0)}$  represents the equilibrium state of the functional,  $H$ .

The component equation of order,  $\epsilon^{(1)}$ , contains the short wave - long wave coupling. Equation (5-46) at first order in  $\epsilon$  becomes

$$\frac{k_s}{c_L} \frac{\partial U_o}{\partial t} \frac{\partial \Psi^{(0)}}{\partial \omega} + \xi \left[ \frac{c_{gs}}{c_L} - 1 \right] \frac{\partial \Psi^{(1)}}{\partial x} = \epsilon \frac{\beta}{c_L} \Psi^{(1)} - \frac{\gamma \Psi^{(0)}}{c_L} \frac{\partial U_o}{\partial x} + \epsilon \int_{k_s} I^{(0)}(\Psi^{(0)}, k_s, k'_s) \Psi^{(1)}(k'_s) dk'_s . \quad (5-47)$$

See Appendix II for the origin of the integral representation of the nonlinear interaction appearing in equation (5-47). As the goal of this study is to investigate the cyclic short wave slope intensity changes with respect to the long wave, it seems reasonable to express the spectral perturbation,  $\Psi^{(1)}$ , as a direct function of the long wave profile,  $\eta_L = a_L e^{ik_L x} + *$  (Keller and Wright, 1975). The motion becomes stationary in the mean, since the frame moves with the long wave celerity. The first order slope intensity spectrum,  $\Psi^{(1)}$ , is written in terms of spectral components in phase and in quadrature with the long wave as

$$\Psi^{(1)}(\omega, x) = [h(\omega) + ig(\omega)] e^{ik_L x} + * . \quad (5-48)$$

The integral term in equation (5-47) is related to the spectral perturbation by the relaxation approximation discussed in Appendix II. The result of the approximation is given as

$$\int_{k_s} I^{(0)}(\psi^{(0)}, k_s, k'_s) \psi^{(1)}(k'_s, t) dk'_s = -(\beta + \beta_r) \psi^{(1)}(k_s, t) \quad , \quad (5-49)$$

where  $\beta_r$  is the relaxation rate coefficient. Substitution of  $U_0$ ,  $\psi^{(1)}$ , their derivatives, and (5-49) into (5-47) yields (5-50) after cancellation of  $\epsilon$ ,  $U_L/c_L$ , and the exponential term. When the complex conjugate equation is disregarded we have

$$\begin{aligned} & -ik_s \sigma_L \frac{\partial \psi^{(0)}}{\partial \omega} + ik_L \left[ \frac{c_{gs}}{c_L} - 1 \right] [h(\omega) + ig(\omega)] \\ & = \frac{\beta}{c_L} [h(\omega) + ig(\omega)] - i\gamma k_L \psi^{(0)} - \frac{(\beta + \beta_r)}{c_L} [h(\omega) + ig(\omega)] \quad . \quad (5-50) \end{aligned}$$

This equation can be separated into its real and imaginary parts as

$$\text{RE:} \quad -k_L \left[ \frac{c_{gs}}{c_L} - 1 \right] g(\omega) = \frac{\beta}{c_L} h(\omega) - \frac{(\beta + \beta_r)}{c_L} h(\omega) \quad ,$$

and

$$\begin{aligned} \text{IM:} \quad & -k_s \sigma_L \frac{\partial \psi^{(0)}}{\partial \omega} + k_L \left[ \frac{c_{gs}}{c_L} - 1 \right] h(\omega) \\ & = \frac{\beta}{c_L} g(\omega) - \gamma k_L \psi^{(0)} - \frac{(\beta + \beta_r)}{c_L} g(\omega) \quad . \end{aligned}$$

The real and imaginary equations are solved simultaneously for the two components of  $\psi^{(1)}$  to yield

$$\frac{h(\omega)}{\psi^{(0)}} = \frac{-[1 - (c_{gs}/c_L)] K^2 [(k_s c_L / \psi^{(0)}) (\partial \psi^{(0)} / \partial \omega) - \gamma]}{[1 - (c_{gs}/c_L)]^2 K^2 + 1} \quad , \quad (5-51)$$

and

$$\frac{g(\omega)}{\psi^{(0)}} = \frac{K [(k_s c_L / \psi^{(0)}) (\partial \psi^{(0)} / \partial \omega) - \gamma]}{[1 - (c_{gs}/c_L)]^2 K^2 + 1} \quad , \quad (5-52)$$

where  $K \equiv \sigma_L / \beta_r$ . This solution is similar to that of Keller and Wright (1975), the central difference being the presence of the derivative of  $\psi(0)$  with respect to  $\omega$  rather than  $k_s$ .

## CHAPTER VI

### COMPARISON BETWEEN EXPERIMENTAL AND THEORETICAL RESULTS

#### VI.A. Determination of Spectral Modulation by the Modeling Methods

The predictions of the modulations are formulated from the two analyses of Chapter V in the following way. The variation in the slope spectral density,  $\Psi(\omega; x, t)$ , may be represented as

$$\Psi(\omega; x, t) = \Psi^{(0)}(\omega) + \Delta\Psi(\omega; x, t) \quad . \quad (6-1)$$

Referring to the perturbation analyses of Chapter V, and realizing that the long wave profile may be written as a cosine function since the surface is a real quantity; the spectral density function may be represented by

$$\Psi(\omega; x, t) = \Psi^{(0)} [1 + m \cos (k_L x + \phi)] \quad , \quad (6-2)$$

where the approximation is correct through the first order in long wave slope.

The quantity,  $m\Psi^{(0)}$ , represents the amplitude of the excursions of the spectral density away from its total mean value,  $\Psi^{(0)}(\omega)$ . The coefficient,  $m$ , is defined as

$$m \equiv \frac{U_L}{c_L} \left| \frac{h(\omega)}{\Psi^{(0)}} + \frac{ig(\omega)}{\Psi^{(0)}} \right| = \frac{U_L}{c_L} \left[ \left( \frac{h(\omega)}{\Psi^{(0)}} \right)^2 + \left( \frac{g(\omega)}{\Psi^{(0)}} \right)^2 \right]^{1/2} \quad , \quad (6-3)$$

where  $i = \sqrt{-1}$  and  $h(\omega)$  and  $g(\omega)$  are defined by equation (5-24) for the wave energy equation analysis and equations (5-51) and (5-52) for the

Hamiltonian analysis. Calculation of  $h(\omega)$  and  $g(\omega)$  yields predicted values for slope intensity excursions.

The maximum intensity excursion, calculated or measured, is located relative to the crest of the long wave by a phase angle,  $\phi$ . The phase angles resulting from the modulation calculations are given by

$$\phi = \tan^{-1} \left[ \frac{g(\omega)}{h(\omega)} \right] . \quad (6-4)$$

The measured value of phase results from the analysis process described in section III.F. The intensity calculations are located within data segments that are each one-eighth the length of a long wave cycle.

Therefore, the maximum uncertainty in the phase measurement is  $\pm 22.5^\circ$ .

The modeling methods of Chapter V require the first order spectral quantities,  $\Psi^{(0)}$  and  $\partial\Psi^{(0)}/\partial\omega$ , located at the frequency corresponding to the mean short wave frequency. This frequency is found to be the sum of the selected free wave frequency and the shift in frequency due to the homogeneous surface drift current. The mean frequencies are

$$\omega_{\text{mean}}(k_s) = \overline{\omega_0 + k_s(U_o(x) + U_d)} = \omega_0 + k_s U_d , \quad (6-5)$$

where the overbar implies averaging over one wave period and

$\omega_0$  = free wave frequency (short wave),

$k_s$  = short wave wavenumber,

$U_o(x)$  = long wave horizontal orbital velocity,

and

$U_d$  = wind induced surface drift.

The first order spectral quantities are obtained from the total mean slope spectral density calculations by entering the tabulated spectral results with the frequencies calculated by equation (6-5).

The analysis scheme described in section III.F. looks at the data in one long wave period and calculates slope spectral intensity at eight phase locations along the long wave profile. This gives an estimate of how the intensity within a variance element changes as a function of phase location along the profile. The present analysis, for which the details are given below, is intended to estimate with high resolution and stability the first order slope spectral intensity (total average spectrum) of the complete wave field for a given wind condition.

The slope data signal is operated on in segments of 4064 points, representing approximately five long wave periods in time. Every segment, but the first, contains 2032 new data points concatenated with the final 2032 points from the previous segment. The initial and final 10% of each segment is shaped by the application of a cosine bell. The central 3252 points are passed to the FFT routine unaltered. Thirty-two additional zero valued points are appended to each segment before Fourier transformation, so the resultant spectral resolution is 0.098 Hz on the frequency axis. The data shaping through the application of the cosine bell reduces the energy content of each data segment. The energy content is restored, as described in section III.F., by division of the spectral values by the mean square value of the sampling window. The 4064 point sampling window described here has a mean square value of 0.938. First order spectra are calculated for 57 segments in the manner described above and averaged together to yield a spectral estimate of approximately 93 equivalent degrees of freedom according to Welch's (1967) method.

The parameters from the first order spectra,  $\psi^{(0)}$ , and  $\partial\psi^{(0)}/\partial\omega$ , required in the calculations of the energy excursions are obtained by the following procedures. The value of  $\psi^{(0)}$  is calculated as the

average of about six of the values from the first order spectrum at and adjacent to the selected mean short wave frequency. The spectral slope,  $\partial\psi^{(0)}/\partial\omega$ , is calculated over a frequency band of approximately 2.0 Hz. The point of interest is at the center of the band and the endpoints of each band are represented by the average of six points at each end of the band.

As a routine check of the spectral computations described above and those described in section III.F., the first order values calculated by the method above are compared to the spectra computed by averaging the eight phase averaged results obtained for the earlier analysis. A typical comparison is shown below each portion of the figure for two sets of test conditions in Figure 37.

## VI.B. Model Based on the Wave Energy Equation

The perturbation model based on the wave energy equation discussed in section V.C., yields results like those compared to data in Figures 35 and 36 for wind speeds of 5.6 and 8.3 m/s, respectively. The modulation value of the spectrum is defined to be one-half of the peak to peak energy excursion found experimentally after removal of the frequency modulation. These values are represented by the circled data points. The calculated energy excursions are shown for two different values of  $K_H$ , the relative growth factor. The figures show agreement between data and theory only for a very narrow frequency range around 9.5 Hz. The phase angles associated with each value of  $K_H$  are also shown. The values of  $K_H$  were chosen to yield values of amplitude modulation and phase that were within the realm of the data.

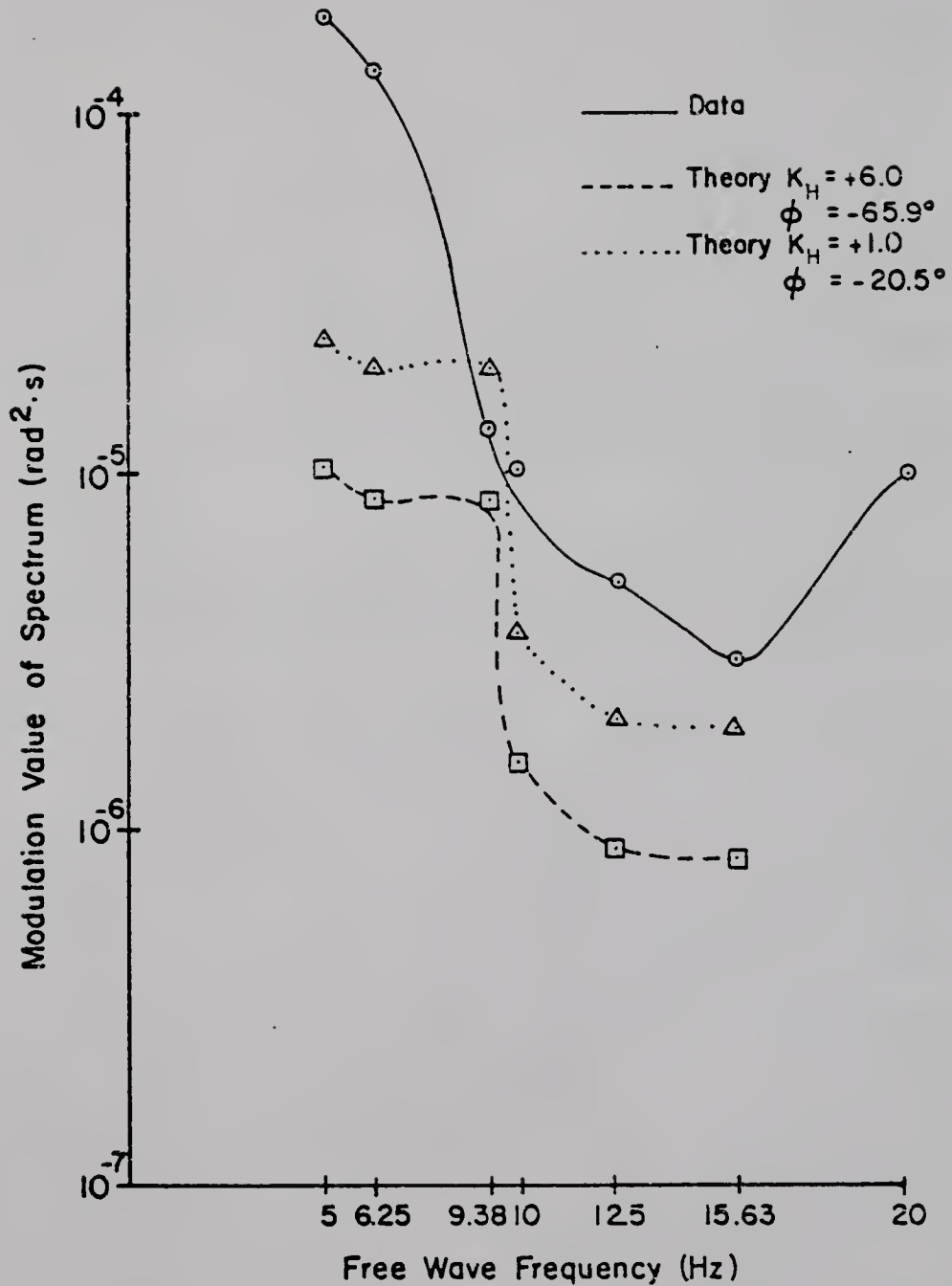


Figure 35. Comparison for experiment E3 and test T16 between the experimental modulation results and the theoretical prediction based on the hydrodynamic energy equation with the cyclic perturbation. Reference wind speed = 5.6 m/s. Long wave:  $T = 2.0$  s,  $H = 10.0$  cm.

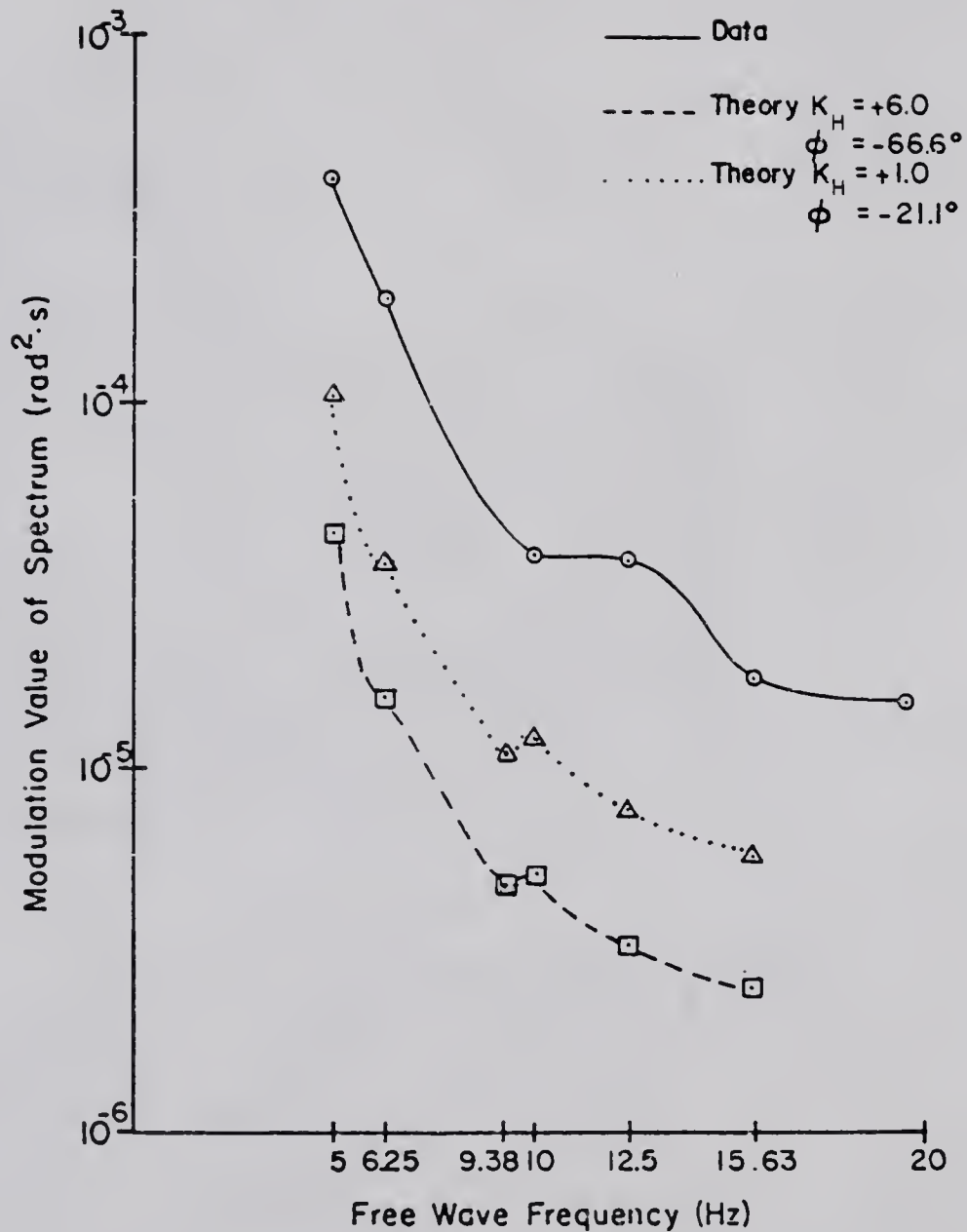


Figure 36. Comparison for experiment E3 and test T19 between the experimental modulation results and the theoretical prediction based on the hydrodynamic energy equation with the cyclic perturbation. Reference wind speed = 8.3 m/s. Long wave:  $T = 2.0$  s,  $H = 10.0$  cm.

### VI.C. Model Based on the Hamiltonian Formulation

The analysis based on the Hamiltonian formulation was discussed in section V.D. It yields results of the form shown in Figure 37. Figure 37 displays the amplitude, phase, and shape of the modulation of the short wave spectral density for the variance element centered at the 9.38 Hz free wave for the two wind speeds of 4.9 m/s and 5.6 m/s. The measured modulations are based on the phase averaging routine. For E3T15 and E3T16 the total mean spectral values come from five point averages around the 9.38 Hz free wave convected by surface drift to 15.07 and 15.85 Hz, respectively. The primary contribution to these data is from modulation of the nature of an amplitude modulation, the frequency modulation having been removed. Note that the experimentally determined modulation values do not produce a curve that has the shape of a sinusoid. The predicted modulations shown were calculated by using K values that yield good fits to the amplitudes of the energy excursions. The figure shows that the phase angles between the long wave profile and the predicted modulation curves are somewhat smaller than the experimentally determined values. The predicted phase angles could be increased by reducing the values of K used in the calculations. However, this would sacrifice good amplitude agreement for only a small improvement in phase prediction. For example, if K in the upper portion of Figure 37 is reduced from 0.2 to 0.1 the phase increases only from  $80^{\circ}$  to  $85^{\circ}$ , while the energy excursion would be reduced by 50%. If K in the lower portion of the figure were reduced from 0.3 to 0.2, the phase would only increase from  $75^{\circ}$  to  $80^{\circ}$ , while the energy excursion would be reduced by 29%. The major disagreement appearing between the experimental and predicted modulations result from the use of a sinusoid to

approximate the true modulation. All things considered, Figure 37 shows good analytical agreement with the experimental values.

The results shown in Figures 38 through 52 display in condensed form all of the experimental amplitude modulations of this study and comparisons with the analytical results based on the Hamiltonian formulation. In these figures the frequency modulation has been removed. Figures 38 through 45 illustrate the amplitude modulation of the short wave slope spectral densities as a function of the free wave frequency. The figures are divided into three portions, the value of  $K$  chosen for the computation, which represents the relaxation rate, the phase angle by which the modulation peak leads the long wave crest, and the modulation amplitude of the slope spectral density. Each figure represents the results for a given reference wind speed. The value of  $K$  was allowed to vary for most of the test situations in order to determine the range that was necessary to make the prediction conform to the experimental amplitude modulation of the slope spectral density reasonably well, without forcing the corresponding phase prediction to unreasonable values. In general the amplitude modulation values could be predicted exactly, while the predicted phase angles were smaller than the experimental values. The dotted lines of these figures refer to calculations made with a variable  $K$ , the values of  $K$  being shown in the upper portion of the figures. Most of the data can be fit well with  $K$  values ranging from 0.2 to 2.0, which corresponds to relaxation coefficient values of 15.7 and 1.57, respectively. The data point at a 5.00 Hz free wave frequency was consistently poorly predicted.

The modulation prediction values corresponding to the dashed lines of Figures 38 through 45 were calculated based on a constant value of  $K$ , which was chosen to be 0.5. The value was selected as a logical midpoint

based on the range of K needed to fit the data. After the fixed value of K was decided on, the curves for variable K were no longer drawn (as in Figures 43 through 45). When K is held constant the phase angle does not vary. The predictions of the modulation amplitude are not as close to the data as for the variable K case. Generally, the prediction occupies the same region as the data and exhibits the same trend, but does not agree as well in amplitude or phase as the variable K curve.

The peaks in the constant K prediction curves of Figures 38 through 45 seem to be directly related to the formation of "plateau" regions in the spectra of Figures 26 through 28. At low wind speeds the first order spectral shape drops off gently as frequency increases. As the wind speed increases, one of the first spectral changes noticed is the formation of a plateau in the region from 2.0 to 10.0 Hz. The slope spectral density becomes more uniform within that frequency band. The relatively large increase in intensity in this band leads to the development of a steep edge on the high frequency end of the plateau. This condition leads to the calculation of relatively large predicted intensity excursions in the 9.0 to 10.0 Hz free wave frequency region. Then with further increases in wind speed the plateau becomes narrower and the large spectral slope values occur at lower frequencies, causing the peak in the modulation prediction to shift to lower frequencies. In test E3T16 at a reference wind speed of 5.6 m/s a second plateau region begins to form. Again the relatively large increase in spectral level leads to larger spectral slopes, and a second peak in the modulation prediction in the neighborhood of the 15.63 Hz free wave. At wind speeds above 7.2 m/s the regions of the spectra that were lagging behind the plateau regions begin to rise and fill in the spectral shape to a

smooth drop off toward the higher frequencies. This has the effect of smoothing out the modulation prediction curve.

The predicted modulations for the reference wind speed of 9.2 m/s shown in Figure 44 do not agree well with the data and can serve well to illustrate a weakness in the prediction procedure. The original prediction curve, represented by the dashed line, is based on  $K = 0.5$  and lies concave upward in the figure. The first order spectral parameters required for its construction were calculated by computer from the first order spectrum by the usual method. That is, for the frequency under consideration the spectral value was taken as the seven point average of the seven values located about that frequency, and the spectral slope is the spectral difference calculated by seven point averages centered 0.98 Hz on either side of the frequency of interest divided by the change in radian frequency between these two points. The second prediction curve, represented by a dashed-dotted line, is based on  $K = 0.5$  and lies concave downward in the figure. The difference between the curves is that the second prediction is based on a spectral slope calculated by five point averages centered 0.59 Hz on either side of the frequency of interest. The prediction method is clearly very sensitive to the value of spectral slope, and thereby to the method of its calculation.

Figures 46 through 52 compare the measured and calculated modulation amplitudes as a function of wind speed. Each figure applies to a selected free wave frequency. The dotted lines refer to the calculation for which  $K$  was allowed to assume a new value for any selected frequency and wind speed. The results are displayed for those tests for which they were calculated. These figures show in another form the accuracy

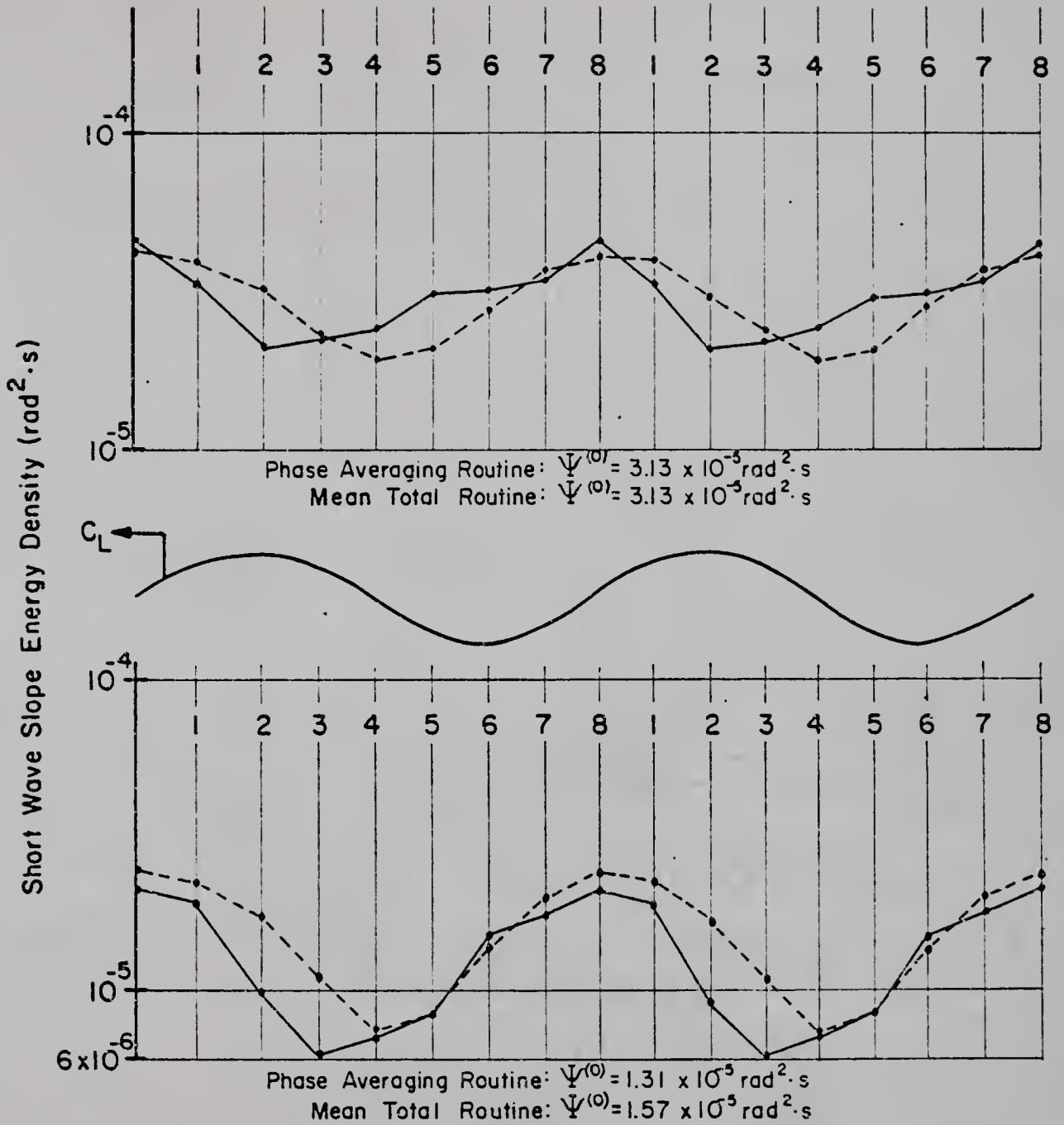


Figure 37. Eight point amplitude modulation comparison.

- Experimental values.
- - - Spectral prediction for experiment E3. Long wave:  
 $T = 2.0 \text{ s}$ ,  $H = 10.0 \text{ cm}$ . The free short wave  
 frequency is  $9.38 \text{ Hz}$ . Upper portion of figure is  
 for test T16. Wind speed =  $5.6 \text{ m/s}$ .  $K = 0.2$ .  
 Lower portion of figure is for test T15. Wind  
 speed =  $4.9 \text{ m/s}$ .  $K = 0.3$ .

Figure 38. Magnitudes and phases of the short wave slope energy amplitude modulation for the conditions of experiment E3 and test T14. Reference wind speed = 4.4 m/s. Long wave:  $T = 2.0$  s,  $H = 10.0$  cm.

- Experimentally determined values.
- - - - Spectral prediction with  $K = 0.5$ .
- . . . . Spectral prediction with the values of  $K$  indicated in the uppermost part of the figure.

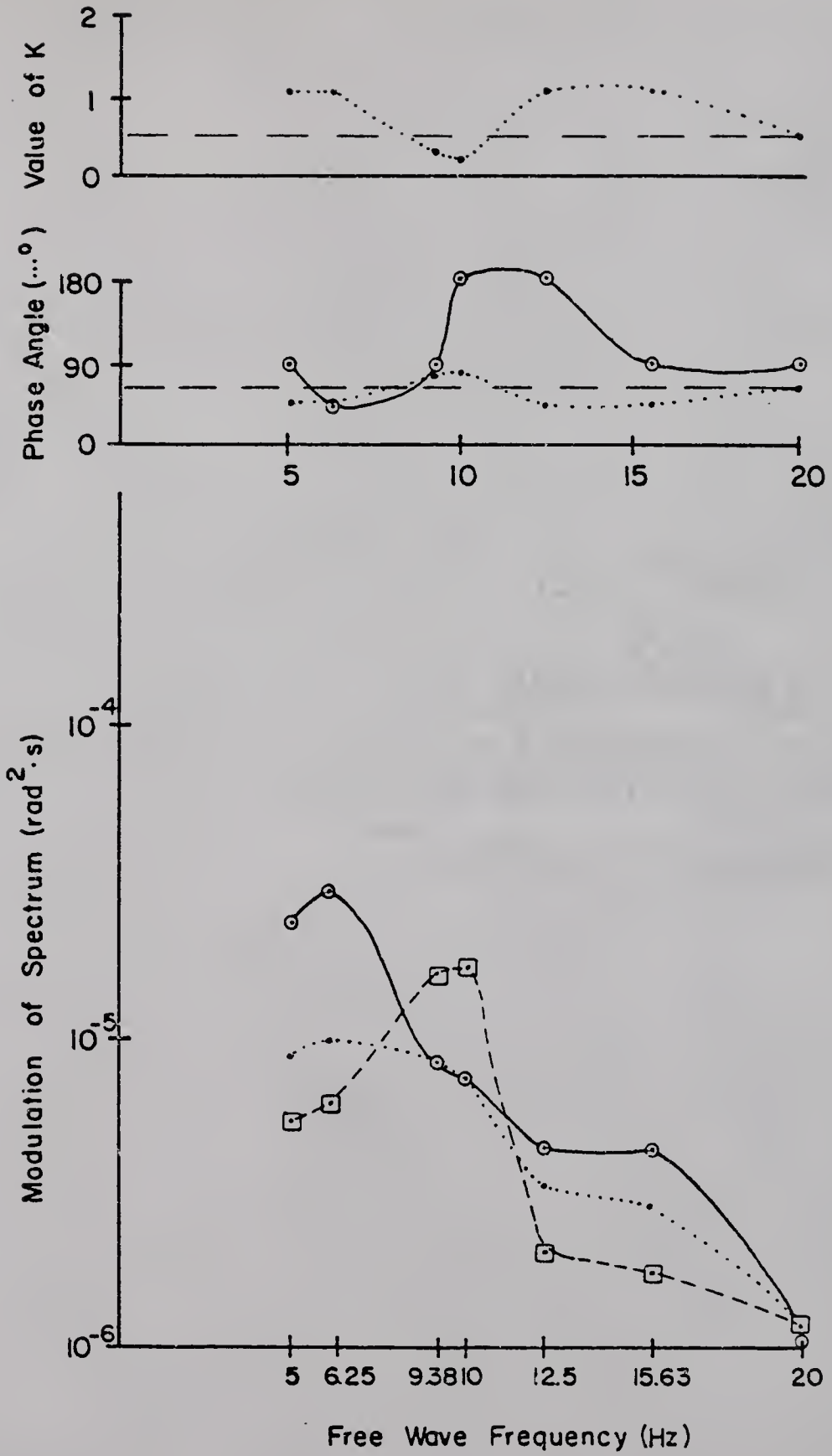


Figure 39. Magnitudes and phases of the short wave slope energy amplitude modulation for the conditions of experiment E3 and test T15. Reference wind speed = 4.9 m/s. Long wave:  $T = 2.0$  s,  $H = 10.0$  cm.

- Experimentally determined values.
- - - - Spectral prediction with  $K = 0.5$ .
- . . . . Spectral prediction with the values of  $K$  indicated in the uppermost part of the figure.

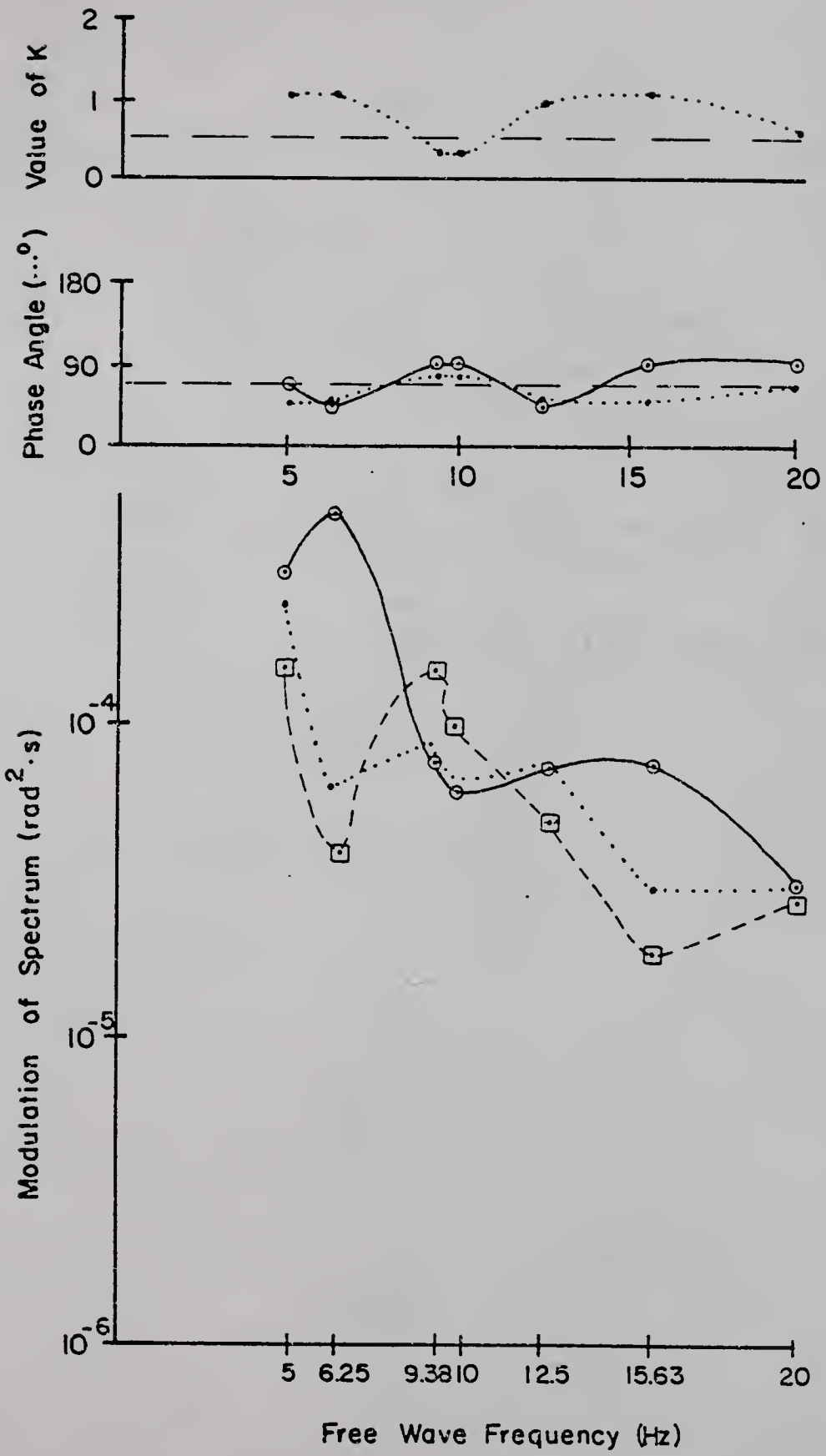


Figure 40. Magnitudes and phases of the short wave slope energy amplitude modulation for the conditions of experiment E3 and test T16. Reference wind speed = 5.6 m/s.  
Long wave:  $T = 2.0$  s,  $H = 10.0$  cm.

- Experimentally determined values.
- - - - Spectral prediction with  $K = 0.5$ .
- . . . . Spectral prediction with the values of  $K$  indicated in the uppermost part of the figure.

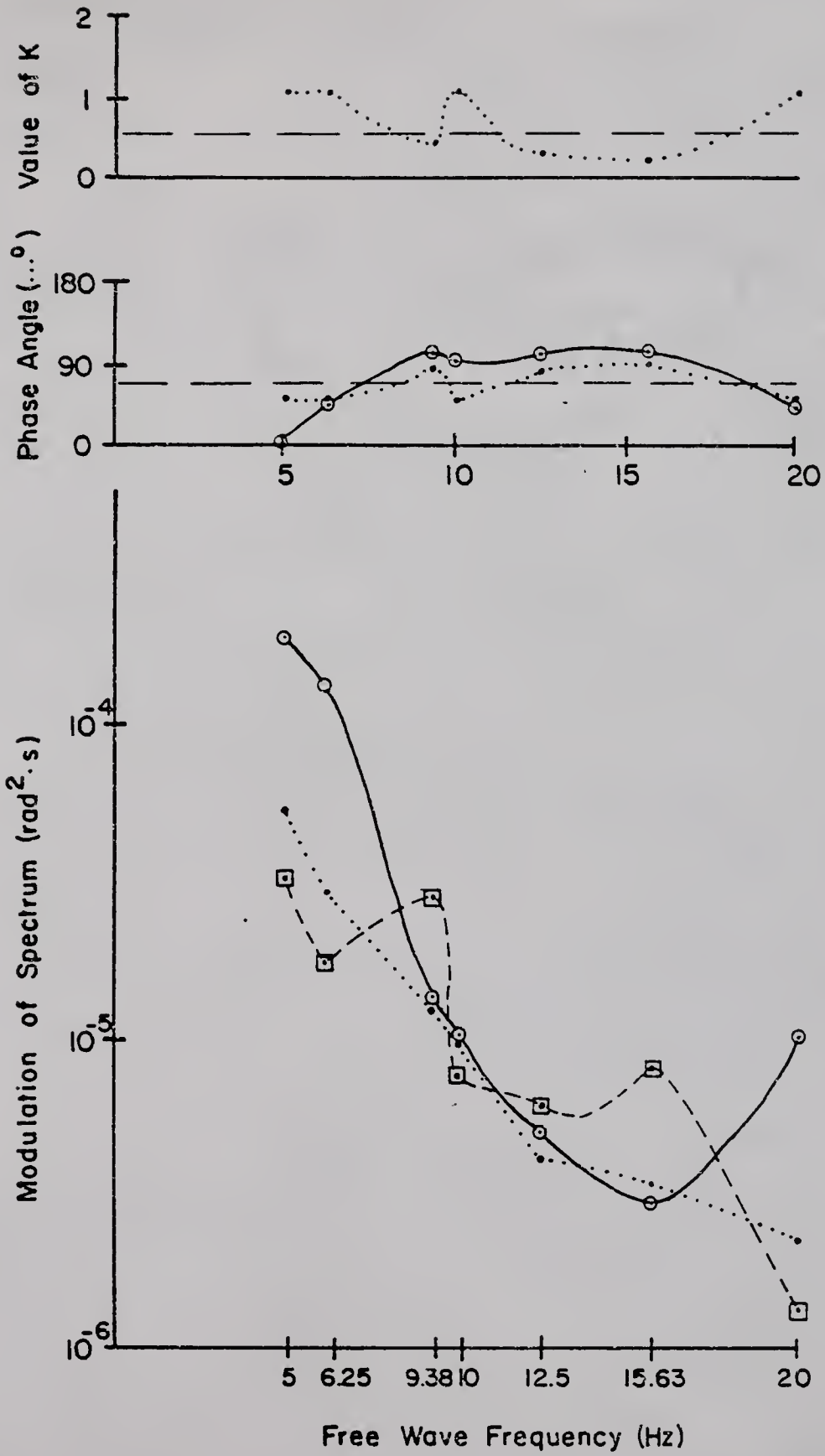


Figure 41. Magnitudes and phases of the short wave slope energy amplitude modulation for the conditions of experiment E3 and test T17. Reference wind speed = 5.9 m/s. Long wave:  $T = 2.0$  s,  $H = 10.0$  cm.

- Experimentally determined values.
- - - - Spectral prediction with  $K = 0.5$ .
- . . . . Spectral prediction with the values of  $K$  indicated in the uppermost part of the figure.

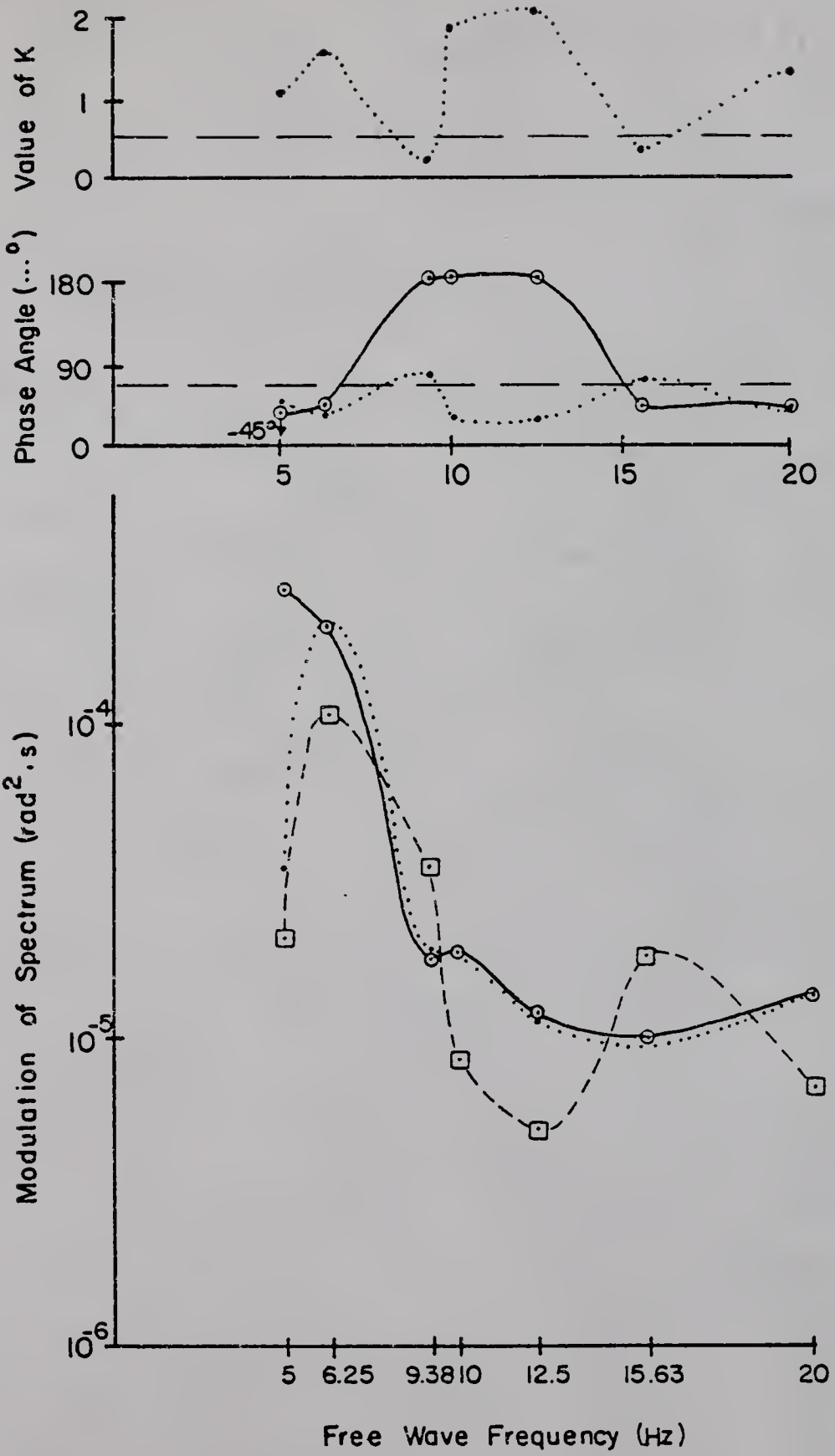


Figure 42. Magnitudes and phases of the short wave slope energy amplitude modulation for the conditions of experiment E3 and test T18. Reference wind speed = 7.2 m/s. Long wave: T = 2.0 s, H = 10.0 cm.

- Experimentally determined values.
- - - - Spectral prediction with K = 0.5.
- . . . . Spectral prediction with the values of K indicated in the uppermost part of the figure.

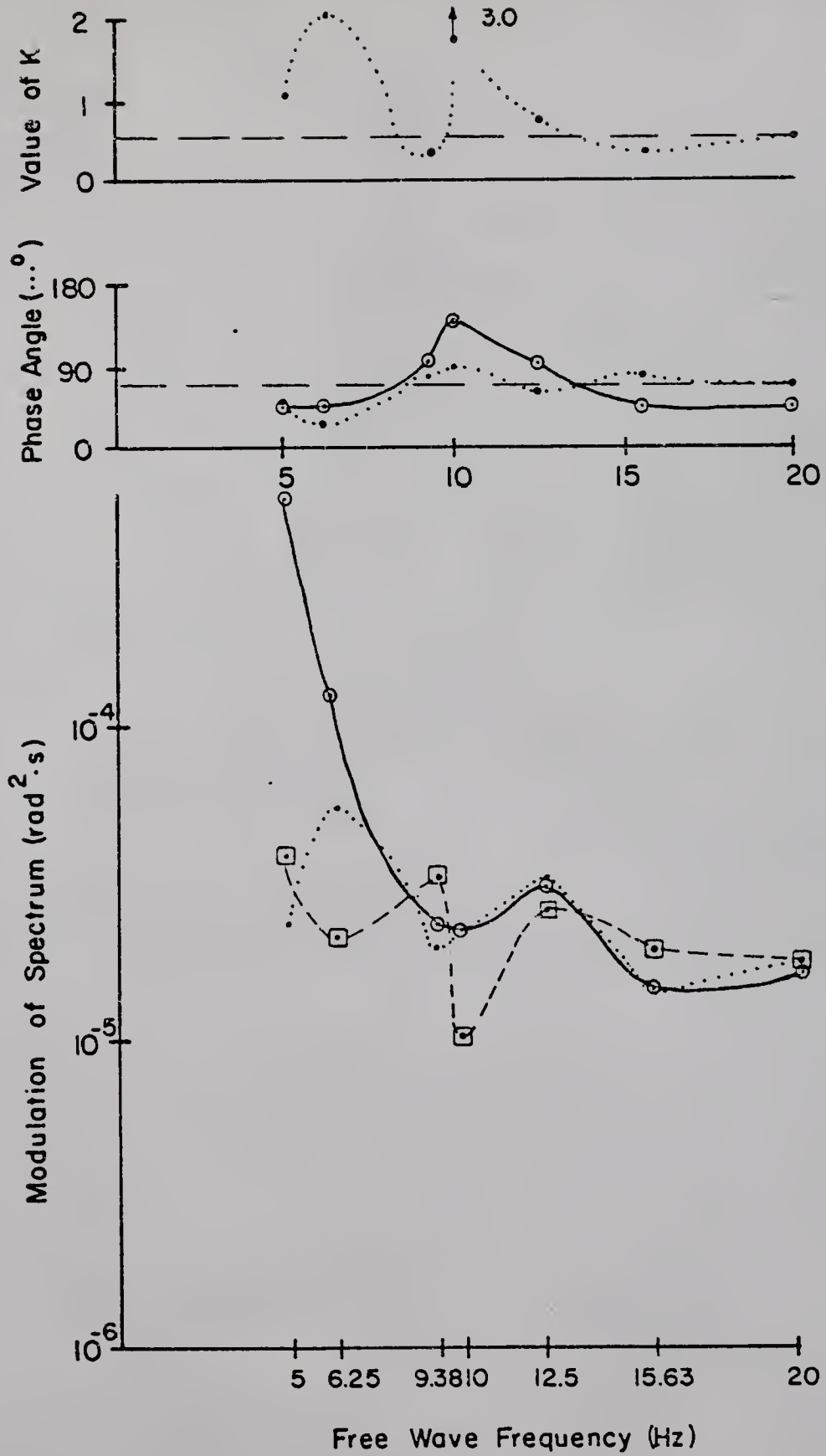


Figure 43. Magnitudes and phases of the short wave slope energy amplitude modulation for the conditions of experiment E3 and test T19. Reference wind speed = 8.3 m/s. Long wave:  $T = 2.0$  s,  $H = 10.0$  cm.

———— Experimentally determined values.  
- - - - Spectral prediction with  $K = 0.5$ .

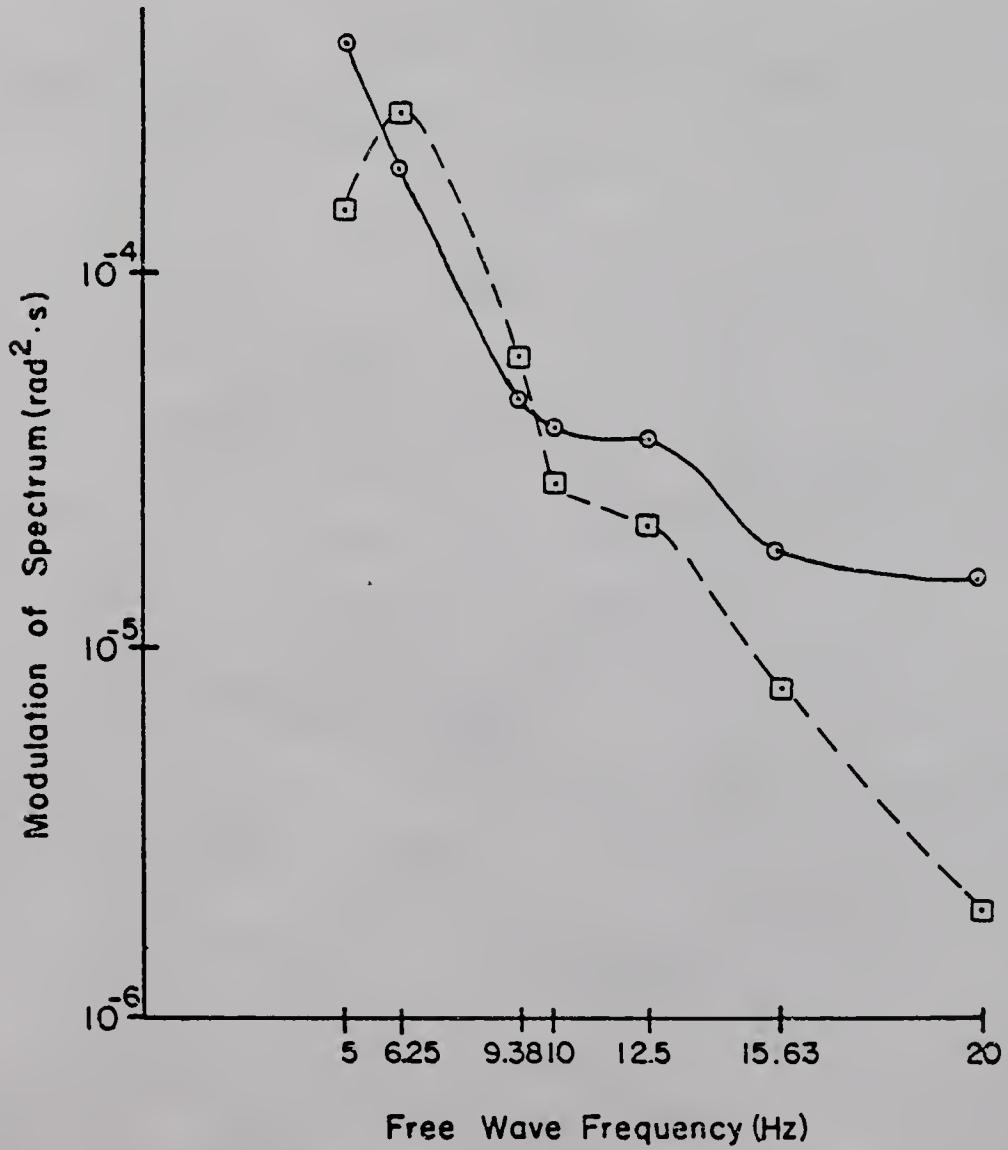
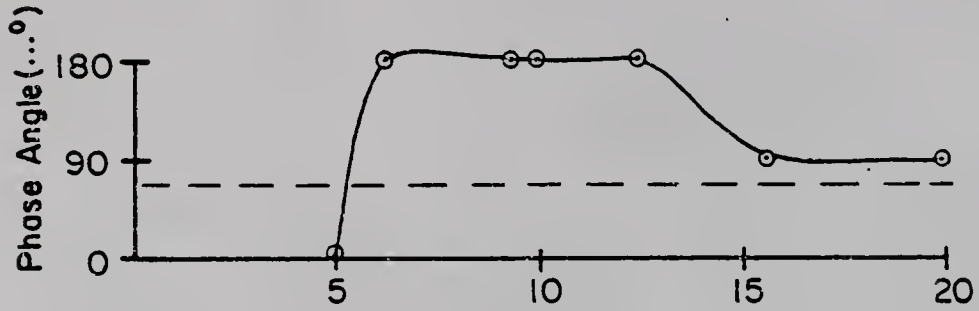
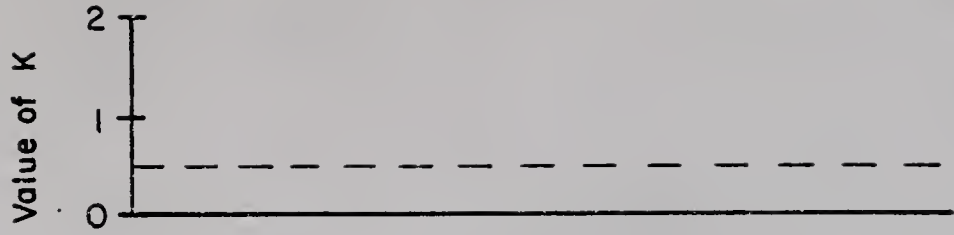


Figure 44. Magnitudes and phases of the short wave slope energy amplitude modulation for the conditions of experiment E3 and test T20. Reference wind speed = 9.2 m/s.  
Long wave:  $T = 2.0$  s,  $H = 10.0$  cm.

- Experimentally determined values.
- - - - Spectral prediction with  $K = 0.5$ .
- Spectral prediction with  $K = 0.5$ , but utilizing an alternate method of finding the first order spectral slope as described in the text.

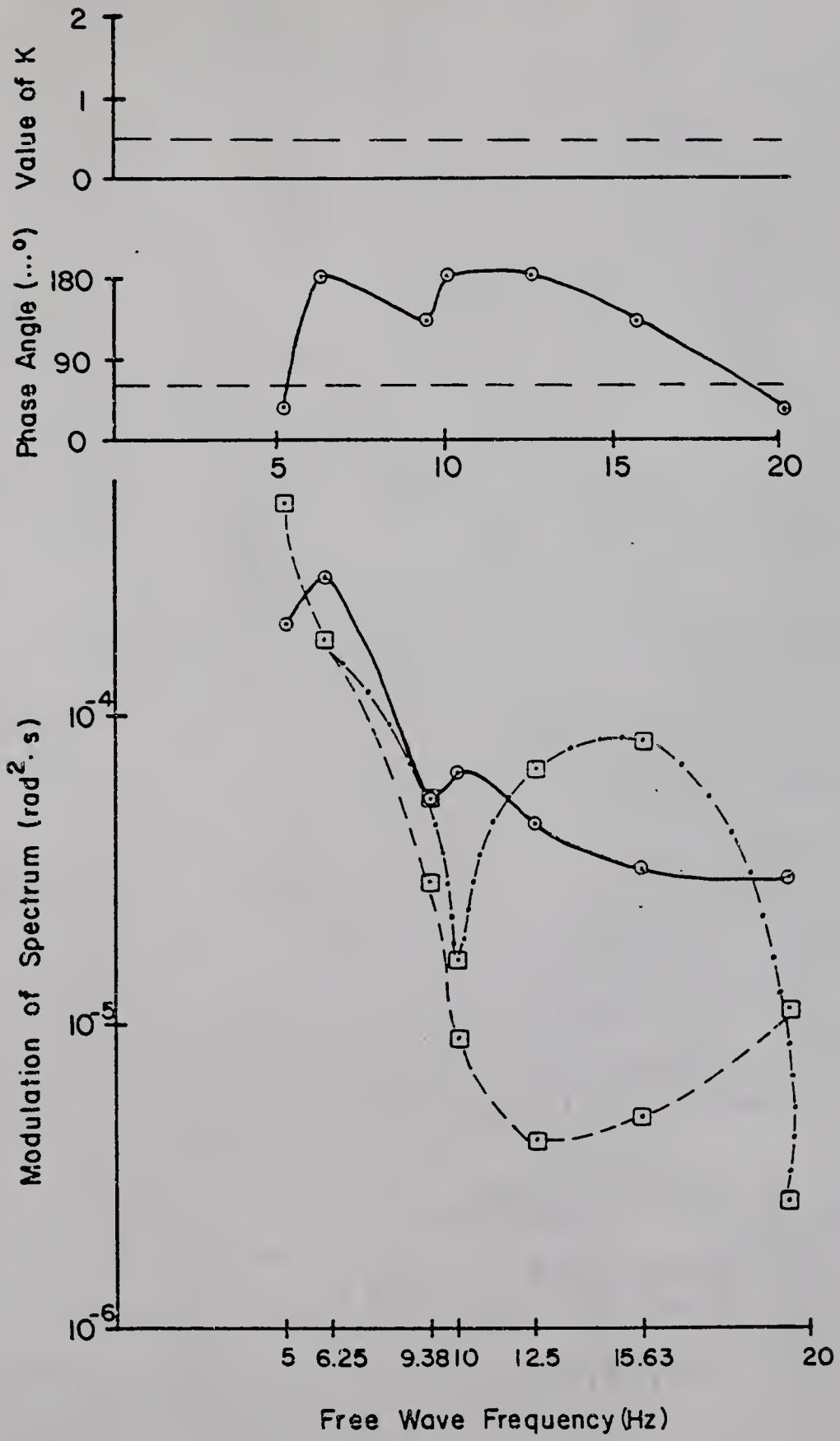


Figure 45. Magnitudes and phases of the short wave slope energy amplitude modulation for the conditions of experiment E3 and test T21. Reference wind speed = 10.1 m/s. Long wave:  $T = 2.0$  s,  $H = 10.0$  cm.

———— Experimentally determined values.  
- - - - Spectral prediction with  $K = 0.5$ .

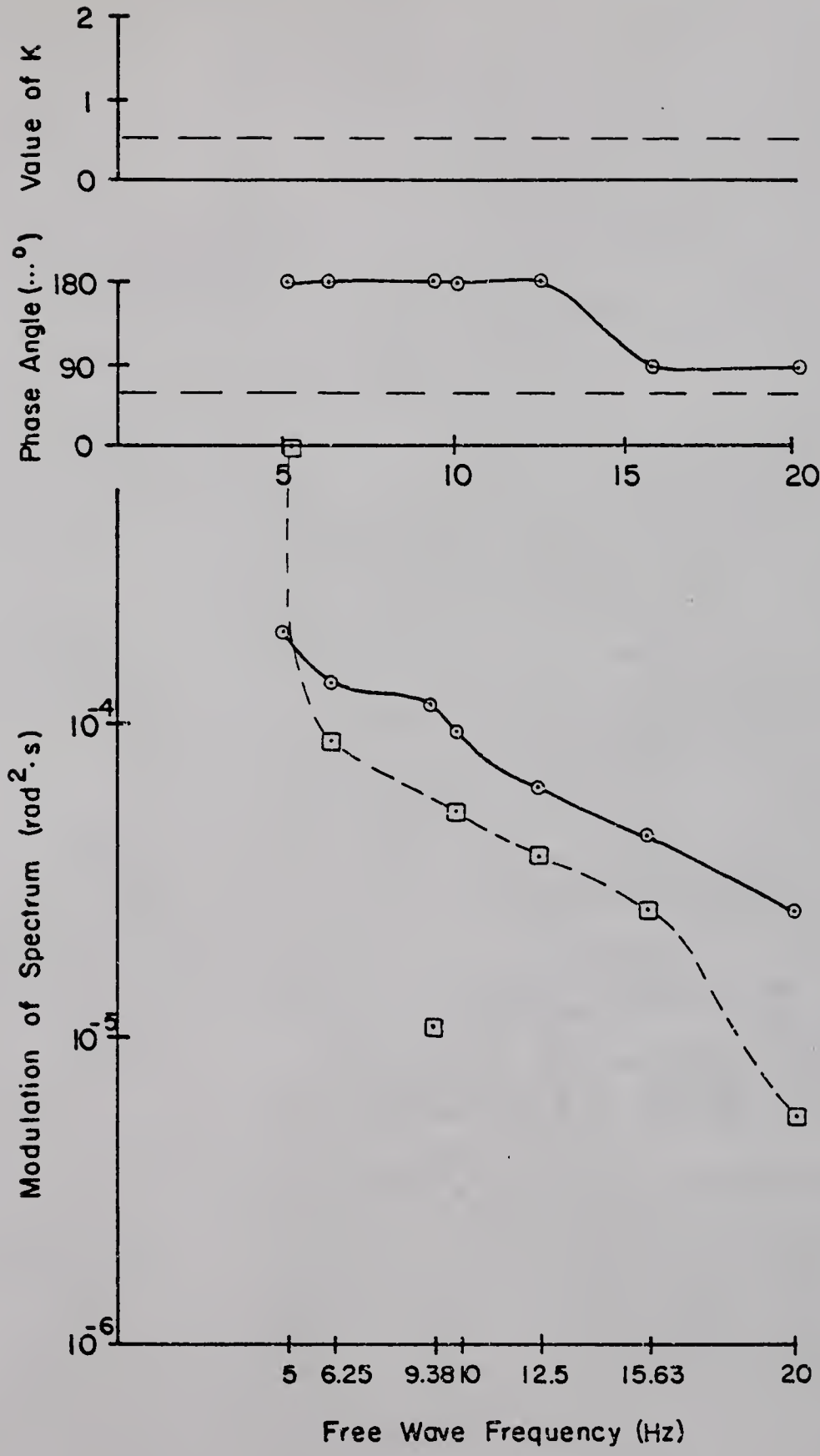


Figure 46. Magnitudes and phases of the short wave slope energy amplitude modulation for the free wave frequency of 5.00 Hz.

- Experimentally determined values.
- - - - Spectral prediction with  $K = 0.5$
- . . . . Spectral prediction with the values of  $K$  indicated in the uppermost part of the figure.

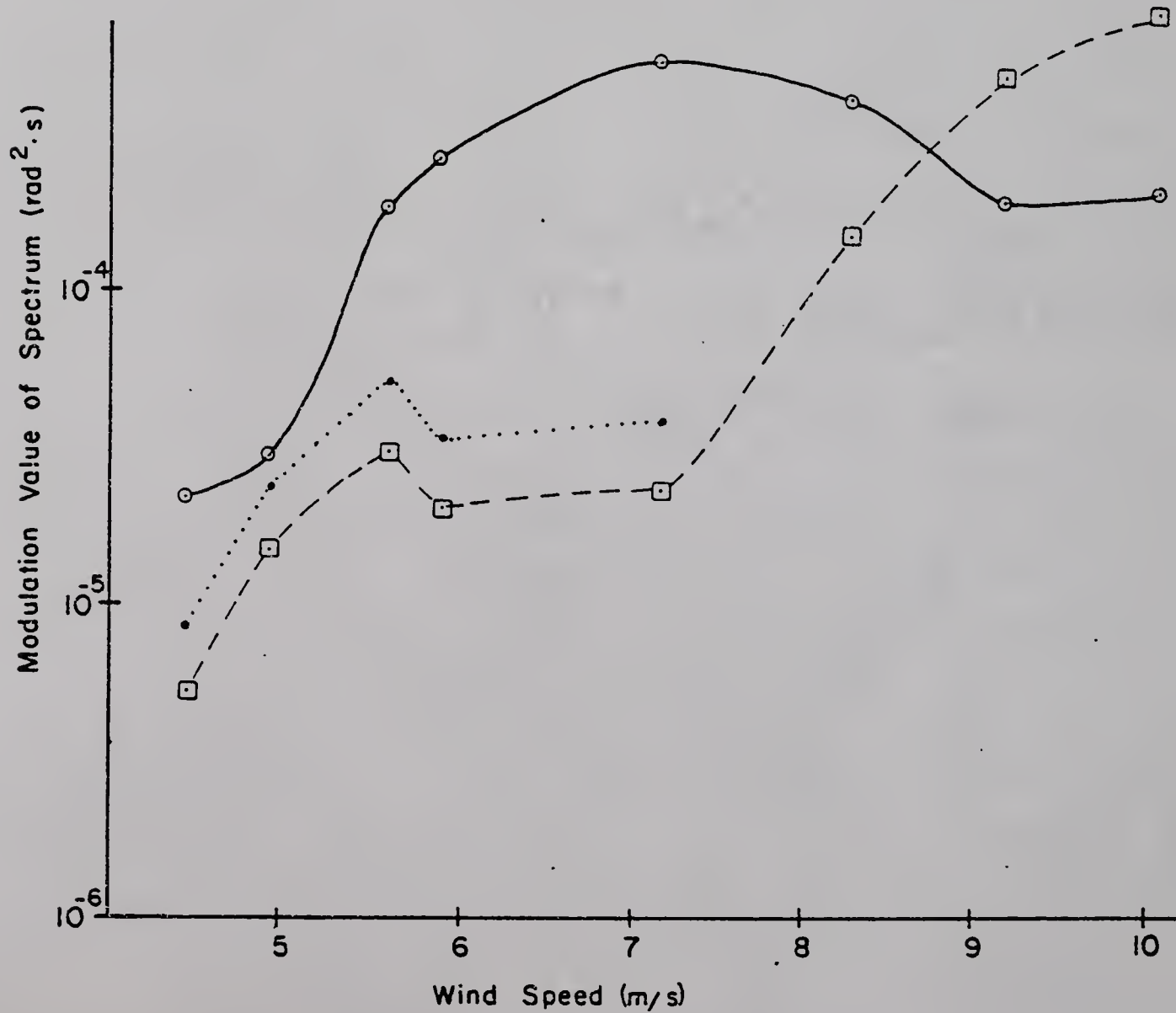
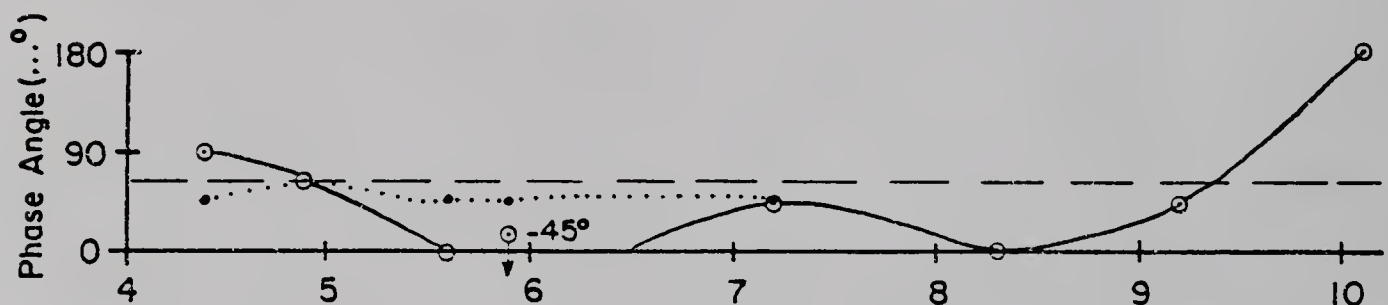
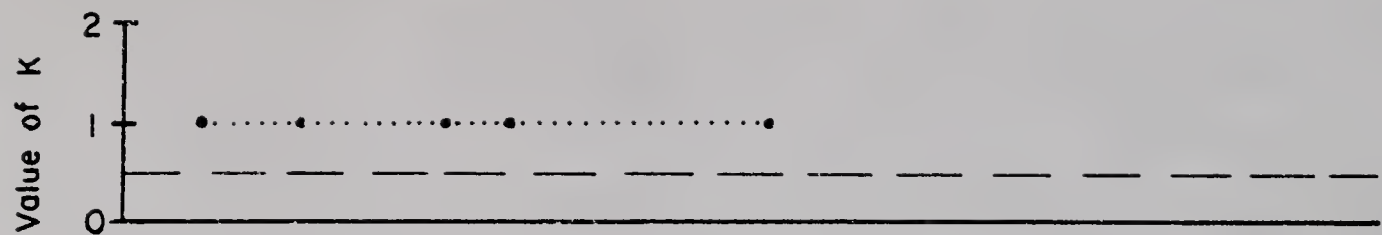


Figure 47. Magnitudes and phases of the short wave slope energy amplitude modulation for the free wave frequency of 6.25 Hz.

- Experimentally determined values.
- - - - Spectral prediction with  $K = 0.5$
- . . . . Spectral prediction with the values of  $K$  indicated in the uppermost part of the figure.

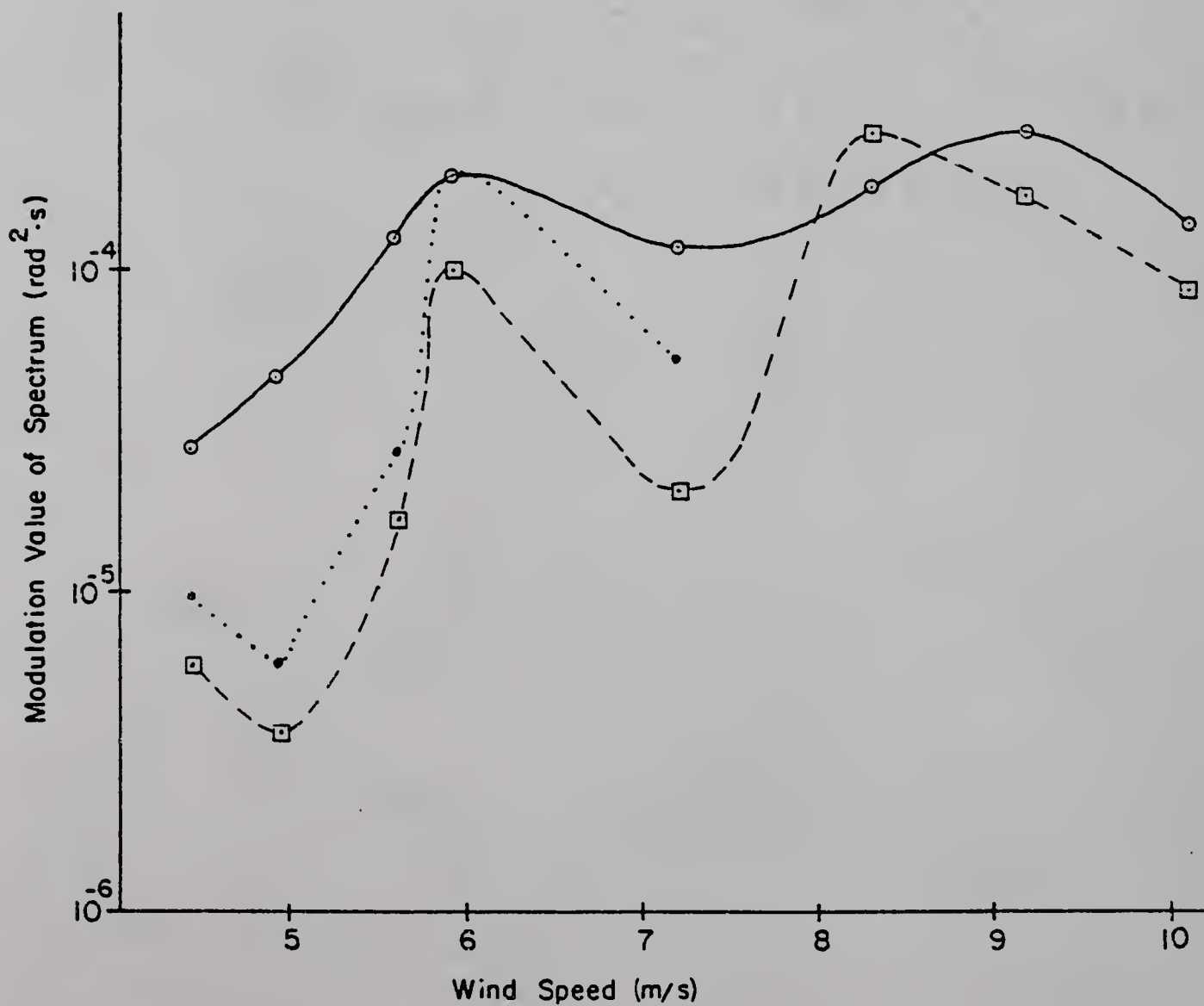
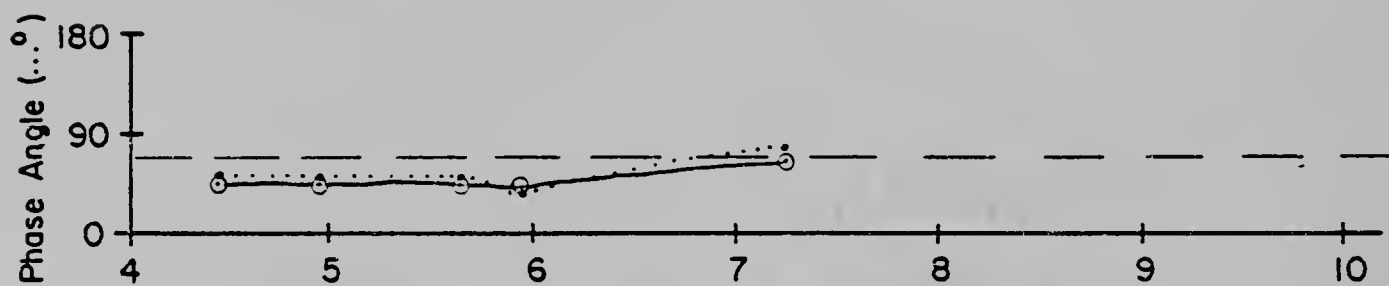
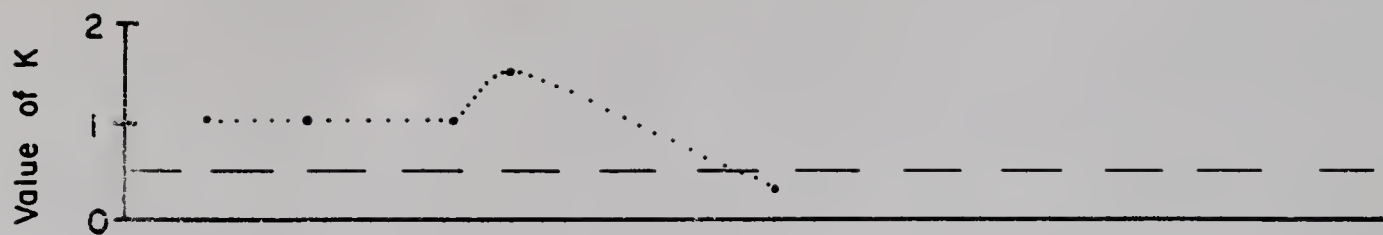


Figure 48. Magnitudes and phases of the short wave slope energy amplitude modulation for the free wave frequency of 9.38 Hz.

- Experimentally determined values.
- - - - Spectral prediction with  $K = 0.5$
- . . . . Spectral prediction with the values of  $K$  indicated in the uppermost part of the figure.

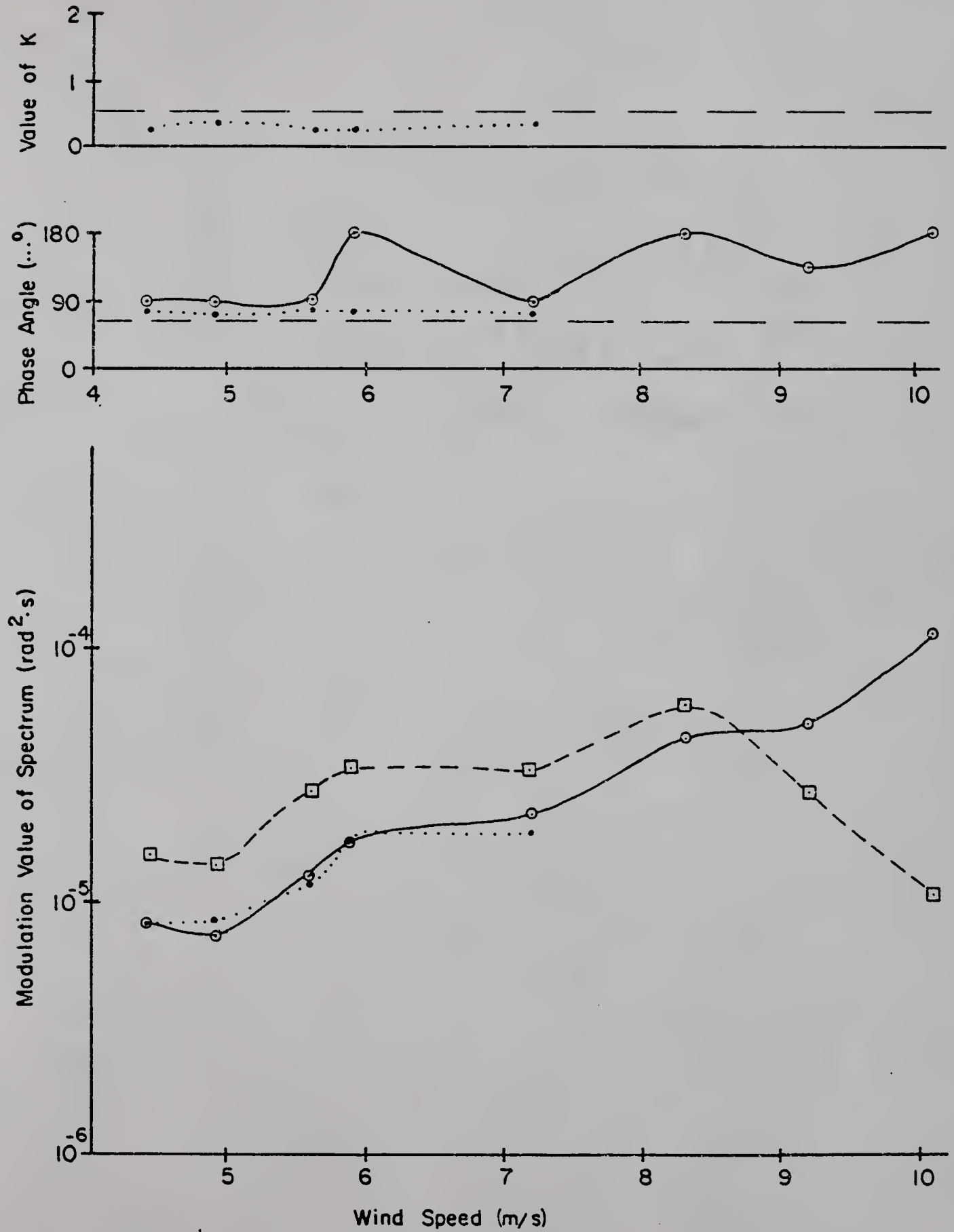


Figure 49. Magnitudes and phases of the short wave slope energy amplitude modulation for the free wave frequency of 10.00 Hz.

- Experimentally determined values.
- - - - Spectral prediction with  $K = 0.5$
- . . . . Spectral prediction with the values of  $K$  indicated in the uppermost part of the figure.

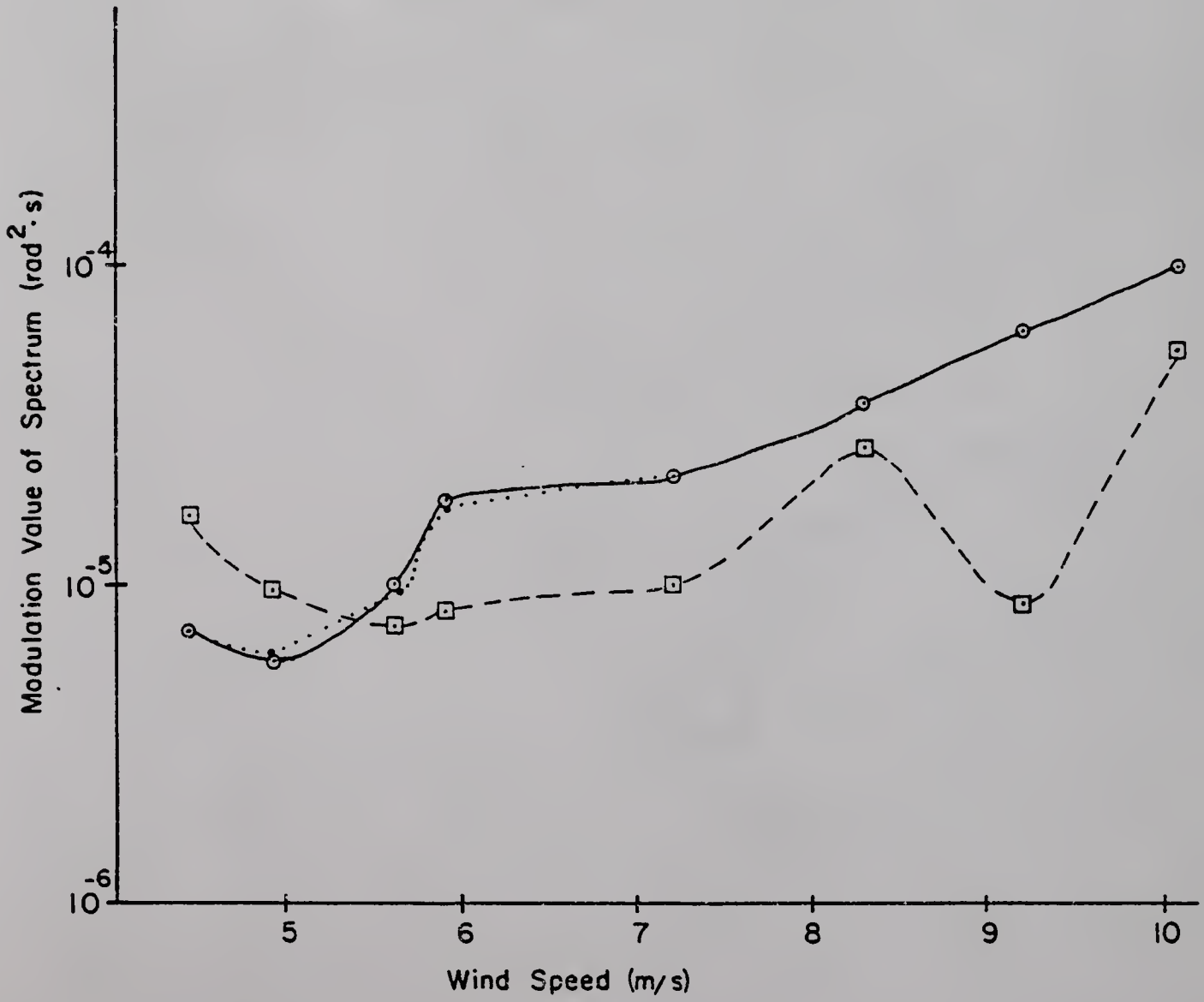
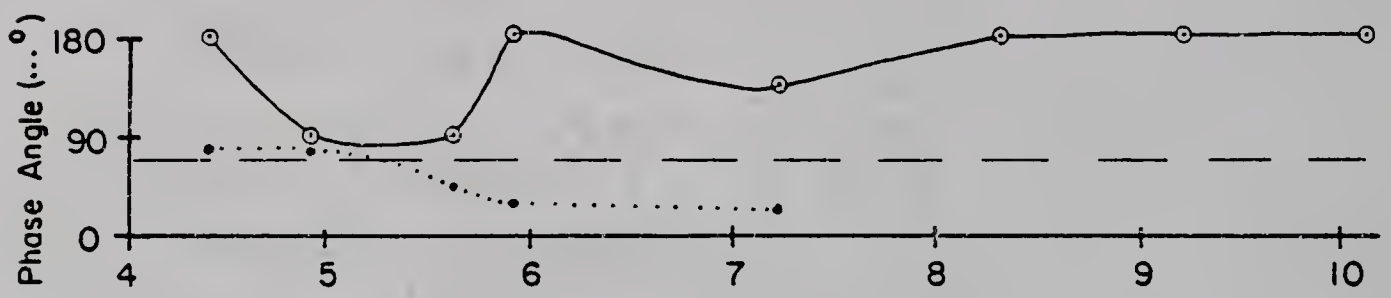
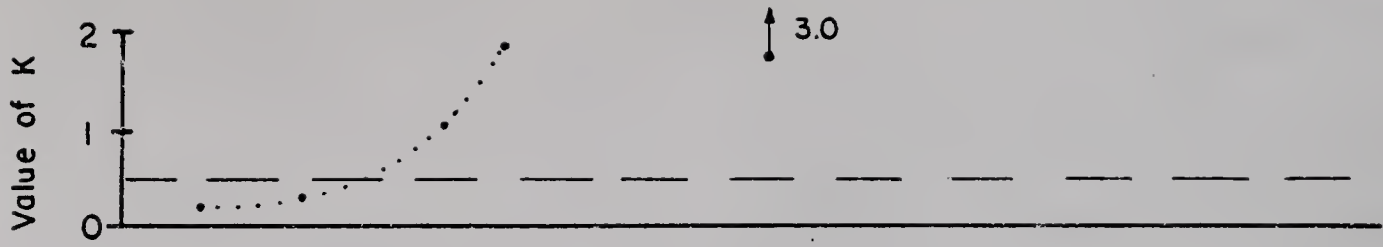


Figure 50. Magnitudes and phases of the short wave slope energy amplitude modulation for the free wave frequency of 12.50 Hz.

- Experimentally determined values.
- - - - Spectral prediction with  $K = 0.5$
- . . . . Spectral prediction with the values of  $K$  indicated in the uppermost part of the figure.

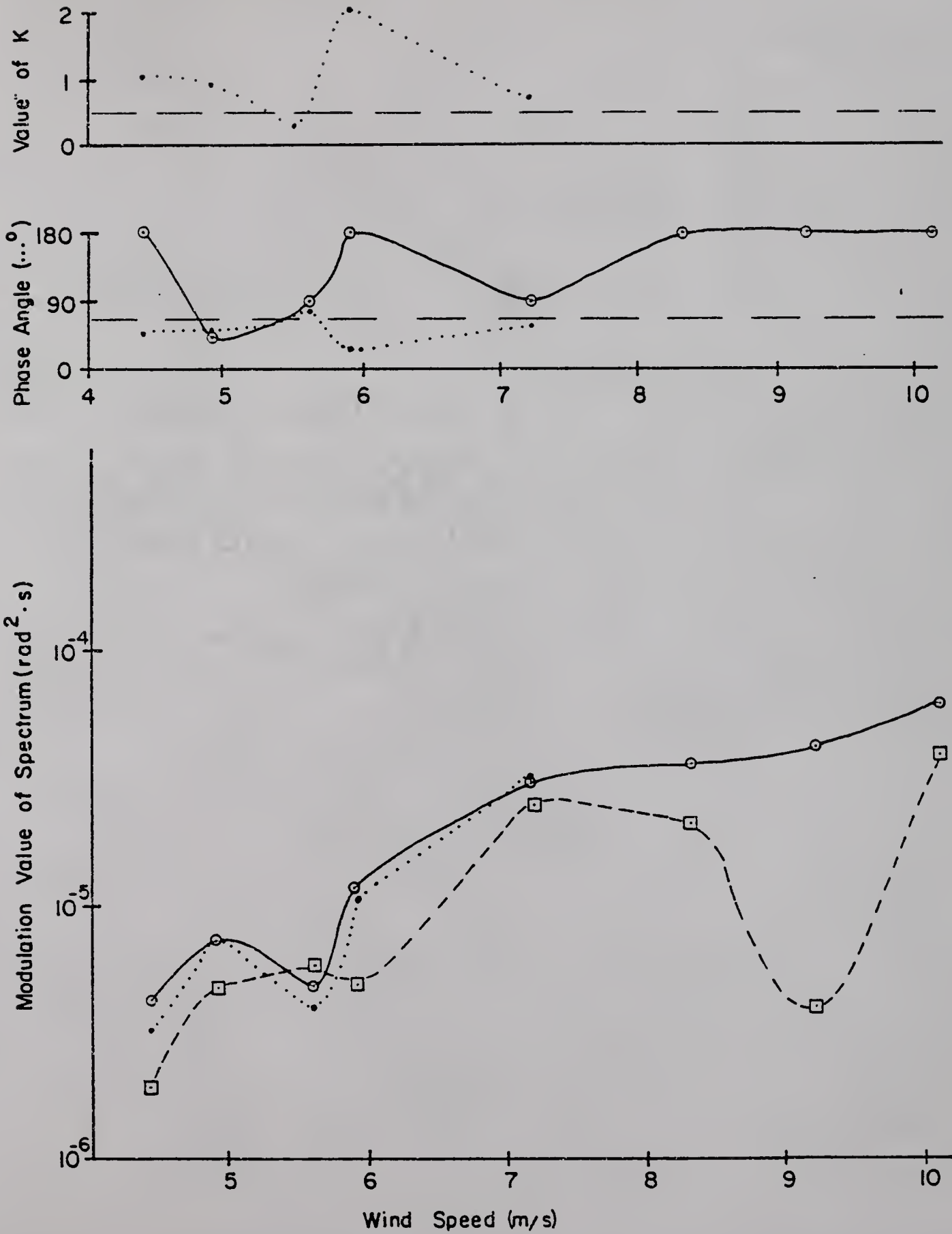


Figure 51. Magnitudes and phases of the short wave slope energy amplitude modulation for the free wave frequency of 15.63 Hz.

- Experimentally determined values.
- - - - Spectral prediction with  $K = 0.5$
- . . . . Spectral prediction with the values of  $K$  indicated in the uppermost part of the figure.

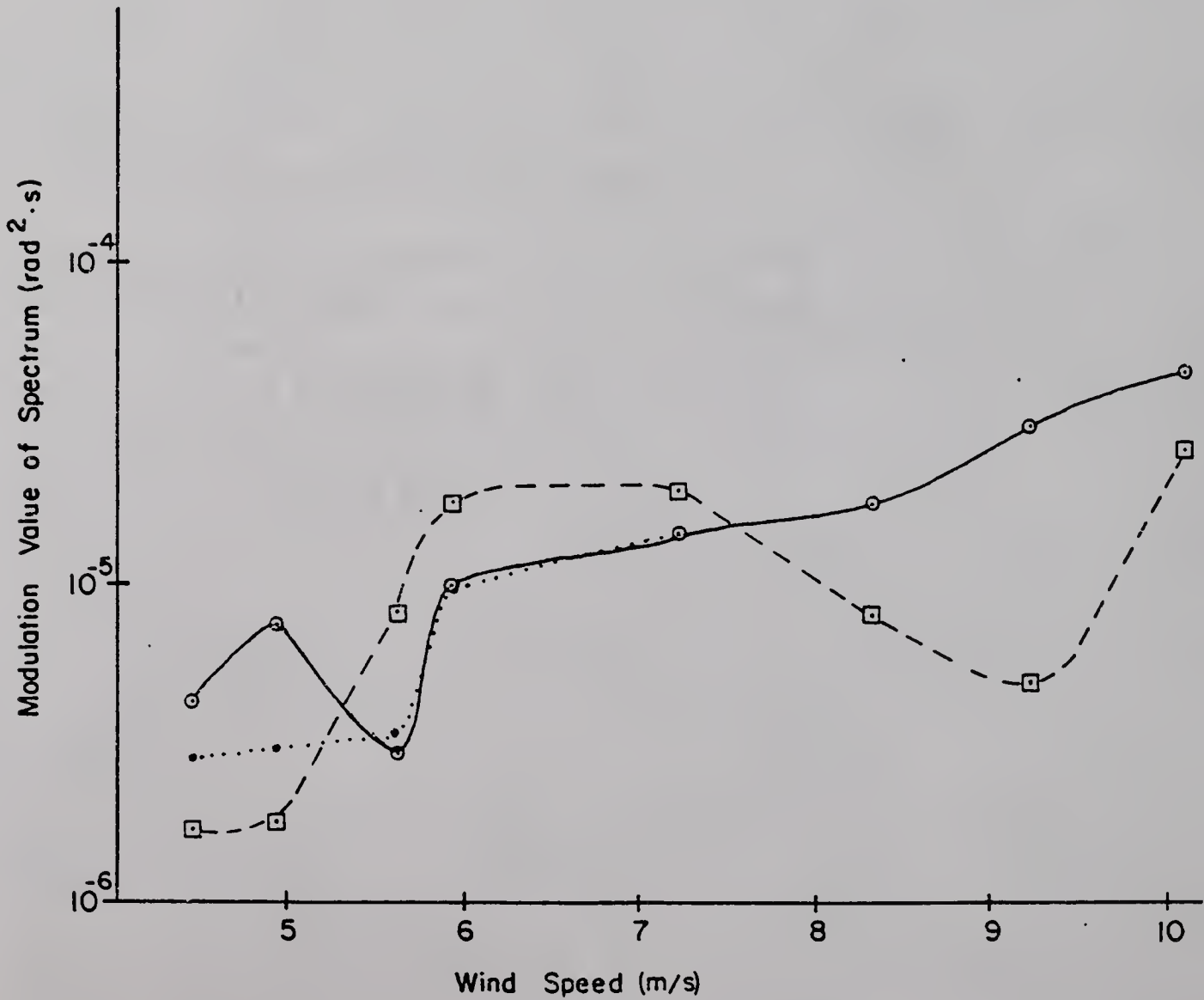
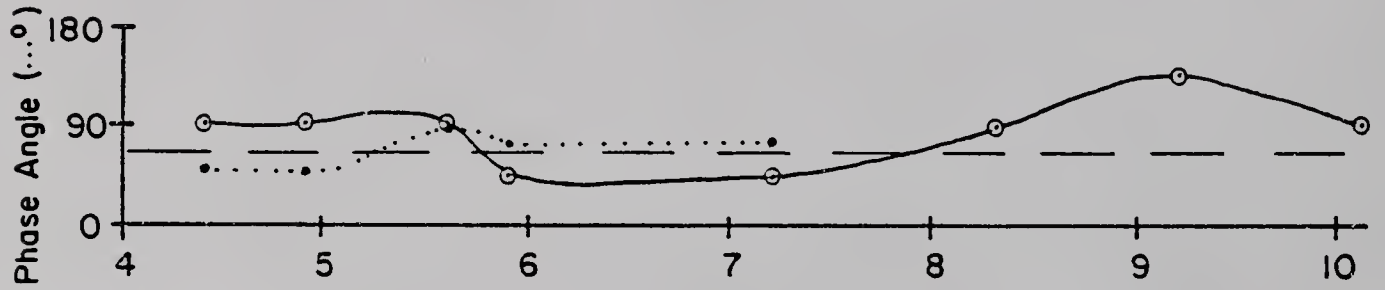
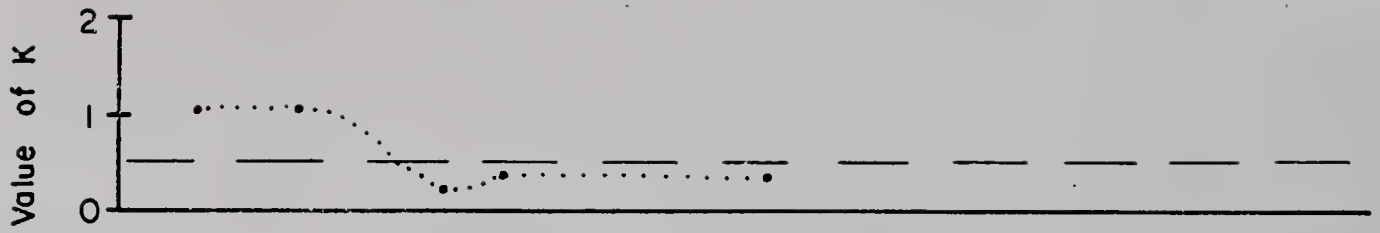
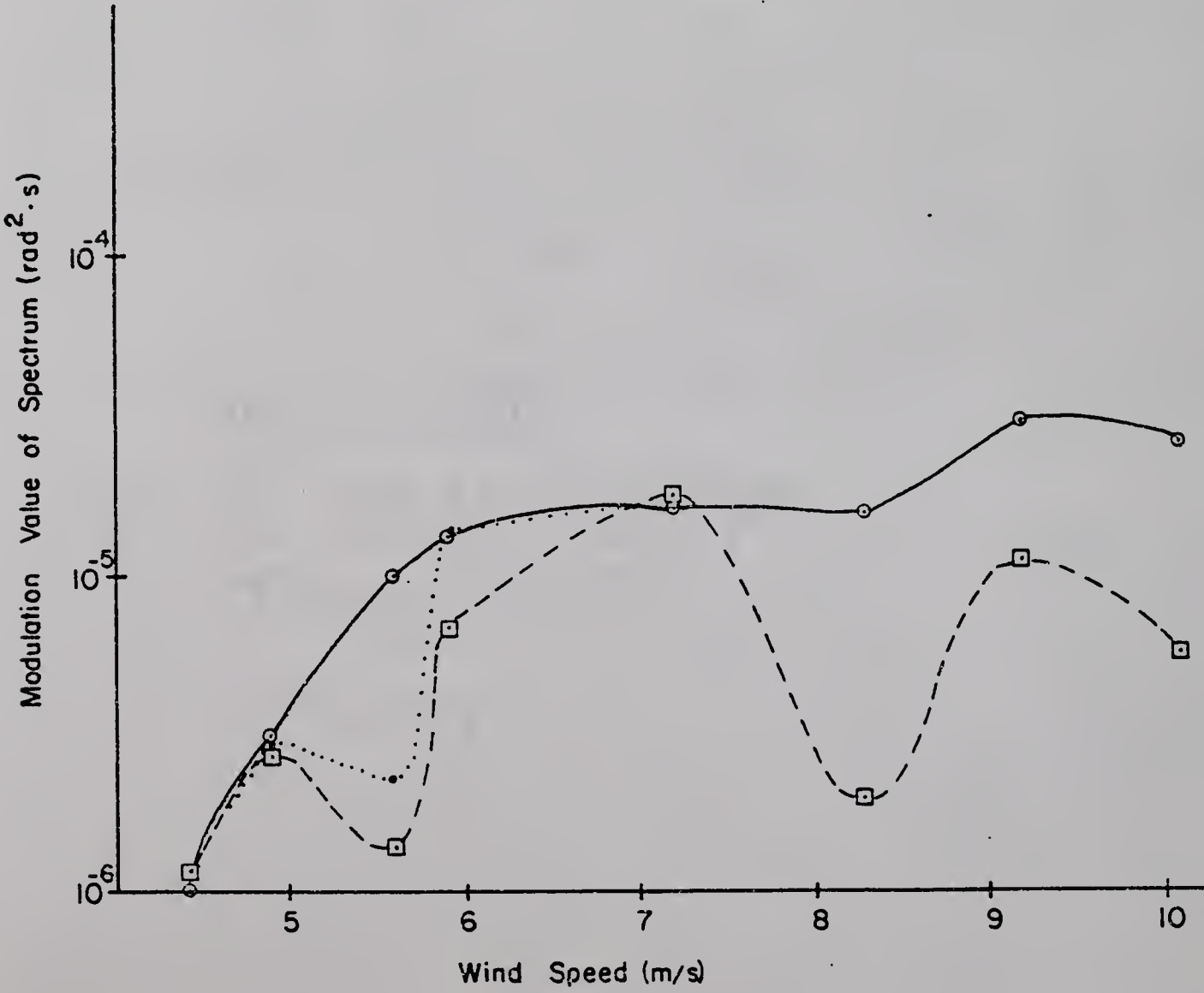
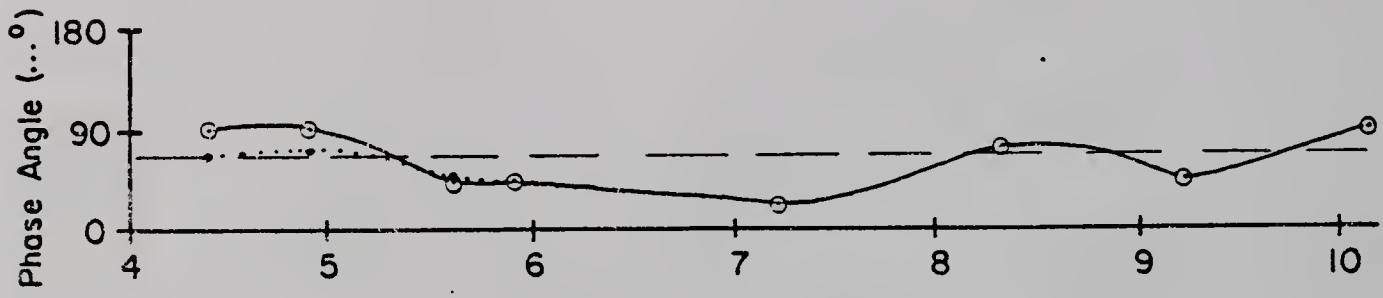
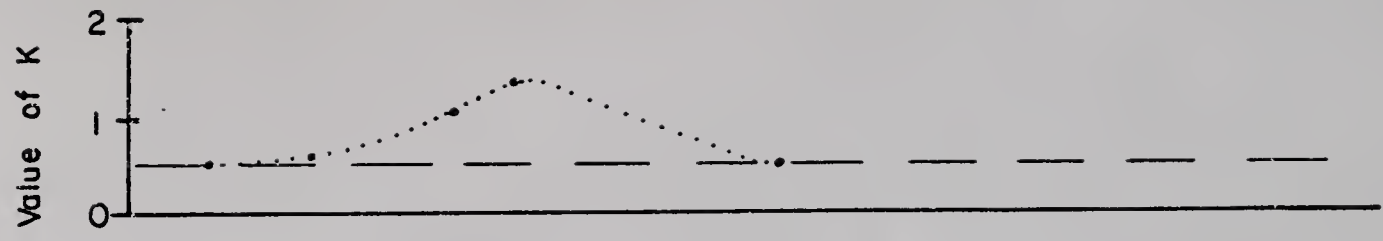


Figure 52. Magnitudes and phases of the short wave slope energy amplitude modulation for the free wave frequency of 20.00 Hz.

- Experimentally determined values.
- - - - Spectral prediction with  $K = 0.5$
- . . . . Spectral prediction with the values of  $K$  indicated in the uppermost part of the figure.



of the prediction calculation and the relative improvement when  $K$  is variable. As before the poorest agreement is for the 5.00 Hz free wave.

## CHAPTER VII

### CONCLUSIONS

The test information contained in this report applies to the free wave frequency range of 5.0 to 20.0 Hz, and a reference wind speed range of 4.4 to 10.1 m/s. Within these experimental bounds the short wave slope energy exhibits a cyclic variation along the long wave profile that is related to the long wave profile. The observed variation is separable conceptually and practically into effects having two origins. The energy density variations result from the combined effect of the short wave frequency variation created by nonuniform short wave energy advection by the long wave orbital velocity, and the variation of the energy content for a short wave component brought about by straining against the long wave orbital flow and the subsequent relaxation through wave-wave interaction toward the mean energy content. Based on the form of the observed behavior it seems reasonable to refer to the spectral energy variation and its constituents relating to the long wave profile as modulations.

The frequency modulation of the short waves, although complicated by the amplitude modulation and the uncertainties in the local wind drift and long wave orbital velocity, is successfully described by the consideration of the linear advection effect. This is especially remarkable when one considers that the spectral computations come from a finite region of observation and are only assumed in a mean sense to be representative of a point where the linear correction is specified.

This study could be profitably extended through accurate quantification of the local surface water velocity.

The frequency modulation is found to be an increasing function of free wave frequency. The mean frequency shift varies from 40% to 126% of the free wave frequency, increasing with free wave frequency and reference wind speed. The peak to peak variation about the mean convected frequency is 58% of that frequency for all wind speeds.

The amplitude of the wave slope energy modulation is considered after compensating for the frequency modulation based on surface velocity. The peak to peak intensity excursion of a variance element in the wave slope spectrum due to the amplitude modulation effect is commonly 100% of the mean value of the intensity. The magnitude of the excursions become smaller as short wave frequency increases, and larger as wind speed increases. The experimentally determined phase relationship between the long wave profile and the intensity variation of a short wave variance element falls between  $45^{\circ}$  and  $180^{\circ}$  with the intensity modulation leading. There is only a slight trend toward larger phase angles with increasing wind speed.

No hydrodynamic theory has been found that is capable of predicting the modulation values found experimentally. The theory in a Hamiltonian formulation does a considerably better job of prediction. In the theory the value of the parameter,  $K$ , the ratio of long wave radian frequency to the relaxation coefficient, may be held constant or allowed to vary to predict modulation behavior. By either approach the prediction lies in the region of the experimentally determined values. In general the theory can be made to conform quite accurately to the experimental values of modulation amplitude if  $K$  is allowed to vary. In addition, by

doing so the predicted phase angle is usually moved toward the experimental value. Present results indicate that the minimum values of  $K$  are required in the vicinity of 9 Hz and that they increase on either side of this minimum. Further detailed study that includes long wave steepness changes may indicate consistent trends in  $K$  values that would allow it to be functionally described in terms of wind speed, short wave frequency, and long wave parameters.

The analysis in the Hamiltonian formulation is extremely sensitive to the magnitude of  $\partial\Psi^{(0)}/\partial\omega$ , derived from the first order spectrum. To develop more confidence in the general utility of the prediction by the Hamiltonian formulation of the amplitude modulation, the calculation of  $\partial\Psi^{(0)}/\partial\omega$  should be the focus of an investigation designed to indicate the method by which the most reliable estimate of it can be obtained.

## APPENDIX I

### THE BOLTZMANN TRANSPORT EQUATION

The Hamiltonian formulation of a problem is a general approach in which a system is specified through its momentum and generalized coordinates. The  $m$  generalized coordinates,  $q_i$ , specify the position vector,  $\underline{r}_j$ , in cartesian space. The conversion is

$$\underline{r}_j = \underline{r}_j(q_1, q_2, \dots, q_m) \quad . \quad (I-1)$$

The problem is formulated in phase space where for each  $m$  degrees of freedom of a mechanical system there are  $2m$  quantities required to specify its motion. Phase space is made up of  $m$  pairs of axes, the coordinates,  $q_i$ , and the associated momenta,  $p_i$ . A point, passing through the phase space representing the motion of a system in physical space, is then completely specified by  $2m$  vectors.

The Lagrangian function,  $L$ , is necessary for use in the definition of the Hamiltonian function. The Lagrangian is defined as (McCuskey, 1959)

$$L = T - V \quad , \quad (I-2)$$

where  $T$  is the kinetic energy and  $V$  the potential energy of the system under study. In terms of generalized coordinates we have

$$L = L(q_i, \dot{q}_i, t) \quad . \quad (i = 1, m) \quad (I-3)$$

The generalized momentum,  $p_i$ , to be associated with the coordinate,  $q_i$ , is defined as

$$p_i = \frac{\partial L}{\partial \dot{q}_i} \quad . \quad (i = 1, m) \quad (I-4)$$

The potential field,  $V$ , in this case is assumed to contain no variations in either physical space or phase space. Hence

$$\frac{\partial L}{\partial \dot{q}_i} = \frac{\partial T}{\partial \dot{q}_i} \quad , \quad (\text{I-5})$$

where  $T$  is a quadratic function of the generalized velocities. From (I-1) we find

$$\Delta \underline{r}_j = \sum_{i=1}^m \frac{\partial \underline{r}_j}{\partial q_i} \Delta q_i \quad \text{and} \quad \Delta \dot{\underline{r}}_j = \sum_{i=1}^m \frac{\partial \underline{r}_j}{\partial q_i} \dot{q}_i \quad . \quad (\text{I-6})$$

Then by definition of the kinetic energy and substitution of (I-6) we are able to find the expression for the total kinetic energy of a system of  $n$  particles in terms of generalized velocities. It is given by

$$T \equiv \frac{1}{2} \sum_{j=1}^n m_j \dot{\underline{r}}_j^2 = \frac{1}{2} \sum_{j=1}^n m_j \left[ \sum_{k=1}^m \sum_{i=1}^m \frac{\partial \underline{r}_j}{\partial q_k} \cdot \frac{\partial \underline{r}_j}{\partial q_i} \right] \dot{q}_k \dot{q}_i \quad . \quad (\text{I-7})$$

Changing the order of summation, we have

$$T = \frac{1}{2} \sum_{k=1}^m \sum_{i=1}^m \left[ \sum_{j=1}^n m_j \frac{\partial \underline{r}_j}{\partial q_k} \cdot \frac{\partial \underline{r}_j}{\partial q_i} \right] \dot{q}_k \dot{q}_i \quad . \quad (\text{I-8})$$

Finally, the bracket can be written as a coefficient,  $a_{ki}$ , which does not depend on the velocities, and we have

$$T = \frac{1}{2} \sum_{k=1}^m \sum_{i=1}^m a_{ki} \dot{q}_k \dot{q}_i \quad . \quad (\text{I-9})$$

We find the expression for the generalized momentum from (I-4), (I-5), and (I-9). They yield

$$p_i = \sum_{k=1}^m a_{ki} \dot{q}_k \quad . \quad (i = 1, m) \quad (\text{I-10})$$

Hamilton replaced the Lagrangian function with a function now called the Hamiltonian and defined as

$$H(p_i, q_i, t) = \sum_{i=1}^m p_i \dot{q}_i - L(q_i, \dot{q}_i, t) \quad , \quad (\text{I-11})$$

where  $H$  is not explicitly a function of  $\dot{q}_i$ , since  $p_i$  can be solved for  $\dot{q}_i$  from the set of equations (I-10). The differential  $H$  then becomes

$$dH = \sum_{i=1}^m p_i d\dot{q}_i + \sum_{i=1}^m \dot{q}_i dp_i - \sum_{i=1}^m \frac{\partial L}{\partial q_i} dq_i - \sum_{i=1}^m \frac{\partial L}{\partial \dot{q}_i} d\dot{q}_i - \frac{\partial L}{\partial t} dt \quad . \quad (\text{I-12})$$

From the definition of  $p_i$ , equation (I-4), the first and fourth terms above cancel. From equation (I-11) we have the following

$$\frac{\partial H}{\partial p_i} = \dot{q}_i, \quad \frac{\partial H}{\partial q_i} = - \frac{\partial L}{\partial q_i} = -\dot{p}_i, \quad \frac{\partial H}{\partial t} = - \frac{\partial L}{\partial t} \quad . \quad (\text{I-13})$$

Using (I-13) we can rewrite (I-12) as

$$dH = \sum_{i=1}^m \frac{\partial H}{\partial p_i} dp_i + \sum_{i=1}^m \frac{\partial H}{\partial q_i} dq_i + \frac{\partial H}{\partial t} dt \quad , \quad (\text{I-14})$$

and we can write

$$\frac{dH}{dt} = \sum_{i=1}^m \frac{\partial H}{\partial p_i} \dot{p}_i + \sum_{i=1}^m \frac{\partial H}{\partial q_i} \dot{q}_i + \frac{\partial H}{\partial t} \quad . \quad (\text{I-15})$$

The meaning of the Hamiltonian can be found easily for this case. The summation term in equation (I-11) can be written in a different form using equations (I-4) and (I-5) as

$$\sum_{i=1}^m p_i \dot{q}_i = \sum_{i=1}^m \frac{\partial L}{\partial \dot{q}_i} \dot{q}_i = \sum_{i=1}^m \dot{q}_i \frac{\partial T}{\partial \dot{q}_i} \quad . \quad (\text{I-16})$$

T is a homogeneous function of degree two in generalized velocity. So by Euler's theorem for homogeneous functions (Wylie, 1966) it is known that

$$\sum_{i=1}^m \dot{q}_i \frac{\partial T}{\partial \dot{q}_i} = 2T \quad . \quad (\text{I-17})$$

Thus H is shown to be the total energy of the system expressed in the coordinates of phase space. From (I-11) we arrive at

$$H = 2T - (T - V) = T + V = E \quad . \quad (\text{I-18})$$

Equation (I-15) becomes

$$\frac{dE}{dt} = \frac{\partial E}{\partial p_i} \dot{p}_i + \frac{\partial E}{\partial q_i} \dot{q}_i + \frac{\partial E}{\partial t} \quad , \quad (\text{I-19})$$

making use of the tensor summation convention. The variable,  $\dot{q}_i$ , is clearly the velocity of propagation of the energy, E, in the dimension of the generalized coordinates. Hasselmann used the wavenumbers,  $k_i$ , rather than the momenta, to complete each of the phase planes in phase space. For wave motion this arises logically in the following way. The momentum is given as a function of the total orbital velocity,  $m|U_i|$ . From linear wave theory we have  $m|U_i| = mck_i$ , which is the momentum associated with a wave packet specified by  $k_i$ . Therefore,  $p_i = f(k_i)$ . The equation for the Lagrangian change in the wave energy resulting from external factors, S, is given by

$$\frac{dE}{dt} = \frac{\partial E}{\partial k_i} k_i + \frac{\partial E}{\partial q_i} \dot{q}_i + \frac{\partial E}{\partial t} = S \quad , \quad (\text{I-20})$$

and is known as the Boltzmann transport equation.

To go along with this equation there are two geometrical equations of motion which apply to any kind of wave motion, and were used for

surface waves by Ursell (1960) and Whitham (1960). The equations are called the Hamiltonian equations and are

$$\dot{q}_i = \frac{\partial}{\partial k_i} \omega(q, k) \quad , \quad (\text{I-21})$$

and

$$\dot{k}_i = - \frac{\partial \omega}{\partial q_i} (q, k) \quad . \quad (\text{I-22})$$

Dorrestein (1960) pointed out the analogy between equation (I-20) that specifies the evolution of the wave spectral energy and Liouville's theorem. Rather than dealing with a single physical particle that has a single representative point associated with it, Liouville's theorem deals with a continuum of representative points. Liouville defined a number density function,  $\rho(p, q, t)$ , that gives the number of representative points in an elemental area of a phase plane. By performing a simple balance type of analysis on an elemental area  $dp \cdot dq$  in the phase plane, the following continuity equation results. The conservation of number is

$$\frac{\partial \rho}{\partial t} + \dot{p} \frac{\partial \rho}{\partial p} + \dot{q} \frac{\partial \rho}{\partial q} = 0 \quad . \quad (\text{I-23})$$

This fundamental law in classical statistical mechanics states that in phase space the density of a continuum of points remains constant as we follow any point. The wave analogy is that any spectral energy density function for a wave system in wavenumber space remains constant, as we follow any wave group. Of course, the addition of source terms,  $S$ , to the balance means that the material change in the spectral energy density need no longer be zero.

## APPENDIX II

### THE WAVE-WAVE INTERACTION INTEGRAL

If the multiple wave hydrodynamic boundary value problem is expanded in a perturbation analysis, it is found that at high order the energy term may become nonstationary, resulting in an energy flux among spectral components. If the problem expansion in wave slope goes as

$$\phi = \epsilon \phi^{(1)} + \epsilon^2 \phi^{(2)} + \epsilon^3 \phi^{(3)} + \dots, \quad (\text{II-1})$$

then the energy expansion goes as

$$E = \epsilon E_2 + \epsilon^3 E_4 + \epsilon^5 E_6 + \dots, \quad (\text{II-2})$$

Valenzuela and Laing (1972) found that in a gravity-capillary wave system, a resonant interaction could occur at second order in the energy spectrum. The nonstationarity occurs in  $E_4$ , requiring a third order analysis in wave slope for evaluation. The nonlinear source term required in the Boltzmann transport equation is written in Valenzuela's (1975) shorthand notation as

$$\begin{aligned} H = & \iint_{-\infty}^{\infty} T_1(k_1, k_2, k_3) (\omega_3 \Psi_1 \Psi_2 - \omega_2 \Psi_1 \Psi_3 - \omega_1 \Psi_2 \Psi_3) \\ & \cdot \delta(\omega_3 - \omega_2 - \omega_1) dk_{x_1} dk_{y_1} + 2 \iint_{-\infty}^{\infty} T_2(k_1, k_3, k_2) \\ & \cdot (\omega_3 \Psi_1 \Psi_2 - \omega_2 \Psi_1 \Psi_3 + \omega_1 \Psi_2 \Psi_3) \delta(\omega_3 - \omega_2 + \omega_1) dk_{x_1} dk_{y_1}. \quad (\text{II-3}) \end{aligned}$$

The subscripts on the energy spectra refer to the wavenumber at which the value is to be taken from the spectrum. The functions,  $T$ , are the

coupling coefficients given in Valenzuela and Laing (1972). The Dirac delta functions limit the contributions from the integrals to the conditions when the proper relationships among the wavenumbers and frequencies exist. The first integral term contributes to H when  $k_3 = k_1 + k_2$  and  $\omega_3 = \omega_1 + \omega_2$ . The second integral term contributes when  $k_3 = k_2 - k_1$  and  $\omega_3 = \omega_2 - \omega_1$ .

As in the Boltzmann transport equation, the energy spectrum is perturbed

$$\Psi_i = \Psi_i^{(0)} + \epsilon \Psi_i^{(1)} + O(\epsilon^2) \quad , \quad (\text{II-4})$$

where  $\epsilon$  is the long wave slope. The resulting equation of order  $\epsilon$  which evolves from equation (II-3) is

$$\begin{aligned} H^{(1)} = & \iint_{-\infty}^{\infty} T_1 [(\omega_2 + \omega_1) (\Psi_1^{(0)} \Psi_2^{(1)} + \Psi_2^{(0)} \Psi_1^{(1)}) - \omega_2 (\Psi_1^{(0)} \Psi_1^{(1)} + \Psi_3^{(0)} \Psi_1^{(1)}) \\ & - \omega_1 (\Psi_2^{(0)} \Psi_3^{(1)} + \Psi_3^{(0)} \Psi_2^{(1)})] \delta(\omega_3 - \omega_2 - \omega_1) dk_{x_1} dk_{y_1} \\ & + 2 \iint_{-\infty}^{\infty} T_2 [(\omega_2 - \omega_1) (\Psi_1^{(0)} \Psi_2^{(1)} + \Psi_2^{(0)} \Psi_1^{(1)}) - \omega_2 (\Psi_1^{(0)} \Psi_3^{(1)} + \Psi_3^{(0)} \Psi_1^{(1)}) \\ & + \omega_1 (\Psi_2^{(0)} \Psi_3^{(1)} + \Psi_3^{(0)} \Psi_2^{(1)})] \delta(\omega_3 - \omega_2 + \omega_1) dk_{x_1} dk_{y_1} \quad . \quad (\text{II-5}) \end{aligned}$$

Collect the terms of (II-5) into groupings based on first order terms.

The factors with the superscript + are for the condition,  $k_3 = k_2 + k_1$ , and the superscript - refers to the condition,  $k_3 = k_2 - k_1$ . The result is

$$\begin{aligned}
H^{(1)} = & \iint_{-\infty}^{\infty} \left\{ \Psi_1^{(1)} [T_1(\omega_2 + \omega_1) \Psi_2^{(0)} - T_1 \omega_2 \Psi_3^{(0)+} + 2T_2(\omega_2 - \omega_1) \Psi_2^{(0)} \right. \\
& - 2T_2 \omega_2 \Psi_3^{(0)-}] + \Psi_2^{(1)} [T_1(\omega_2 + \omega_1) \Psi_1^{(0)} - T_1 \omega_1 \Psi_3^{(0)+} + 2T_2(\omega_2 - \omega_1) \Psi_1^{(0)} \\
& + 2T_2 \omega_1 \Psi_3^{(0)-}] - \Psi_3^{(1)+} [T_1 \omega_2 \Psi_1^{(0)} + T_1 \omega_1 \Psi_2^{(0)}] \\
& \left. + \Psi_3^{(1)-} [-2T_2 \omega_2 \Psi_1^{(0)} + 2T_2 \omega_1 \Psi_2^{(0)}] \right\} dk_{x_1} dk_{y_1} . \quad (II-6)
\end{aligned}$$

From equation (II-6) arises the shorthand integral notation used in the body of this paper. By comparison to (II-6) we have the form

$$H^{(1)}(k_3) = \int_{k_1} I^{(0)}(\Psi^{(0)}, k_2, k_1) \Psi^{(1)}(k_1) dk_1 . \quad (II-7)$$

The value of this integral is not readily obtained. Keller and Wright (1975) proposed that a relaxation approximation be used to represent the behavior of the  $H^{(1)}$  term. The term relaxation, refers to the response of a dynamical system to a time varying input, analogous to the decay response of a system to an impulsive input. In this case a sinusoidal excitation, due to straining, is presumed. The foregoing leads to the assumption that the spectral form, when driven away from the equilibrium form by an external force, will return to equilibrium at a rate proportional to the difference between the existing spectral amplitude and the equilibrium value. If left unexcited in time the value of  $\Psi^{(1)}$  will go toward zero, and a logical form for  $\Psi^{(1)}(k_3, t)$  becomes

$$\Psi^{(1)}(k_3, t) = [\Psi^{(1)}(k_3)]_{\max} e^{-\beta_r t} , \quad (II-8)$$

where  $\beta_r$  gives the rate at which relaxation occurs, and is called the relaxation constant.

Examining the order  $\epsilon$  component of the Boltzmann equation for the condition when no underlying current is allowed and  $\psi^{(1)}$  has no spatial variations, it becomes

$$\frac{\partial \psi^{(1)}(k_3, t)}{\partial t} = \beta \psi^{(1)}(k_3, t) + \int_{k_1} I^{(0)}(\psi^{(0)}, k_2, k_1) \psi^{(1)}(k_1, t) dk_1 \quad .$$

. . . . . (II-9)

Therefore, under these conditions the interaction integral may be written as

$$\int_{k_1} I^{(0)}(\psi^{(0)}, k_2, k_1) \psi^{(1)}(k_1, t) dk_1 = -(\beta + \beta_r) \psi^{(1)}(k_3, t) \quad .$$

. . . . . (II-10)

Through the relaxation assumption, the interaction is tied directly to the wind input. The size of  $\beta_r$  relative to  $\beta$  determines the closeness of this tie.

## LIST OF REFERENCES

1. Benjamin, T. B., Shearing Flow Over a Wavy Wall, JFM, 6, 161-205, 1959.
2. Benjamin, T. B. and Feir, J. E., The Disintegration of Wave Trains on Deep Water, JFM, 27, 417-430, 1967.
3. Cox, C. S., Measurements of Slopes of High Frequency Wind Waves, JMR, 16, 199-225, 1958.
4. Cox, C. S. and Munk, W. H., Measurement of the Roughness of the Sea Surface from Photographs of the Sun's Glitter, J. Opt. Soc. of Am., 44, 11, 838-850, 1954.
5. Crombie, D. D., Doppler Spectrum of Sea Echo at 13.56 mc/s, Nature, 175, 681-682, 1955.
6. Dorman, C. E. and Mollo-Christensen, Observations of the Structure on Moving Gust Patterns Over a Water Surface ("Cats Paws"), J. of Phy. Ocean., 3, 120-132, 1972.
7. Dorrestein, R., Simplified Method of Determining Refraction Coefficients for Sea Waves, JGR, 65, 2, 637-642, 1960.
8. Hasselmann, K., On the Non-Linear Energy Transfer in a Gravity-Wave Spectrum Part 1. General Theory, JFM, 12, 481-500, 1962.
9. Hasselmann, K., On the Non-Linear Energy Transfer in a Gravity-Wave Spectrum Part 3. Evaluation of the Energy Flux and Swell-Sea Interaction for a Neumann Spectrum, JFM, 15, 385-398, 1963.
10. Hasselmann, K., Weak Interaction Theory of Ocean Waves, Basic Developments in Fluid Dynamics, Vol. 2, Academic Press, N.Y., 1968.
11. Hasselmann, K., On the Mass and Momentum Transfer Between Short Gravity Waves and Larger-Scale Motions, JFM, 50, 189-205, 1971.
12. Keller, W. C. and Wright, J. W., Microwave Scattering and the Straining of Wind-Generated Waves, Radio Science, 10, 2, 139-147, 1975.
13. Kinsman, B., Wind Waves, Their Generation and Propagation on the Ocean Surface, Prentice-Hall, Inc., Englewood Cliffs, N.J., 1965.

14. Lee, Y. W., Statistical Theory of Communication, John Wiley and Sons, Inc., N.Y., 1960.
15. Long, S. R. and Huang, N. E., On the Variation and Growth of Wave Slope Spectra in the Capillary-Gravity Range with Increasing Wind, Unpublished Manuscript, 1975.
16. Longuet-Higgins, M. S., On the Action of a Variable Stress at the Surface of Water Waves, Phys. Fluids, 12, 737-740, 1969a.
17. Longuet-Higgins, M. S., A Non-Linear Mechanism for the Generation of Sea Waves, Proc. Roy. Soc. A., 311, 371-389, 1969b.
18. Longuet-Higgins, M. S. and Smith, N. D., An Experiment on Third-Order Resonant Wave Interactions, JFM, 25, 417-435, 1966.
19. Longuet-Higgins, M. S. and Stewart, R. W., Changes in the Form of Short Gravity Waves on Long Waves and Tidal Currents, JFM, 8, 565-583, 1960.
20. Longuet-Higgins, M. S. and Stewart, R. W., Radiation Stress in Water Waves, Deep-Sea Res., 11, 529-562, 1964.
21. McCuskey, S. W., An Introduction to Advanced Dynamics, Addison-Wesley Publishing Co., Reading, Mass., 1959.
22. McGoldrick, L. F., Resonant Interactions Among Capillary-Gravity Waves, JFM, 21, 305-331, 1965.
23. McGoldrick, L. F., Phillips, O. M., Hueng, N. E. and Hodgson, T. H., Measurements of Third-Order Resonant Wave Interactions, JFM, 25, 437-456, 1966.
24. Mitsuyasu, H. and Honda, T., The High Frequency Spectrum of Wind-Generated Waves, J. of the Oceanographical Society of Japan, 30, 4, 185-198, 1974.
25. Miles, J. W., On the Generation of Waves By Shear Flows, JFM, 3, 185-202, 1957.
26. Miles, J. W., On the Generation of Surface Waves by Turbulent Shear Flows, JFM, 7, 469-478, 1960.
27. Miles, J. W., On the Generation of Surface Waves by Shear Flows, Part 4, JFM, 13, 433-448, 1962.
28. Munk, W. H., High Frequency Spectrum of Ocean Waves, JMR, 14, 302-314, 1955.
29. Palm, C. S., An Instrument to Measure the Two-Dimensional Wave Slope Spectrum of Ocean Capillary Waves, Doctoral Dissertation, University of Florida, 1975.

30. Phillips, O. M., On the Generation of Waves by Turbulent Wind, JFM, 2, 417-445, 1957.
31. Phillips, O. M., On the Dynamics of Unsteady Gravity Waves of Finite Amplitude, Part 1, The Elementary Interactions, JFM, 9, 193-217, 1960.
32. Phillips, O. M., Recent Developments in the Theory of Wave Generation by Wind, JGR, 67, 8, 3135-3141, 1962.
33. Phillips, O. M., On the Attenuation of Long Gravity Waves by Short Breaking Waves, JFM, 16, 321-332, 1963.
34. Phillips, O. M., The Dynamics of the Upper Ocean, Cambridge University Press, 1969.
35. Pierson, W. J., The Theory and Applications of Ocean Wave Measuring Systems at and Below the Sea Surface, on Land, from Aircraft, and from Spacecraft, Univ. Inst. of Oceanography, City University of New York, June, 1975.
36. Robinson, E. A., Multichannel Time Series Analysis with Digital Computer Programs, Holden-Day, 1967.
37. Ruskevich, V. G., Leykin, I. A. and Rosenberg, A. D., Multisensor Wave-Measuring System for the Study of the Space-Time Structure of Waves in the High-Frequency Part of the Spectrum, Okeanologiya, 13, 2, 357-361, 1973.
38. Russell, J. S., Report of the Committee on Waves, Proc. Brit. Ass. Adv. Sci., 7th Meeting, York, 1844, 311-390, 1844.
39. Schooley, A. H., A Simple Optical Method for Measuring the Statistical Distribution of Water Surface Slopes, J. Opt. Soc. of Am., 44, 1, 37-40, 1954.
40. Schooley, A. H., Curvature Distributions of Wind-Created Water Waves, Trans. Am. Geophysical Union, 36, 2, 273-278, 1955.
41. Scott, J. C., An Optical Probe for Measuring Water Wave Slopes, J. of Physics E: Scientific Instruments, 7, 747-749, 1974.
42. Shemdin, O. H., Air-Sea Interaction Laboratory Facility, TR3, Dept. of Coastal and Oceanographic Engineering, University of Florida, Gainesville, Fla., 1969.
43. Shemdin, O. H., Wind Generated Current and Phase Speed of Wind Waves, J. Phy. Ocean., 2, 4, 411-419, 1972.
44. Shemdin, O. H., Lai, R. J., Reece, A. and Tober, G., Laboratory Investigations of Whitecaps, Spray, and Capillary Waves, TR11, Coastal and Oceanographic Engineering Laboratory, University of Florida, 1972.

45. Sinitsyn, Yu. A., Leykin, I. A. and Rozenberg, A. D., The Space-Time Characteristics of Ripple in the Presence of Long Waves, Izv. Atmospheric and Oceanic Physics, 9, 5, 511-519, 1973.
46. Stewart, R. W., The Wave Drag of Wind Over Water, JFM, 10, 189-194, 1961.
47. Tick, L. J., A Nonlinear Random Model of Gravity Waves, I. Jour. Math. and Mech., 8, 5, 643-652, 1959.
48. Ursell, F., Steady Wave Patterns on a Non-Uniform Steady Fluid Flow, JFM, 9, 333-346, 1960.
49. Valenzuela, G. R., Further Results on Non-Linear Energy Transfer in Gravity-Capillary Wave Spectra, With Viscous Considerations, NRL Report 7913, 1975.
50. Valenzuela, G. R. and Laing, M. B., Nonlinear Energy Transfer in Gravity-Capillary Wave Spectra, with Applications, JFM, 54, 507-520, 1972.
51. Welch, P. D., The Use of Fast Fourier Transform for the Estimation of Power Spectra: A Method Based on Time Averaging Over Short, Modified Periodograms, IEEE Trans. on Audio and Electro Acoustics, AU-15, 2, 70-73, 1967.
52. Wentz, F. J., Cox and Munk's Sea Surface Slope Variance, JGR, 81, 9, 1607-1608, 1976.
53. Whitman, G. B., A Note on Group Velocity, JFM, 9, 3, 347-352, 1960.
54. Wu, J., Laboratory Studies of Wind-Wave Interactions, JFM, 34, 1, 91-111, 1968.
55. Wu, J., Slope and Curvature Distributions of Wind-Disturbed Water Surface, J. Opt. Soc. of Am., 61, 7, 852-858, 1971.
56. Wu, J., Correlation of Micro and Macroscopic Structures of Wind-Waves, IEEE Ocean 75, 321-326, 1975.
57. Wu, J., Lawrence, J. M., Tebay, E. S. and Tulin, M. P., A Multiple Purpose Optical Instrument for Studies of Short Steep Water-Waves, The Review of Scientific Instruments, 40, 9, 1209-1213, 1969.
58. Wylie, C. R., Advanced Engineering Mathematics, McGraw-Hill Book Co., 1966.

## BIOGRAPHICAL SKETCH

Allan M. Reece was born 16 September 1947 in Pittsburgh, Pennsylvania. In 1965 he graduated from Mt. Lebanon Senior High School in Pittsburgh and entered Union College in Schenectady, New York. He was graduated in 1969 with honors in mechanical engineering and entered the Rosenstiel School of Marine and Atmospheric Sciences, University of Miami, Miami, Florida. He received his MS in 1971 and entered the University of Florida to begin study toward a doctorate in Coastal and Oceanographic Engineering.

He is married to Margo Marie, née, Bryant, of Hollywood, Florida.

I certify that I have read this study and that in my opinion it conforms to acceptable standards of scholarly presentation and is fully adequate, in scope and quality, as a dissertation for the degree of Doctor of Philosophy.

Omar H. Shemdin

O.H. Shemdin, Chairman  
Professor of Engineering  
Sciences

I certify that I have read this study and that in my opinion it conforms to acceptable standards of scholarly presentation and is fully adequate, in scope and quality, as a dissertation for the degree of Doctor of Philosophy.

B.A. Christensen

B.A. Christensen  
Professor of Civil Engineering

I certify that I have read this study and that in my opinion it conforms to acceptable standards of scholarly presentation and is fully adequate, in scope and quality, as a dissertation for the degree of Doctor of Philosophy.

D.M. Sheppard

D.M. Sheppard  
Associate Professor of  
Engineering Sciences

I certify that I have read this study and that in my opinion it conforms to acceptable standards of scholarly presentation and is fully adequate, in scope and quality, as a dissertation for the degree of Doctor of Philosophy.

R. G. Dean

R.G. Dean  
Professor of Civil Engineering  
University of Delaware

I certify that I have read this study and that in my opinion it conforms to acceptable standards of scholarly presentation and is fully adequate, in scope and quality, as a dissertation for the degree of Doctor of Philosophy.

D. G. Childers

D.G. Childers  
Professor of Electrical  
Engineering

I certify that I have read this study and that in my opinion it conforms to acceptable standards of scholarly presentation and is fully adequate, in scope and quality, as a dissertation for the degree of Doctor of Philosophy.

B. E. Ruth

B.E. Ruth  
Professor of Civil Engineering

This dissertation was submitted to the Graduate Faculty of the College of Engineering and to the Graduate Council, and was accepted as partial fulfillment of the requirements for the degree of Doctor of Philosophy.

December, 1976

Wayne H. Chen

Dean, College of Engineering

Dean, Graduate School

1599 *La m... 83* (107)

RU 1. 77 01.22